The Design, Kinematics and Error Modelling of a Novel Micro-CMM Parallel Manipulator
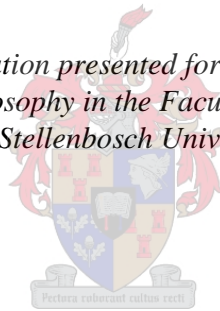
by
Ali Milud Rugbani

Dissertation presented for the degree of
Doctor of Philosophy in the Faculty of Engineering at
Stellenbosch University

Promotor: Prof Kristiaan Schreve

April 2014

Declaration

By submitting this dissertation electronically, I declare that the entirety of the work contained therein is my own, original work, that I am the owner of the copyright thereof (unless to the extent explicitly otherwise stated) and that I have not previously in its entirety or in part submitted it for obtaining any qualification.

Signature: _____

Name: _____

Date: _____

ii

Abstract

The research presented in this dissertation establishes a micro-CMM parallel manipulator as a viable positioning device for three degree of freedom micro measurement applications. The machine offers the advantages associated with parallel kinematic manipulators, such as light carrying weight, high stiffness and no accumulation of errors, while avoiding some of the traditional disadvantages of parallel manipulators such as the associated effects of angular errors (Abbé error), singularity problems, work space limitation and the extensive use of spherical joints.

In this dissertation, the direct position kinematic solution is developed analytically and the solution of the inverse position kinematic is solved numerically. A workspace analysis has been performed. A fully functional prototype demonstrator is fabricated to demonstrate this machine. While the demonstrator was not intended to achieve submicron accuracy, it was intended to validate the error models. Computer controlled measurement is developed and used to position the probe and to record measurements.

A reliable kinematic error model based on the theory of error propagation is derived analytically. A numerical method is used to verify the analytical results. Comparison shows that the results of the error model, both analytical and numerical, represent a very good match and follow the same trend.

The kinematic position model is validated using a conventional CMM. Results show that an average difference of less than 0.5 mm over a set of 30 points is achieved. This result of the micro-CMM demonstrator measurements falls within the error budget of approximately 0.75 mm estimated by the proposed analytical error model.

iii

Opsomming

Die navorsing in hierdie tesis vestig 'n mikro-CMM parallelle manipuleerder as 'n lewensvatbare posisioneringstoestel vir drie vryheidsgraad-mikrometing toepassings. Die masjien bied voordele geassosieer met parallelle kinematiese manipuleerders, bv. ligte dra-gewig, hoë styfheid en geen ophoping van foute nie. Die tradisionele nadele van parallelle manipuleerders soos die geassosieerde gevolge van hoekfoute (Abbé fout), enkelvoudigheidsprobleme, werkspasiebeperking en die uitgebreide gebruik van sferiese koppelings word vermy.

In hierdie tesis word die direkte posisie kinematiese oplossing analities ontwikkel en die oplossing van die omgekeerde posisie kinematies word numeries opgelos. 'n Werkspasie analise is uitgevoer. 'n Ten volle funksionele prototipe demonstrasie-model is vervaardig om hierdie masjien te demonstreer. Die model is nie vervaardig om submikron akkuraatheid te bereik nie, maar eerder om foutmodelle geldig te verklaar. Rekenaar-beheerde metings is ontwerp en gebruik om die toetspen te posisioneer en om metings te neem.

'n Betroubare kinematiese foutmodel gebaseer op die teorie van foutvoortplanting is analities afgelei. 'n Numeriese metode word gebruik om die analitiese resultate te bevestig. Vergelyking toon aan dat die resultate van die foutmodel, beide analities en numeries, goeie pasmaats is en dieselfde tendens volg.

Die kinematiese posisie model word geldig verklaar deur gebruik te maak van 'n konvensionele CMM. Resultate wys dat daar 'n gemiddelde verskil van minder as 0.5 mm oor 'n stel van 30 punte behaal word. Die resultate van die mikro-CMM model se metings val binne die foutbegroting van ongeveer 0.75 mm geskat by die voorgestelde analitiese foutmodel.

Dedication

To the pillars of my life, to my parents and to my wife,

for their endless love, support and encouragement.

Acknowledgements

A special thanks to my family. Words can't express how grateful I am to my mother and father, for all of the sacrifices that you've made on my behalf. Your prayer for me was what sustained me thus far. To my wife, I can't thank you enough for encouraging me throughout this experience. I would also like to thank my brother and sisters, and all family members and friends for their understanding support and encouragement.

To my supervisor, Prof Kristiaan Schreve, for the patient guidance, encouragement and advice he has provided throughout my time as his student. I have been extremely lucky to have a supervisor who cared so much about my work, and who responded to my questions and queries so promptly. It has been a great privilege and honour to work with you.

Many thanks are also due to my Libyan friends here in South Africa, who were a great source of support in my moments of crisis.

I extend my gratitude to my lab and office mates and to my colleagues in the mechatronics, automation and design research group (SU). I really appreciated all the discussions, and the friendships we made.

I would like to express my special appreciation and thanks to all the staff at the Department of Mechanical and Mechatronic Engineering (SU) who ensure its smooth running, and assisted me in various ways, in particular: Mrs Welma Liebenberg, Mr Pieter Hough, Mrs Susan van der Spuy, Ms Marilie Oberholzer, Mr Ferdi Zietsman, Mrs Maurisha Galant.

I would also like to thank Mrs Linda Uys and Mrs Yolanda Johnson (Postgraduate & international office) for all their help.

Finally, I would like to thank the ministry of higher education (Libya) and the University of Stellenbosch, not only for providing the funding which allowed me to undertake this research, but also for giving me the opportunity to attend conferences and meet so many interesting people.

List of Contents:

x

x

List of figures:

xi

List of tables:

List of abbreviations

AFM   Atomic Force Microscopy

AM   Analytical Error Model

CMM   Coordinate Measuring Machine

DAQ   Data Acquisition Cards

DDKM   Direct Differential Kinematic Model

D-H   Denavit-Hartenberg

DOF   Degrees Of Freedom

DPKM   Direct Position Kinematic Model

FEM   Finite Element Modelling

IDKM   Inverse Differential Kinematic Model

IPKM   Inverse Position Kinematic Model

MC   Monte-Carlo Simulation

MEMS   Micro Electro Mechanical System

Micro-CMM Micromeasurment Coordinate Measuring Machine

PKM   Parallel Kinematic Manipulator

SEM   Scanning Electron Microscopy

Nomenclature

α	angle of Abbé effect
β	angle between links
θ	angle of sensor misalignment
σ	standard deviation
ε	error
$e\beta$	error in angle between the legs of the tetrahedron
eab	Abbé error
eb	parallelism in the runner blocks
$ecos$	angular errors of the actuator, cosine error
ed	error in the dead distance in the links
el	error in link length
em	backlash in the motors
ep	probe error
er	error in laser distance reading
es	error in spherical joints
ex_i, ey_i, ez_i	error in pivot points coordinates
i	$[a,b,c]$
l_i	distance between pivot point and probe tip
p_i	pivot point
r_i	reading of the laser distance sensor
x, y, z	coordinates of the probe
x_i, y_i, z_i	coordinates of the pivot points

CHAPTER 1:

Introduction

1.1   Introduction

Engineers and scientists are constantly striving to measure distances more accurately. It is integral to our ability to produce products that are more sophisticated. The accuracy to which we can measure depends directly on the distance being measured. In manufacturing, these accuracies must be achieved in three dimensions, i.e. the measurement system must be capable of moving around the object and measure distances in any direction. At macro scale (roughly a few millimetres to a meter), it is now possible to measure within 0.001 mm (or

1

1 micron). The currently available measurement technologies for dimensional metrology can be divided into the following principles [1]:

- Interferometric solutions
- Microtopography measuring instruments
- Scanning electron microscopy (SEM)
- Micro and nano coordinate measuring machines
- Other techniques

Interferometry is basically a one dimensional measuring system, usually systems with multiple interferometers are used to benefit from its nm range of measurement uncertainty and accuracy. Even though the microtopography instruments provide three dimensional surface topography measurement, its capability is limited in the vertical axis for a high aspect ratio features. SEM devices can easily achieve micrometre and manometer region, they are commonly used to inspect 2D objects. The problem with SEM is the limitation to measure 3D objects with deep channels, cavities, holes and side walls.

The conventional coordinate measurement machines (CMM) have the ability to move a probe in three dimensions and take 3D measurements at macro scale. At the other end of the spectrum there are 3D measurements to nanometre accuracy such as the AFM, but then the range is a fraction of a millimetre.

There is a gap for measurement systems that can measure in 3D over a distance of up to 100 mm to an accuracy of much better than a micron but not quite at nanometre level. This limitation is due to either lack of accuracy or probing system [1].

Method of measurement can be chosen based on the aspect ratio of the object to be measured. Aspect ratio of a structure is defined as the depth divided by its width. 2D techniques can measure features with aspect ratio below 1. Features with aspect ratio greater than 1 are referred to as 2½D. Measurements of features of free-forms, deep holes, channels and cavities are called 3D [1]. Figure 1 shows a classification of these major techniques based on the feature size [2].
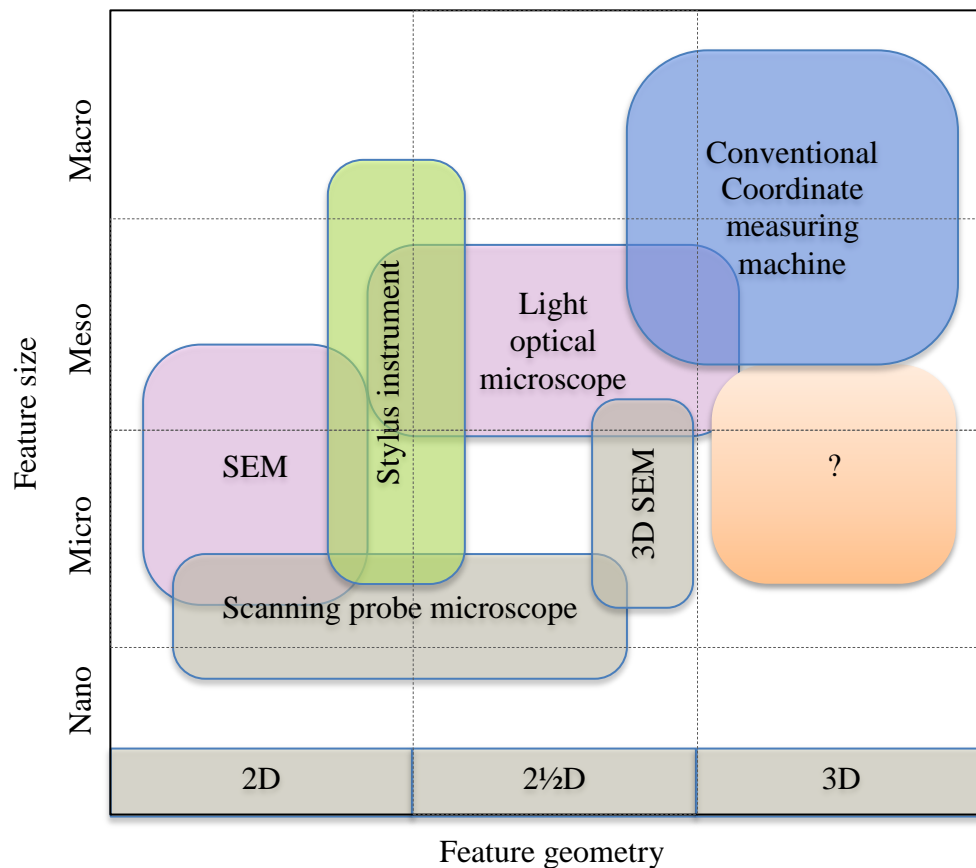
Figure 1: Classification of metrology measuring devices, depicted from [2].

The meso scale referred to on the vertical axis is typically the 100 mm range in any three dimensional direction, Figure 1 show that none of the reviewed techniques are capable of characterization of full three dimensional features with less than 1 micro meter accuracy. The figure further illustrates the need to achieve

precision better than 100 nm. These machines are called micrometrology coordinate measurement machines (micro-CMM). The development of micro-manufacturing (i.e. manufacturing in the same dimensional range and accuracy) has driven this demand.

There are already a number of commercially available machines that operate in this range. However, as the analysis of the commercially available systems in section 2.12 will show, they either lack in range or accuracy.

In this research the author is proposing a novel design of such machines that overcome certain fundamental problems that existing systems have, such as workspace limitation, effect of angular errors and singularity problems. Therefore it is anticipated that these systems will come closer or even achieve the goal of a true micro-CMM.

1.2 Objectives, motivation and contributions of the thesis

A high precision and high accuracy micro-CMM, at a lower cost than traditional machines, will be introduced for the measurement of part dimensions in micro scale. The design is considering a completely new system module, including the structure for a better stiffness and stability, reduction of Abbé error, the position of the probe will be determined using a mathematical module, and the distances will be measured using laser distance sensors feedback.

The work envelope of the measuring range of the machine is around 100 mm x 100 mm x 100 mm, and aimed to achieve resolution in the submicron regime. Linear motors and laser distance sensors are to be used to drive the stage and feedback the position to the control.

The primary objective of this research can be broken down in to the following points:

- Derive an efficient measuring model to accurately determine the relative position of the probe in Cartesian coordinates.

- Develop the control algorithm and add a friendly user interface to control the machine.

- Suggest a reliable error modelling technique to estimate and analyse the errors, and to help reducing measurement errors.

- Build a fully functional prototype for the micro-CMM to prove the design concept.

- And eventually, validate the kinematic and error models through set of experiments.

1.3   Organization of the thesis

Chapter 1 includes a brief introduction, and the objectives of the study.

Chapter 2 presents a background to micrometrology and terminology identification in micro-measurement. A literature review of the available machines, measuring techniques and methods of error modelling is included.

Chapter 3 describes the design and structure of the novel micro-CMM used in the study. Coordinate system and workspace analysis are discussed in detail.

In Chapter 4, the derivation of the measurement model is presented, and the solutions to the inverse and direct models are discussed. Moreover, error modelling is also derived and discussed.

In Chapter 5 the implementation of the computer control system is described in detail, and the user interface and the hardware and software used in this study are discussed.

The machine is characterized, its geometrical parameters are identified in Chapter 6.

The results of the analytical kinematic error model are obtained and verified numerically in Chapter 7.

Chapter 8 presents the initial prototype of the machine and gives a comparison with the improved novel micro-CMM.

Chapter 9 offers the conclusions drawn after conducting the confirmation and validation measurements. It concludes with recommendations for improvement of the micro-CMM design and models.

Appendix A presents the detailed design drawings of the proposed mico-CMM. Appendix B presents the Python codes for the inverse and forward kinematic models as well as the analytical error model and Monte-Carlo simulation. The data measurement and the results of the error modelling are tabulated in Appendix C. The specifications and data sheets of the instruments and devices used in the machine are listed in Appendix D.

CHAPTER 2:

Background and literature review

2.1   Introduction to micrometrology

The micro-measurement machines are used for inspection and quality controlling of objects with dimensions normally less than 100 mm, A good example of these objects is microelectromechanical systems (MEMS), usually such objects have micro scale features, an example of such MEMS are the parts used in small electronic devices like cell phones, optical scanners and automobile airbags. The machining, assembly, inspection and quality controlling of these devices require high positioning accuracy. It is very important for MEMS producers to accurately meet high manufacturing standards.

The technology of micrometrology measurement has received much attention in research during the past two decades to fill the gap between the ultrahigh precise measurements of nanometrology and macrometrology [3]. The major challenge of the micro-measurement machines is to provide accurate measurements in the submicron level.

Generally, micro-measurement technology can be divided into two main categories, non-contact (optical and laser-based systems) measurement technique, and contact probing measurement techniques. The main advantage of the contact probe machines is their capability of measuring deep narrow holes and peek around edges. Contrary the non-contact technologies, such as white light interferometer, confocal microscope, holographic microscope, scanning probe microscope, etc., such devices cannot measure side walls or steep surface, even though, they facilitate the measurement of surfaces in the submicron range easily [2].

The ball tip of the contact probe must be perfectly spherical, more importantly they must be manufactured as small as possible and should be sensitive to very small contact forces. During the last decade a number of probes has been developed to be used with contact probing machines [4], [5].

2.2   Terminologies used in metrology

The most common fundamental terms of identifying the capability performance of a positioning system can be summarized as follows:

2.2.1   Measurement uncertainty

There is no guaranteed perfect measurement. Every measurement must be accompanied by the associated uncertainty. The guide to the expression of uncertainty in measurement (GUM), is the definitive document on this subject [6].

8

Uncertainty of measurement is a non-negative value associated with a measurement that reflects the doubt of the measured quantity. Uncertainty value can be estimated by quantifying the measured data to estimate the confidence about the results.

According to Feng, et al. [7] the uncertainty estimation for CMM measurements can simply be a prediction by an experienced operator.

2.2.2   Resolution of a measuring machine

Resolution is commonly defined in literature as the smallest increment can be controlled of a system to create a positional change [8]. The overall accuracy of micro measurement machines are primarily limited by the accuracy of the instruments used in its parts, mainly the probing systems [9].

2.2.3   Precision of a measurement

Precision is a term that represents the relation between the spread of the measured data to the true value of these measurements [10]. Precision is also called repeatability if determined under the same methods and using the same equipment by the same operator. Reproducibility is also the precision of measurements determined using same methods by different equipment and operators [11].

2.2.4   Accuracy of a measurement

Accuracy is a qualitative term representing the closeness degree of the mean of the measurements to its true value [10]. Prior knowledge of the exact value must be available to determine the accuracy. It is easier to achieve high resolution and precision than accuracy [8].

Figure 2 below illustrates the difference between precision and accuracy; the centre points of the circles represent the actual value of the measurement.
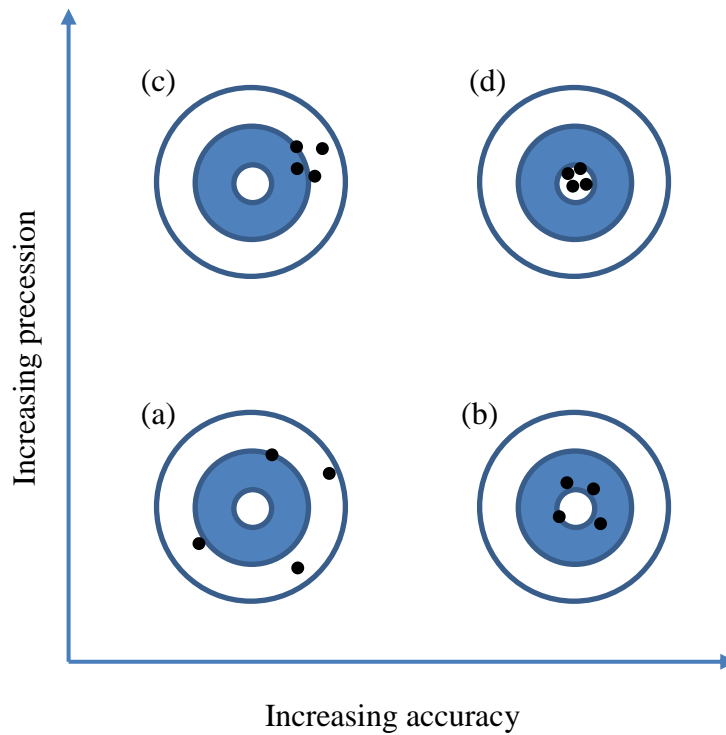
Figure 2: Difference between accuracy and precision.

(a): the measurements are neither accurate nor precise, measured data are scattered all around the true value.

(b): the measurements are accurate but not precise, measured data are close to the true value but not close to each other.

(c): the measurements are precise but not accurate, measured data are close to each other but all are not close to the true value.

(d): the measurements are accurate and precise, measured data are close to the true value and also very close together

10

2.2.5   Measurement traceability

Measurement traceability is a term used to represent the method of determining the accuracy and precision of the CMM. The National Institute of Standards and Technology (NIST) defined traceability of measurement as as: "Traceability of measurement requires the establishment of an unbroken chain of comparisons to stated references each with a stated uncertainty" [12].

2.3   Micrometrology and micro-CMMs

The micrometrology requirements of high accuracy and resolution for determining the 3D measurements of fine parts of MEMS are beyond the capabilities of conventional CMMs [13]. That urged the need for ultrahigh precise measurement technologies, bearing in mind that the design of conventional CMMs cannot be scaled down to micro-CMM as the accuracy of the accuracy of the mechanical parts always remain in micrometre domain [13].

Micro machines can provide a very high degree of precision and they consume much less energy than a regular machine. These characteristics make micro machines popular in many industrial fields.

During the period of late 90's and mid 2000's number of micro-CMMs have been introduced, such as the nano-CMM which was developed in 1998 by Takamatsu [14], small CMM in 2003 by NPL [15], nanopositioning CMM in 2004 by Hausottee and Jager [16], micro-CMM by Fan [17] and Liang in 2004 [18]. The micro-CMM have become a hot topic of research.

Wang [19] listed a general comparison of specifications of the measurement accuracy and resolution of the micro-CMM compared to the available conventional macro-CMM, in Table 1.

11

Table 1: Comparison between macro-CMM and micro-CMM machines [19].

Specification	Conventional CMM	Micro-CMM
Size of machine (mm^3)	1000x900x1200	300x300x400
Weight of machine (Kg)	1000	40
Measuring range (mm^3)	600x500x400	20x20x10
Resolution (nm)	1000	30
Accuracy (nm)	3000	50
Min probe diameter (μm)	500	50
Min contact force (mN)	100	0.05

Isara (IBS Precision Engineering) is available in the market for ultra-precision measurements; it comprises a moving product table and a metrology frame with thermal shielding on which three laser sources are mounted [20], the working envelope is 100 mm x 100 mm x 40 mm, and it can reach uncertainty of 109 nm in 3D. The F25 micro-CMM (Carl Zeiss) is another product, with working envelope of 100 mm x 100 mm x 100 mm, and can provide uncertainty of less than 250 nm [21]. Moreover, the AI-Hexapod of Alio industries has a work envelope of 15 mm to 200 mm with resolution of 5 nm [22]. PI (Physik Instrumente) produced hexapods for high precision linear travel range of up to 100 mm with actuator resolution of up to 5 nm [23]. Further, the National Physical Laboratory (NPL) is currently conducting research on the probe so that measurements accuracy can be improved [24].

2.4   Scale factor

The ratio between measuring range and accuracy is known as the scale factor, see Figure 3. In precision measurement this ratio is around 10^{-4}. This scale factor can be achieved by conventional measuring methods within the macro and nano scale,

while a gap between nano and macro scale measurements exists in the scale interface [15].
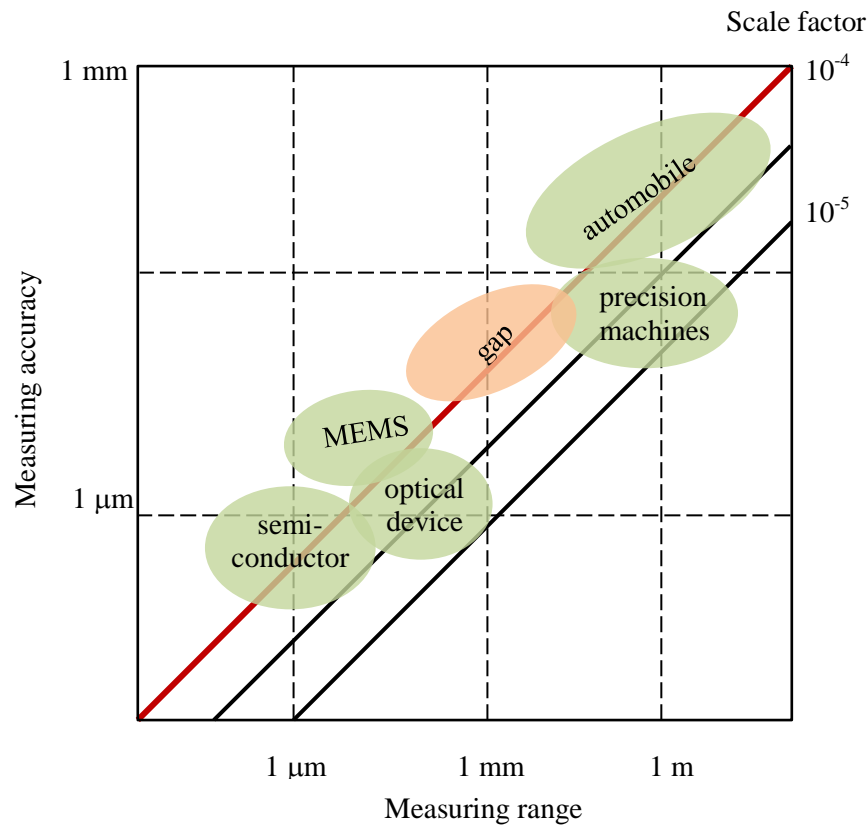
Figure 3: Scale factor over scale interface [26].

2.5   Type of CMM mechanisms

The first CMM was introduced in 1959 by the British company Ferranti metrology group, (currently International Metrology Systems Ltd IMS) [27]. Since then the CMMs quickly evolved in the mid 1960's. In the early 1970's with the introduction of the touch trigger probe by Renishaw, the use of CMMs started to rapidly attract attention by manufacturing companies. There are two fundamental concepts for the movement of the probe; serial and parallel mechanisms [28].

2.5.1   Serial CMMs

Here, all the links are connected to each other like a chain. This chain is as strong as its weakest link. The links are normally arranged in a way that is orthogonal to each other to create three axes. The probe location is determined, typically in micrometre precision, by reading the travel distance of each axis. If one link causes a measurement error, it is directly propagated through the entire system. There will also be an accumulation of errors, since it is impossible to make a link with zero error contribution. Figure 4 shows a photograph of a conventional CMM from Mitutoyo.

Figure 4: Photograph of a conventional CMM from Mitutoyo.

14

2.5.2 Parallel CMM arrangement

The alternative to serial mechanisms is parallel mechanisms. Unlike the open-chain structure of the serial mechanisms, parallel manipulators consist of several links connected in parallel to create a closed-chain structure. Generally parallel manipulators consist of a moving platform and a fixed base, connected by several links. Each link is directly connected to the probe; therefore there is no accumulation of errors. This, and the fact that these systems are normally stiffer that equivalent serial mechanisms, are the factors that lead researchers around the world to believe that this layout will bring a breakthrough in micro-CMM design. The probe position is determined by solving the relatively complex kinematics of the closed chain mechanism.

Obviously, there are some other difficulties with using parallel mechanisms; otherwise they would have been more widely used. With this study the author believes that at least some of these problems can be overcome with the proposed micro-CMM. Figure 5 show a typical parallel manipulator CMM.
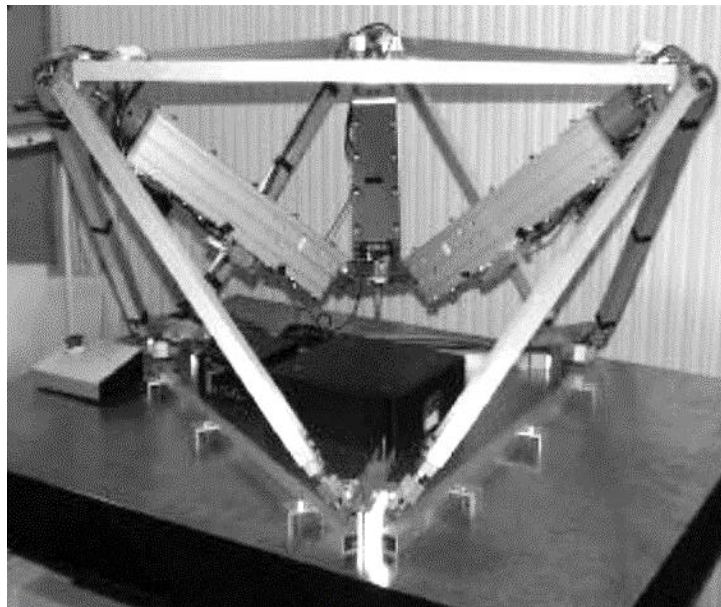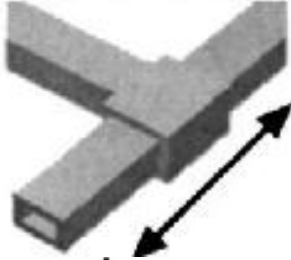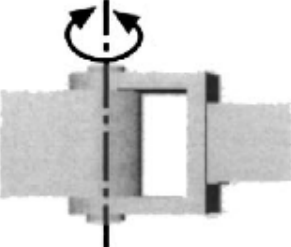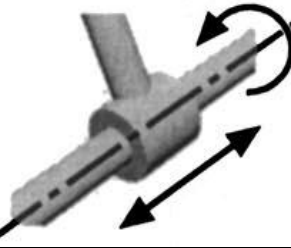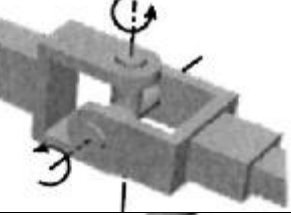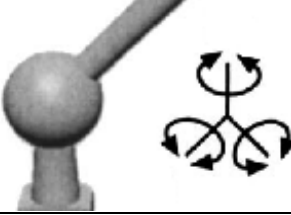
Figure 5: Photograph of a typical parallel manipulator CMM [29].

15

Micro machines have attracted a renewed interest in introducing and developing new types of parallel kinematics machines [30], [31]. Parallel Kinematic Manipulators (PKM) were extensively studied as micro positioning and machining structures [32 – 34]. For instance, Liu [35] has developed a micro parallel manipulator, Harashima [36] has introduced an integrated micromotion system, a micro parts assembly system, Zubir [37] presents a high-precision micro gripper that was designed by Bang [38]. Moreover, Gilsinn [39] worked on developing a scanning, tunnelling microscope using macro-micro motion system.

2.6   Classification of parallel manipulators

Using the enumeration theory of basic kinematic chains given by Tsai [40] it is possible to enumerate the parallel manipulators according to the arrangement of their kinematic chains that constrain an end-effector [41]. The most common basic joints used in parallel mechanisms are arranged in an increasing order of degrees of freedom shown in Table 2.

Table 2: Basic joints commonly used in PKMs [42].

Joint type	Description	Symbol	DOF
Prismatic		P	1
Revolute		R	1
Cylindrical		C	2
Universal		U	2
Spherical		S	3

2.7   3-DOF parallel manipulators

Parallel mechanisms are usually presented by their number of DOF of the end-effector, usually between 2 and 6-DOF. The DOF of a manipulator can be

17

translational only, rotational only or mixed DOF. In the following some of the common 3-DOF manipulators will be presented.

Manipulators with translation 3-DOF are widely used for pick-and-place and machining operations. The most famous robot of this type is a mechanism that was first described in 1942 by Pollard [43], further improvements were done by Clavel by introducing the UPR type Delta robot [44], see Figure 6.

Figure 6: Industrial version of the DELTA robot,
the FlexPicker IRB 340 (from ABB).

The Orthoglide robot is another robot which was developed by Wenger [45] for machine tool application, the arrangement of its joints is of the PRR type, where a parallelogram is used for the connection between the revolution joint in each link, see Figure 7.

18
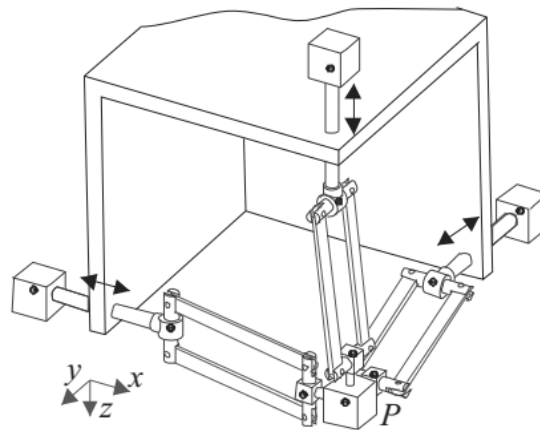
Figure 7: The Orthoglide robot [45].

Another 3-DOF manipulator was introduced by Kong [46] which included cylindrical joints in its kinematic links CRR, where the translational movement of the C joints are actuated, see Figure 8.
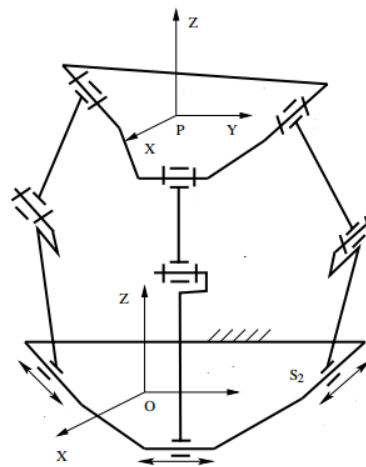
Figure 8: The 3-CRR robot of Kong [46].

Figure 9 show a very popular 3-DOF with pure translational motion proposed in 1996 by Tsai [47], which belong to the 3-UPU manipulator type.

19

Figure 9: Tsai's translation parallel manipulator [47].

Di Gregorio [48] proposed a pure rotational parallel manipulator, the moving platform is connected by three RUU legs in parallel, and Hereve [49] added an improved version of the same 3-RUU manipulator type, see Figure 10.

Figure 10: Two different designs for the 3-RUU manipulator type.

Many other structures have been proposed by Fong and Tsai as wrist: 3-RRS, 3-CRU, 3-UPC, 3-CRC [50], Di Gregorio also proposed 3-RSR [51]. A comprehensive list of different manipulators is covered by Kong [46].

20

2.8   Parallel vs. Serial CMMs

The major advantages of parallel mechanisms as compared to their serial counterparts can be summarised as:

Firstly, higher accuracy, since its moving components are more strongly related and errors are not cumulative and amplified. Secondly, they have higher structural rigidity than the serial CMMs, since the end-effector is simultaneously carried by several legs in parallel. Lastly, they carry lighter moving mass, as the location of all the actuators and motors are in the base close to the end effector, allowing it to function at a higher speed and with greater precision [52]. Therefore, parallel robots are suitable for applications in which high speed, high positioning accuracy, and a rapid dynamic response are required.

Another advantage of the PKM is that the solution of the inverse kinematics equations is easier. However, the problems concerning kinematics and dynamics of parallel robots are as a rule more complicated than those of serial one.

The main disadvantage of parallel CMMs is the limited workspace [53 − 55], and the difficulty of their motion control due to singularity problems [52], [56]. Many researchers studied the singularity problem and workspace analysis of some planar parallel mechanisms [57], [58].

As PKM are used for more difficult tasks, control requirements increase in complexity to meet these demands. The implementation for PKMs often differs from their serial counterparts, and the dual relationship between serial and parallel manipulators often means one technique which is simple to implement on serial manipulators is difficult for PKMs (and vice versa). Because parallel manipulators result in a loss of full constraint at singular configurations, any control applied to a parallel manipulator must avoid such configurations. The manipulator is usually limited to a subset of the usable workspace since the required actuator torques will

21

approach infinity as the manipulator approaches a singular configuration. Thus, some method must be in place to ensure that the manipulators avoid those configurations.

In PKMs deformations caused by gravitation forces has very significant effect due to the non-constant stiffness of the structure within the workspace. In contrast, for serial kinematics machines the deformation can be considered constant in the entire workspace and therefore it can easily be automatically compensated in the calibration.

2.9   Error sources

The positioning accuracy of parallel mechanisms is usually limited by many errors, some authors identified the errors affecting the precision of parallel mechanisms as follows [52], [59 − 61]: manufacturing errors, assembly errors, errors resulting from distortion by force and heat, control system errors and actuators errors, calibration, and even mathematical models. These errors should be divided into two main sources, static errors for those not dependent on the dynamics and process forces, and dynamic errors for errors due to the movement and measuring method [62].

2.9.1   Static errors

A high static accuracy is a basic requirement for any micromeasuring machine. Obviously the actual geometry of any machine does not match exactly its design. These differences may cause small positional changes of the probe. The machine then must be properly calibrated to identify its geometric parameters. Any manufacturing and assembly errors of the machine components, especially the joints, will introduce kinematic errors [63]. Sensor errors are caused by angular errors of the actuator (Abbéy's effect) and bending load caused by the weight of the actuator itself [64]. The kinematic errors can be drastically reduced by proper

manufacturing and assembly of the machine parts and sensors. Previous studies showed the influence of joint manufacturing and assembly on the positioning error [52], [65]. Moreover, Huang et al. [66] studied the assembly errors and used manual adjustable mechanisms to control assembly errors. The elastic deformations of the machine structure due to the flexibility of machine components could lead to gravitational errors, a numerical control unit can be used to compensation for the gravitation errors. Moreover, thermal errors should be considered as another source that significantly affects the accuracy due to the thermal deformations and expansion of the legs. Thermal errors can be reduced by compensating for the resulting thermal deformation of the components using a very complex thermal model [67].

Tsai [68], Raghavan [69], Abderrahim and Whittaker [70] have studied the limitations of various modelling methods.

2.9.2   Dynamic errors

These types of errors are dependent on the configuration of the machine. Dynamic errors occur only during operating the machine and depend on the velocity, the acceleration and the forces applied on the end effector. The main sources are friction, wear and backlash occurring in the joints and actuators and deflection in the legs. Additionally, elastic deformations of the machine kinematics through process forces or inertial forces and natural vibrations of the machine can be another sources of dynamic errors.

Static errors are claimed to have the most significant effect on the machine accuracy [67]. Nevertheless, in high precision micro-CMMs the positional error of dynamic sources must be considered. Pierre [71] showed that the operation and the performance of the sensors significantly affect the precision of the manipulator. Hassan analysed the tolerance of the joints [72].

The performance of micro-CMMs in terms of accuracy and precision is influenced by numerous error parameters that require effective error modelling methods [65], [73]. Moreover, the error models are of great importance in order to evaluate the machine and understand the effect of the different parameters. Forward solution for error analysis was also covered [74 – 76].

2.9.3   Abbé error

Abbé error is a very common error in measurement. It can be illustrated with the measurement of a ball's diameter. The diameter is defined through the centre of the ball, but it is impossible to place a ruler there. Therefore, one may use a setup as shown in Figure 11, where two parallel plates are placed next to the ball. The distance between the plates are then measured some distance away from the ball. If one of the plates is misaligned, as shown on the right hand side of the image, the measurement is wrong.
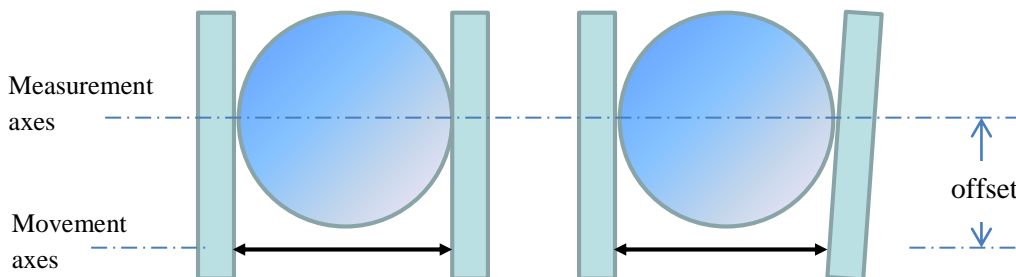
Figure 11: Abbé error illustrated.

Often, this error is unavoidable. Gantry system CMM's inherently has this problem. The error can only be avoided if the measurement of the probe's movement is taken directly from some fixed reference, to the centre of the probe tip.

24

2.9.4   Measurement and movement loops

The structural loop of the machine gives a figure of the possible influence on the stiffness and error budget. The precision and stiffness of a machine can be enhanced if the loop that connects the probe with the work piece through all the elements is closed loop [77].

The electrical motors on CMM's all dissipate heat that is detrimental to high precision measurement. There are also vibrations and variable loads on the motor axes. Therefore it is advisable to not measure on the same axis where the movement of the system happens. That will minimise the effect of the movement on the measurement loops. A typical measurement loop is shown in Figure 12. Clearly, any disturbance along the measurement loop will cause errors. A similar loop can be defined for the movement.
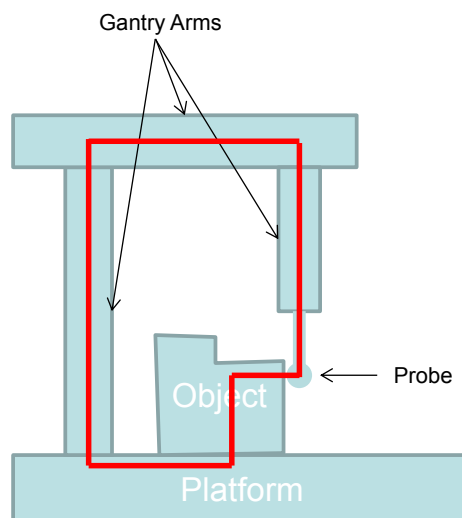
Figure 12: Illustration of a measurement loop.

It is the connected elements consisting of the gantry arms, the probe, the object and the CMM platform. The loop is shown in red.

25

2.10   Kinematic modelling

Parallel mechanism modelling is usually divided in literature into two divisions namely kinematic or geometric models and the dynamic model [78].

The position kinematic model mathematically describes the relations between joint coordinates and the probe position and orientation. The change in the probe's pose is defined with respect to the reference coordinate system. While the dynamic model provides a relation between the probe's acceleration, velocity, coordinates and the influence of forces such as inertia, gravity, torque and non-geometric effects such as friction and backlash.

In 1986 Fichter [79] determined the equations to obtain the leg lengths, directions and moments of the legs and derived these equations for the Stewart platform. Later in 1990, Merlet [80] developed the Jacobian matrix, derived the dynamic equations and determined the workspace of general parallel manipulators. In general, the first step in solving the initial position is to create the forward and inverse position kinematic model by setting the non-linear equations that relate the manipulator variables and the probe pose, then in the next step the non-linear equation system can be solved using analytical or numerical methods or even graphical methods in simple mechanisms.

The position kinematic model can be solved by direct or inverse kinematics, depending on the input and output variables.

A Direct Position Kinematic Model (DPKM) is used to calculate the pose of the probe, given the values for the mechanism.

An Inverse Position Kinematic Model (IPKM) is used to calculate the mechanism's variables for a pose of the probe,

A differential kinematic model is usually used to determine singular configurations or to control the mechanism.

A Direct Differential Kinematic Model (DDKM) is used to obtain the velocity of the end-effector, given the joint velocities.

Inverse Differential Kinematic Model (IDKM) is used to obtain the joint velocities, given the velocity of the end-effector.

Several studies have focused on solving the inverse kinematics of PKM either geometrically [81], analytically [82] or applying the Denavit-Hartenberg (D-H) model [83]. The use of analytical methods is complex, given that the chains share the same unknown factors; therefore, the solutions are usually found using numerical algorithms. In rather simple systems geometric methods can be used. Rao [84] proposed the use of a hybrid optimization method starting with a combination of genetic algorithms and the simplex algorithm. However, for 2-DOF system applying an analytical solution can be more efficient.

In literature many methods have been developed to obtain a mathematical model to solve the direct kinematics of parallel mechanisms. This model determines the roots of one equation, representative of the direct position analysis, in only one unknown. Innocenti et al. [85] solved the direct position analysis and found all the possible closure configurations of a 5-DOF parallel mechanism, in [86] the same authors analyzed a 6-DOF fully parallel mechanism. The developed method finds out all the real solutions of the direct position problem of a 6-DOF fully parallel mechanism. Merlet [87] suggested using sensors to solve the direct model and demonstrated that the measurement of the link lengths is not usually sufficient to determine the unique posture of the platform, and that this posture can be obtained by adding sensors to the mechanism. Sensors can be added by locating rotary sensors in the existing passive joints or by adding passive links whose lengths are measured with linear sensors.

2.11   Parallel machine calibration

According to the international vocabulary of basic and general terms in metrology (VIM), the calibration is definition as: A "Set of operations under specified conditions, that establishes the relation between the quantity of values obtained by a reference to measurement standards and the measurement result that would be obtained using the measuring machine" [11].

The most common reference standards used in CMM calibration are step gauges and ball plates. These reference standards have also to be calibrated regularly [88].

The calibration could be achieved measuring several mechanism configurations and identifying its respective kinematic parameters. Calibration can be done using model-based approaches and numerical approaches. Hollerbach et al. [89] obtained numerical calibration using the least squares method. Daney [90] used methods based on analysis of intervals to certify the calibration of PKM numerically.

The model-based calibration strategies can be classified into three types: external calibration, constrained calibration and self-calibration.

The self-calibration methods of parallel kinematics generally make use of a number of extra sensors on the passive joints. The number of sensors must exceed the number of degrees of freedom (DOF) of the mechanism. Each pose can be used as a calibration pose. These calibration methods are usually of low cost and can be performed inline. Yang et al. [91] used the approach of redundant sensors to calibrate the base and tool by adding one or more sensors on the passive joint in an appropriate way to allow the algorithm to be applied. Singularity based self-calibration method is presented by Last et al. [92]. Parallel mechanisms can be calibrated with this technique only if they have singularities of the second type

28

within their workspace. The advantages of this method are that it does not require any calibration equipment and it gets redundant information from particular characteristics in singular configurations.

Constrained calibration methods are based on constraining the mobility during the calibration process. The idea is to keep some geometric parameters constant such as restricting the movement of the moving platform or the motion of any joint, as a result the number of DOF of the mechanism is decreased. The main advantage of these methods is they do not require extra sensors [78].

The calibration methods with external measuring systems is the most frequently used methods. In these methods, the information is obtained using external devices. External calibration can be divided in four categories: (1) calibration using vision based devices for the measurements, (2) the mobility restriction approach, (3) the redundant leg approach, and (4) the adapted device of measurement approach [93].

Independently of the method chosen, the calibration process is typically carried out using following steps [78], [94]:

- The first step is always the development of a suitable kinematic model to provide a model structure and nominal parameter values.
- The second step is data acquisition of the actual position of the moving platform through a set of end-effector locations that relate the input of the model to the output determination.
- The next step is the identification of the model parameters based on the collected data by using a numerical method to obtain the optimum values of all the parameters included in the model to minimize the platform position error.

- Final step is to identify the error sources and the modelling and implementation of the kinematics compensation models. These methods have been widely studied because of the advantages of these mechanisms.

The results at the end of the calibration process are usually given as a certificate where the machine readings and the reference values can be compared.

2.12   Available systems on the market

The best system is possibly the F25 by Zeiss. Table 3 shows the measurement range, accuracy of a variety of systems. Most of these systems use a gantry system to move the probe; therefore they are all serial manipulators and suffer from the associated problems. The exceptions are the TriNano and Renishaw systems. The TriNano system keeps the probe stationary and moves the object platform. However, this range is limited. The Renishaw system is a parallel mechanism moving the probe. However, its accuracy is not in the micrometrology range and the system suffers significant Abbé errors. The systems from Physik Instrumente and Alio Industries are not measurement systems, but parallel mechanism that can in principle carry a probe. They are only included in the table to show what state of the art parallel mechanisms are capable of. Also, it may be noted that none of the systems achieves the goal of 100 mm range in all directions with an accuracy of better than 0.1 μm. Microtomography (MicroCT) uses X-rays to create a virtual model using cross-sections of the 3D-object.

A comprehensive on-line list of links to websites to manufacturing companies, laboratories as well as to research and development centres in the field of parallel kinematic machines can be accessed in this website: www.parallemic.org.

Table 3: Existing commercial micrometrology systems [95].

Technology	Company	Model	Range [mm]		Resolution [µm]	Accuracy [µm]
			Lat	Vert		
MicroCT	Micro Photonics	SkyScan 1172	50	70	5	
MicroCT	Micro Photonics	SkyScan 1173	140	150	5	
MicroCT	Micro Photonics	SkyScan 1174	32	50	50	
MicroCT	Scanco	µCT 50	50	120	30	
MicroCT	Scanco	µCT 100	100	120	30	
MicroCMM	Zeiss	F25	100	100	0.0075	0.25
MicroCMM	Mitytoyo	UMAP 302	245x 200	200	0.01	2.49
MicroCMM	Mitytoyo	UMAP 350	295x 350	125	0.01	2.7
MicroCMM	Panasonic	UA3P-300	30	20		0.15
MicroCMM	Panasonic	UA3P-4	100	35		0.3
MicroCMM	Panasonic	UA3P-5	200	45		0.3
MicroCMM	Panasonic	UA3P-L	100	50		0.15
MicroCMM	SIOS	NMM-1	25	5	0.0001	
MicroCMM	ISARA	CMM	100	40		0.03
MicroCMM	ISARA	400	400	100		0.1
Parallel Mechanism	Physik Instrumente	M-850	100		±1	
Parallel Mechanism	Alio Industries	AI-TRI-HR8		100	0.005	
Parallel Mechanism	Alio Industries	AI-HEX-HR8		105	0.005	
MicroCMM	TriNano	N100	90	5		0.14 + L/1000
MicroCMM	TriNano	N300	90	5		0.3 + L/1000
MicroCMM	Renishaw	Equator 300	300	150	0.2	2

31

CHAPTER 3:

Novel Micro-CMM design and construction

3.1   Introduction

In this chapter, the design of the novel micro-CMM is described in details, the structure, parts, instruments and devices used in the machine are also described. Major advantages and disadvantages are highlighted.

32

3.2   Machine design

The micro-CMM designed in this research consists of a moving tetrahedron structure with its main vertex pointing downwards. The edges of this frame are carried by three runner blocks where they can slide freely. The runner blocks are connected to the actuated prismatic joints with spherical joints. Moreover, laser distance sensors are installed on the edges of the moving frame in order to acquire accurate measurements of the length of the legs. The movement of the prismatic joints are controlled by three linear motors. A 3D view and a top view of the machine are shown in Figure 13. Moreover, a schematic drawing is given in Figure 14.
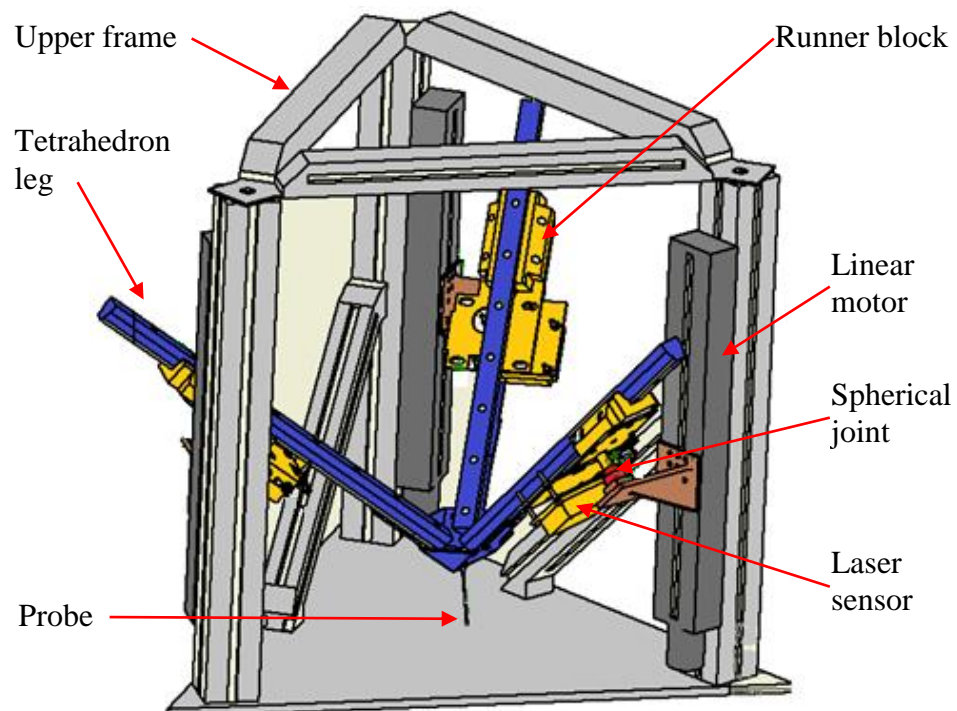
Figure 13-a: 3D view of the micro-CMM design.

33
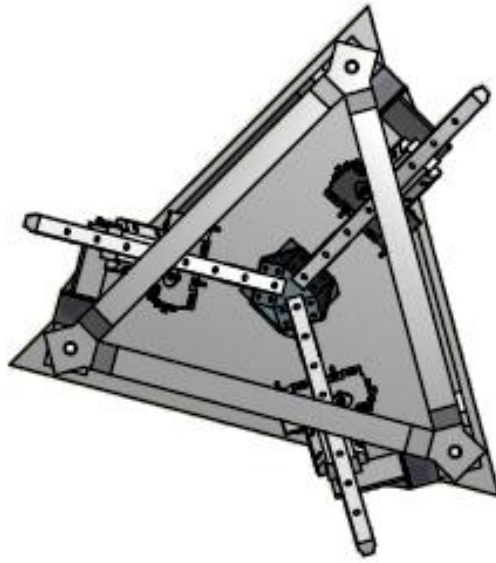
Figure 13-b: Top view of the micro-CMM design.
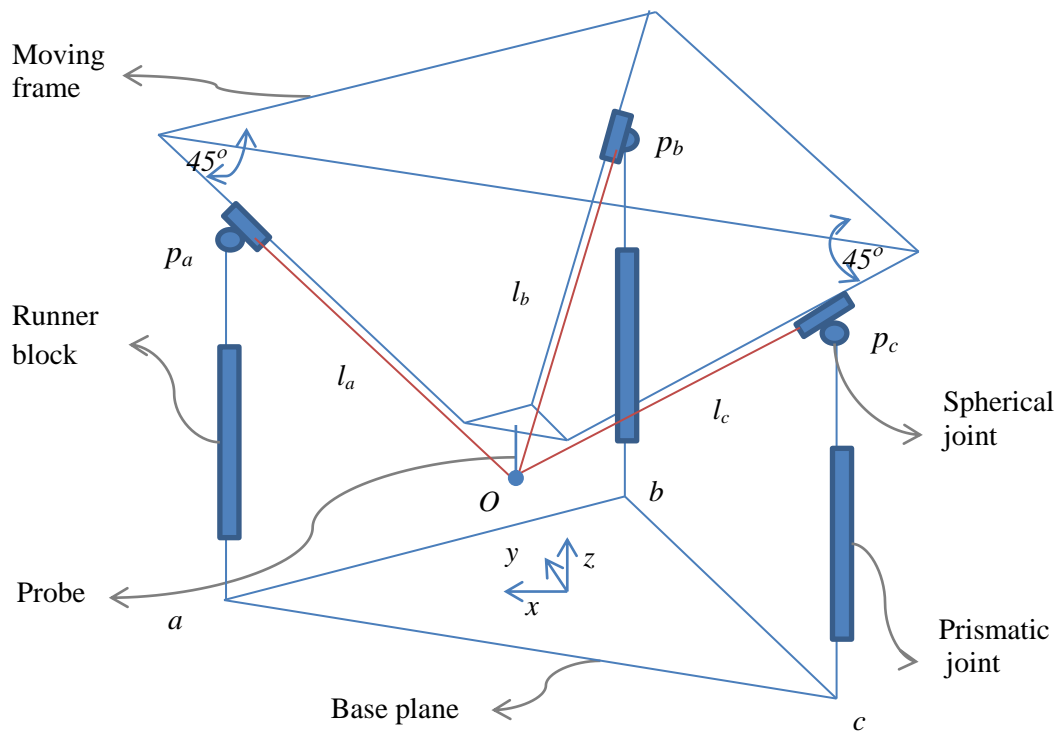
Figure 14: Schematic drawing of the micro-CMM machine.

The arrangement of this micro-CMM provides movement in 3 degrees of freedom (3-DOF), translation in *z* direction, rotation around *x* axis, and rotation around *y* axis. Full design drawings are given in Appendix A.

3.3 Description of the novel micro motion manipulator

The key to this concept is using a fixed tetrahedron. This can be seen in Figure 13. The three coloured beams are the sides of the tetrahedron, these beams are configured in a typical parallel layout where they meet in the middle at the probe platform, and they are the measurement arms. The arms cannot move relative to each other as they together form one part. This makes it different from any of the known concepts. Laser distance sensors are mounted below these beams. The lasers intersect at the centre of the probe ball. Since the tetrahedron is fixed, the lasers will always point directly at the probe centre. That means, in theory, that there will be no Abbé error. The probe is moved by moving the linear motors up and down. This movement repositions the entire tetrahedron, and thus the probe as well. The motors are also not mounted on the measurement arms, thus they do not interfere with lasers.

3.3.1 Machine components and structure

a. Frame and structure

Aluminium extrusion bars from Rexroth were used for increasing rigidity of the machine structure, the 60x60 mm profile shape allow very small deflection values and may be considered rigid elements. The purpose of using a rigid structure is to reduce dynamic errors resulting from the effect of vibration and the weight of the moving parts, reducing the legs' length and mounting the encoder at minimum possible dimensional offset between the probe tip and the measuring axes would be effective in minimizing angular errors.

35

Even though, design for stiffness is not among the objectives of this study, little investigation was done to give an idea of the amount of expected deflection. Mr Craig, in his graduation project, analysed the structure of the preliminary prototype of the machine by applying Finite Element Modelling (FEM) technique [96]. Figure 15 shows the FEM of the micro-CMM.
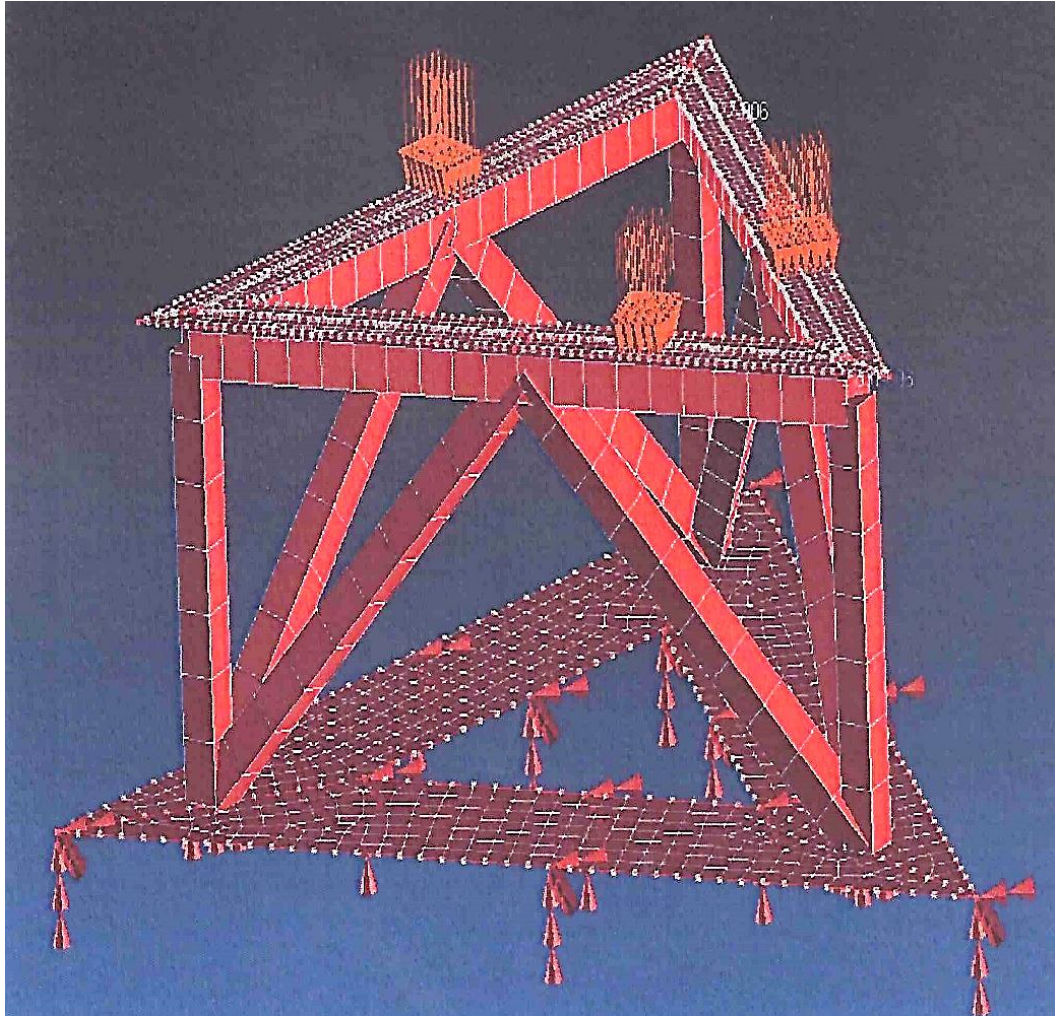
Figure 15: Finite element model of the new micro-CMM [96].

In the physical deformation test, different masses were placed on the frame to study the displacement of predefined points (see Figure 16). Outcomes obtained from this study recommended that a displacement due to the flexibility of the

36

improved structure can reach 0.8 micrometers. These results were confirmed using FEM analysis for the new micro-CMM.
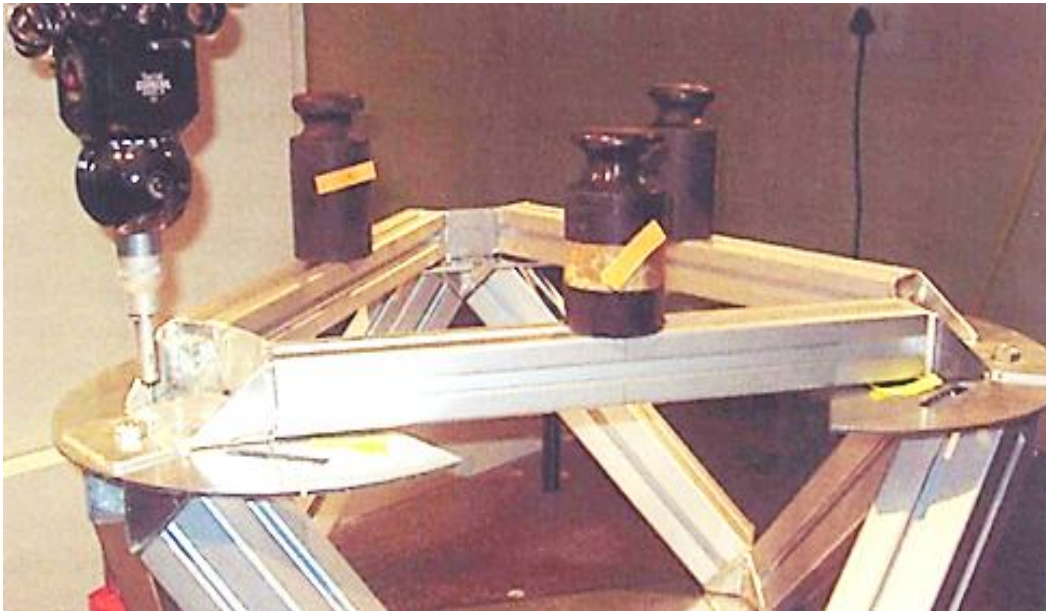
Figure 16: Physical deformation test [96].

b.   Brackets and connections

The required brackets and connections were specially designed and manufactured for this machine. These parts include the probe holder, laser sensor regulator and holder, and motor support and joins holder.

Figure 17 shows the CAD model of the probe holder platform. Besides holding the probe at the centre, the probe holder platform is also the central connections of the three arms of the tetrahedron at fixed designed angles.
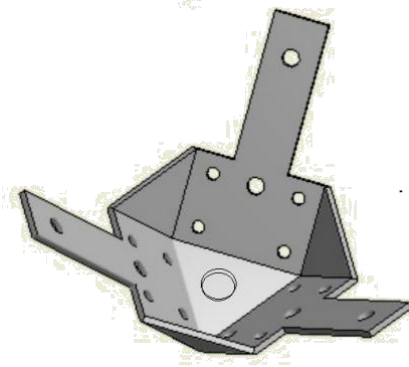
Figure 17: Probe holder and legs connection.

The laser sensor brackets were designed taking into consideration the alignment requirements of the laser beam, misalignment may occur due to the errors during the manufacturing and assembly of the parts.

Figure 18 shows CAD drawings for the top and front views of the laser sensor brackets. Fine threaded bolts carry each part to help in minimizing the misalignment of pitch, roll and yaw angles of the measuring axes.
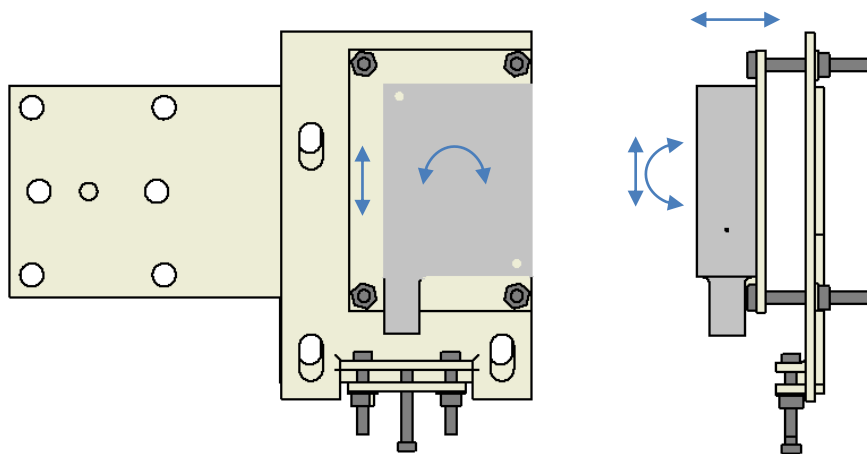
Figure 18: Laser sensor brackets.

38

3.3.2   Bearings, actuators and sensors

a.   Runner blocks and moving arms

The arms of the moving tetrahedron are made of standard precision steel bars from Rexroth. And the runner blocks are also from Rexroth standard precision FLS model. This system of rail and runner block creates parallelism errors between the contact surfaces of +/- 40 µm.

b.   Linear motors

The moving parts are carried by three motors from Zaber (model no. T-LSR). These linear slides with roller bearings have a travel range of 300 mm and can achieve a resolution of micro step size of 0.5 µm with an accuracy of ± 45 µm.

c.   Laser distance sensors

The most important measuring instruments in length and dimensional metrology are the laser interferometers. Due to budget limitation, in this design the distance sensors were optoNCDT ILD 1302 laser distance sensor from Micro-Epsilon, these sensors can provide 50 µm resolution.

d.   Joints

In this study several joints have been identified for use in the proposed Micro-CMM. Mr Blaauw in his undergraduate research project evaluated these joints statistically and physically to determine if they could indeed meet all the design requirements [97]. It was found that flexure joints offered great promise, but would not be able to reach the required angular deformation without failing. As it can be seen in Figure 19 the joins are required to swing for certain angles to reach all the points within the work envelope.

The universal joint was found to have a spherical run-out error of {-0.018 < *error* < 0.016} mm, after calibration that was improved by 30% to reach {-0.013 < *error* < 0.013} mm with 95% confidence.

Standard precision class spherical rolling joints particularly designed by Hephaist Seiko for use in CMMs was selected. These joints provide a run-out error of ± 2.5 μm. These joints also have maximum swing angles up to 40º, which is sufficient for the intended work envelope.
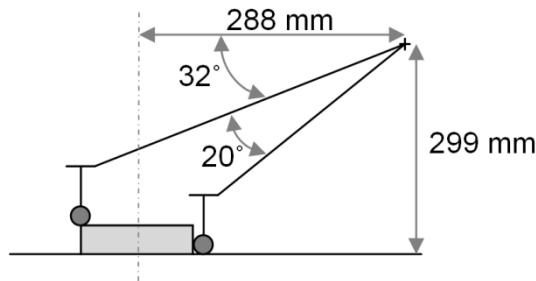
Figure 19: Working angle of the joints.

e. Probe

The Micro-CMM was fitted with Renishaw TP8 manual indexable probe. The TP8 probe provides 0.5 μm repeatability and pre-travel variation of ±1 μm.

3.4   Degrees of freedom of the novel machine

In general, the degree of freedom for a closed-loop spatial mechanism can be obtained by using Grubler's formula as follows:

$$F = 6(l - n - 1) + \sum_{i=1}^{n} f_i$$

Where: F is the degree of freedom, l is the number of bodies including the stage and the base, n is the number of joints, and f_i is the freedom of the ith joint.

40

The number of closed loops or struts are 3, each loop had the same arrangement of joints (prismatic, spherical, slide). The arrangements and DOF for each joint are shown in Figure 20.
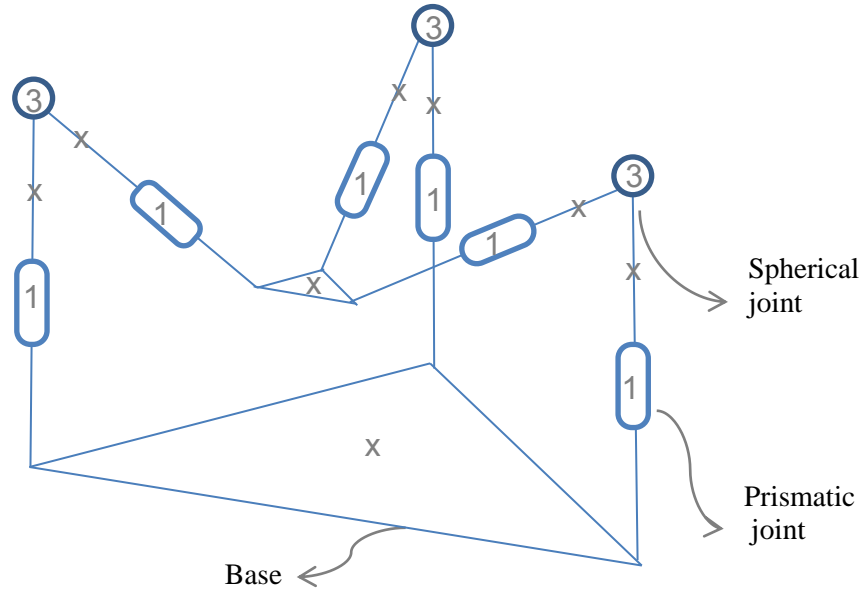
Figure 20: The machine parts, numbers indicate DOF of the joints

Number of all the parts including the moving bodies, $l = 8$, parts are marked with 'x' in Figure 20. Total number of joints, $n = 9$. Spherical joints has 3 DOF, slides and prismatic joints have 1 DOF. Summation of all DOF of the joints = 15.
Appling Grubler's formula, the results show that the novel micro-CMM is classified as 3-DOF parallel kinematic manipulator.

$$F = 6(l - n - 1) + \sum_{i=1}^{n} f_i = 6(-2) + 15 = 3$$

3.5   Micro-CMM prototype

It is obvious that the current prototype lacks certain critical components, e.g. as yet there is not feedback on the run-out error of the rotational joints and the laser displacement sensors' accuracy is not comparable to laser interferometers. The

41

probe that is in use is also not a true micrometrology probe. However, the purpose of the first prototype is to verify the theoretical modelling of the achievable accuracy of the system and also to iron out various design problems. The combination of prototype and the theoretical work serves to guide the development effort and provide evidence of the system's efficacy. Photograph of the micro-CMM, built and fully assembled is shown in Figure 21.
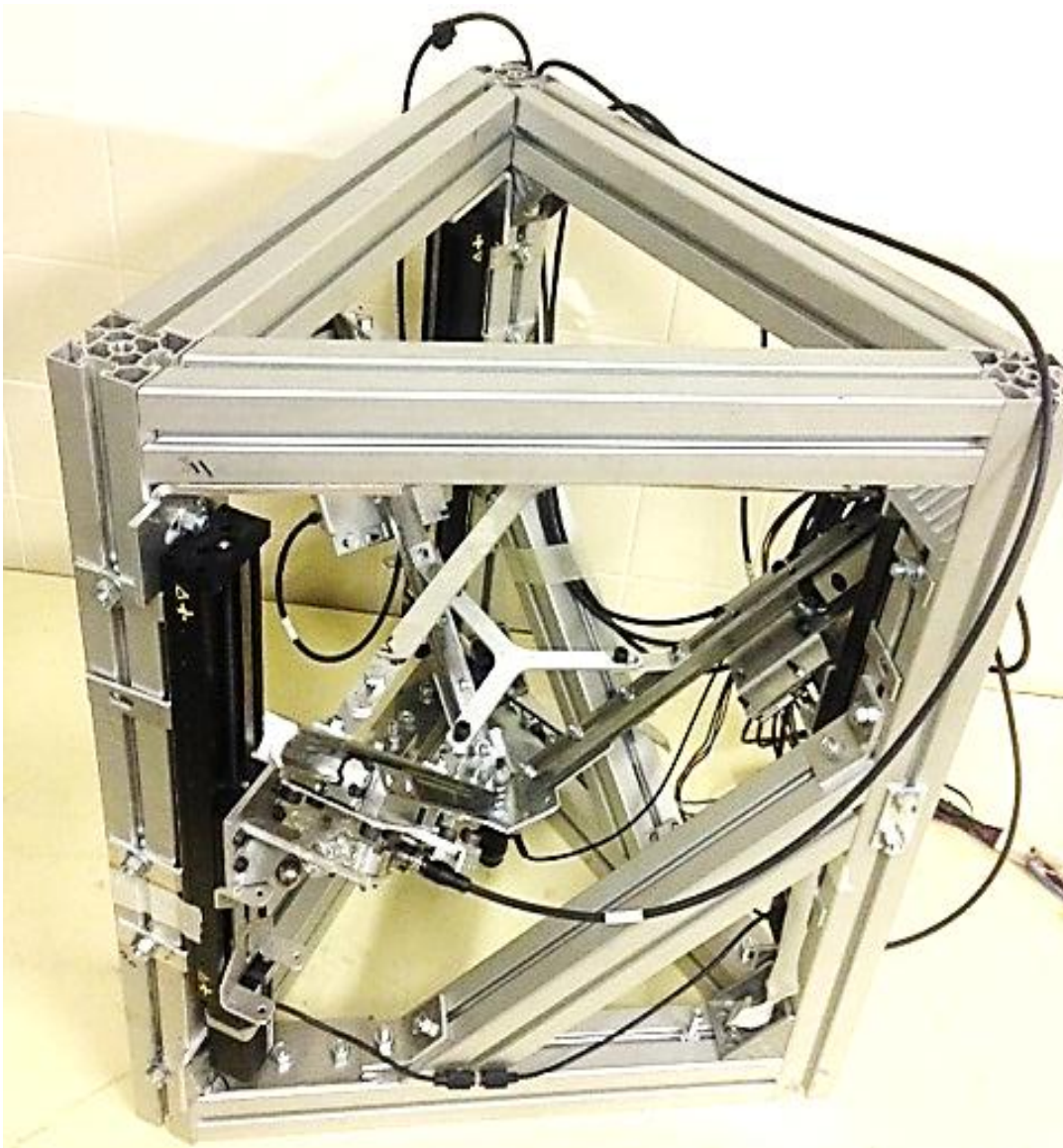
Figure 21: Photograph of the fully assembled micro-CMM.

3.5.1 Advantages of the novel micro-CMM concept

- Singularity free arrangement

  The given kinematic model is defined and well behaved at all points. This provides singularity free movement within the whole workspace. A singularity free system is beneficial to the motion control algorithm.

- Large workspace

  The arrangement of this micro-CMM provides movement in 3-DOF, translation in z direction, rotation around x axis, and rotation around y axis. In other 3-DOF manipulators, like Oiwa's design [29], the workspace is very small because of the limitation of using rotational joints. This novel concept arrangement provides significant advantage where any point within the workspace can be reached by simply controlling the 3 linear actuators.

- Abbé error elimination

  In theory, the angular error due to the effect of Abbé error is eliminated. The axes of measurement of the laser measurement devices intersect with the probe tip, which results in zero offset distance. The probe is moved by moving the linear motors up and down. This movement repositions the entire structure of the tetrahedron, and thus the probe as well.

- Less connections and reduced number of joints

  A further advantage of this system is that there are only three spherical joints on the system. Most similar parallel mechanisms use a combination of rotational or rotational and spherical joints both at the upper end of the measurement arms and at the probe platform. These joints are all prone to

run-out errors. Thus, this concept reduces the total number of joints from six to three. That also may lead to cost reduction.

- Separate measurement and movement loops

Even though, the movement and measurement loops are not completely separated (see Figure 22), a further advantage of this system is that the motors are also not mounted on the measurement arms, thus they do not interfere with lasers. Effects of heat dissipation and vibration resulted from the movement of the motors are minimized. In the figure, the red lines indicate the 'measurement loop' with the measurable distances, including the lengths of the legs 'li' as a direct reading from the laser sensors, where the blue lines indicate the 'movement loop' contains the parts that are responsible for movement, namely the motors (a, b and c). Moving parts are marked with arrows in Figure 22.
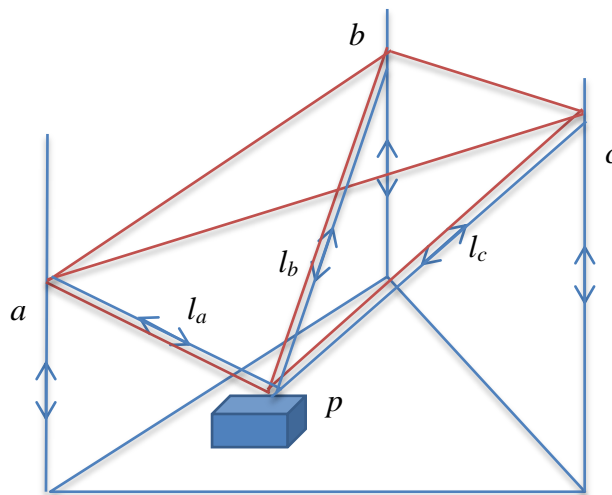
Figure 22: Measurement loop (red lines), and movement loop (blue lines).

3.5.2   Disadvantage of the novel micro-CMM concept

The probe's orientation changes all the time as it moves. This means that some measurements, such as measuring a vertical wall or inside a deep hole, will not be possible. This disadvantage is mitigated to some extent by the fact that the orientation does not change more than 14 degrees. Also, typical micro-manufactured components are not very high compared to their width.

A further disadvantage is the joints. It is very difficult to make spherical joints that provide 3-DOF to precisions high enough for this application. The author plans to mitigate this problem in future, by measuring the run-out error in the spherical joints in real time using capacitive displacement sensors, and then compensating for the error. There is already an on-going research at the University of Stellenbosch to solve this problem.

A typical concept drawing of a spherical joint with three capacitive displacement sensors are shown in Figure 23.
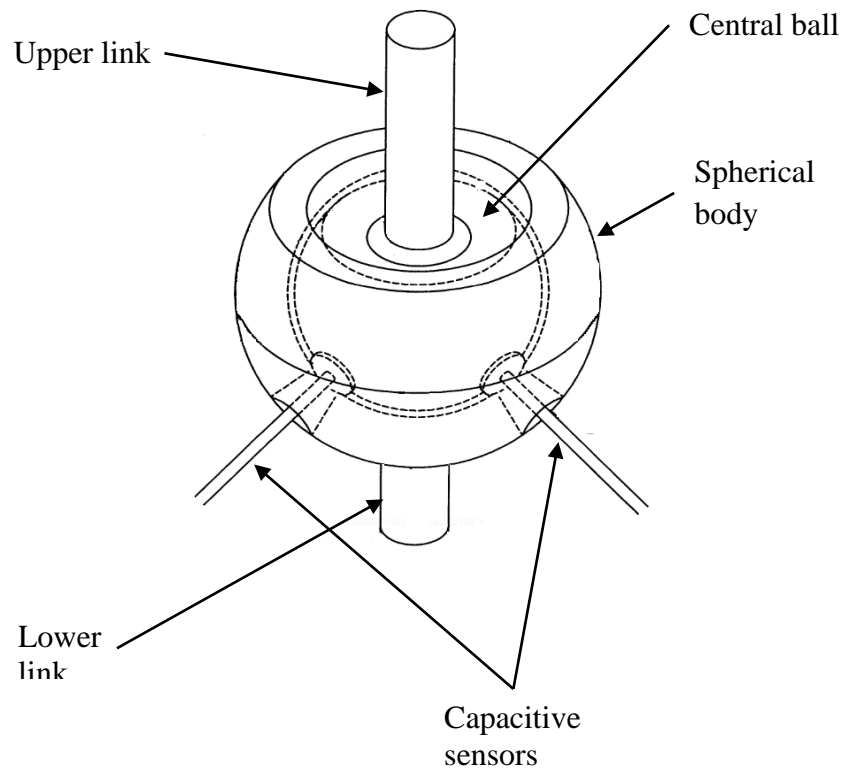
Figure 23: Spherical joint with three capacitive sensors.

CHAPTER 4:

Kinematic modelling of the micro-CMM

4.1   Introduction

In this chapter, the solution to the position kinematic model in the global coordinate system is derived. The reachable workspace is analysed. Derivation of the kinematic error model also presented analytically and numerically.

4.2   Coordinate system

The coordinate system is shown in Figure 24 and Figure 25. The origin $O(0,0,0)$ is placed at the centre of the base. The prismatic joints intersect with the base at

47

points *a, b* and *c*. The *x*-axis equally divides the angle *bac* at point *a*, and the *z*-axis is perpendicular to the base plane (*a,b,c*).
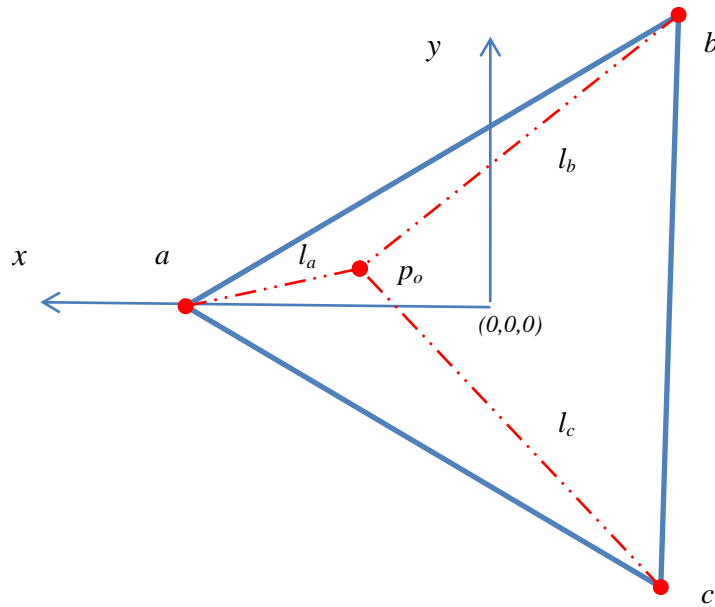
Figure 24: The coordinate system: top view *xy* plane.
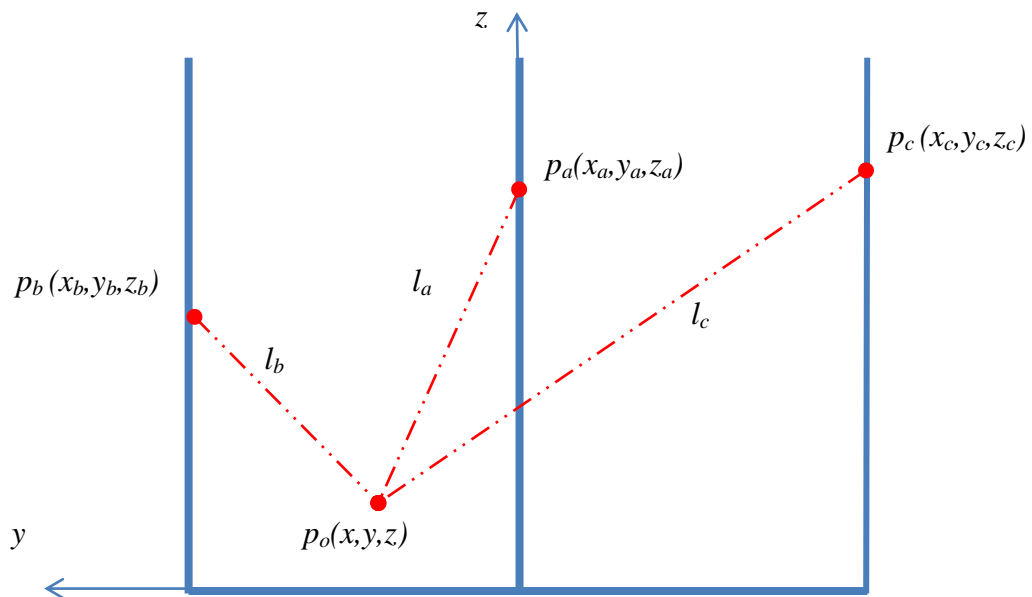
Figure 25: The coordinate system: front view *yz* plane.

48

The geometrical parameters of the micro-CMM are as follows:

l_i : the distance between pivot point of the ball joint p_i and the probe tip p_o.

l_{min}, l_{max} : the maximum and minimum extensions of the arms, l_{min}= 330 mm, l_{max}= 500 mm.

β_i : the angle between the tetrahedron legs l_i, l_{in}, $\beta_a = \beta_b = \beta_c = 68^o$.

The overall height of the machine is 700 mm.

The base frame has an equilateral triangle shape, where the length of each side is 650 mm.

4.3   Kinematic modelling

Parallel mechanism modelling is usually divided in literature into two divisions, namely: kinematic or geometric models and the dynamic model [45].

The position kinematic model mathematically describes the relations between joint coordinates and the probe position and orientation. The change in the probe's pose is defined with respect to the reference coordinate system. While the dynamic model provides a relation between the probe's acceleration, velocity, coordinates and the influence of forces such as inertia, gravity, torque and non-geometric effects such as friction and backlash.

In serial mechanisms, one given joint position vector corresponds to only one end-effector pose. The kinematics problem is not difficult to solve. In contrast, in parallel mechanisms the solution is not unique, since one set of joint coordinates may have different end-effector poses.

In general, the first step in solving the initial position is to create the forward and inverse position kinematic model by formulating the non-linear set of equations that relate the manipulator variables and the probe pose, then in the next step the non-linear equation system can be solved using analytical or numerical methods or even graphical methods in simple mechanisms.

The position kinematic model can be solved by direct or inverse kinematics, depending on the input and output variables.

4.3.1   Development of the kinematic model

A direct position kinematic model (DPKM) is used to calculate the pose of the probe, given the specified values for the mechanism parameters.

The first step in solving the initial position is to create the forward position kinematic model by setting the non-linear set of equations that relate the moving stages' variables and the probe pose. Then in the next step the non-linear equation system are solved analytically.

Assume that the probe tip (x,y,z) is at the main vertex of the moving tetrahedron, which is theoretically the point of intersection of the three laser beams. Because of using spherical joints, the equation of movement of the legs can be expressed by the following governing equations:

$$l_a^2 = (x - x_a)^2 + (y - y_a)^2 + (z - z_a)^2 \tag{1}$$

$$l_b^2 = (x - x_b)^2 + (y - y_b)^2 + (z - z_b)^2 \tag{2}$$

$$l_c^2 = (x - x_c)^2 + (y - y_c)^2 + (z - z_c)^2 \tag{3}$$

From Figure 26 it is clear that values of z coordinate of the moving motors (z_{i+1} and z_{i-1}) can be calculated relative to the z component of the stationary motor (z_i), where the vertical distances between two spherical joints $dz_{i,i+1}$ and $dz_{i-1,i}$ can be calculated provided that the legs l_a, l_b and l_c, as well as angels (β) between them are known.

Let the subscript i and represent (a, b, c) when i rotates around z axes in clockwise direction when seen from above, subscripts ip and in refer to the previous and next points, respectively.

$$z_{in} = z_i + dz_{in} \tag{4}$$

$$z_{ip} = dz_{ip} + z_i \tag{5}$$

$$dz_{in}^2 = (d_{in})^2 - (b_{in})^2 \tag{6}$$

$$dz_{ip}^2 = \left(d_{ip}\right)^2 - \left(b_{ip}\right)^2 \tag{7}$$

$$d_{in}^2 = l_i^2 + l_{in}^2 - 2\, l_i\, l_{in} \cos(\beta_{in}) \tag{8}$$

$$d_{ip}^2 = l_{ip}^2 + l_i^2 - 2\, l_{ip}\, l_i \cos(\beta_{ip}) \tag{9}$$

Where:

i: index of the pivot point of the ith joint, $i = [a,b,c]$

in, ip: index of pivot point of the next and previous pivot points, respectively

dz: the height difference between pivot point of the joint on stationary motor and moving joints

d_{in} and d_{ip}: the distance between i^{th} pivot point and the next and previous pivots, respectively

b_{in} and b_{ip}: the distance between pivot points at $z_{in} = z_i$ and $z_{ip} = z_i$, respectively

β_{in}, β_{ip}: the angles between leg l_i and legs l_{in} and l_{ip}, respectively.

51
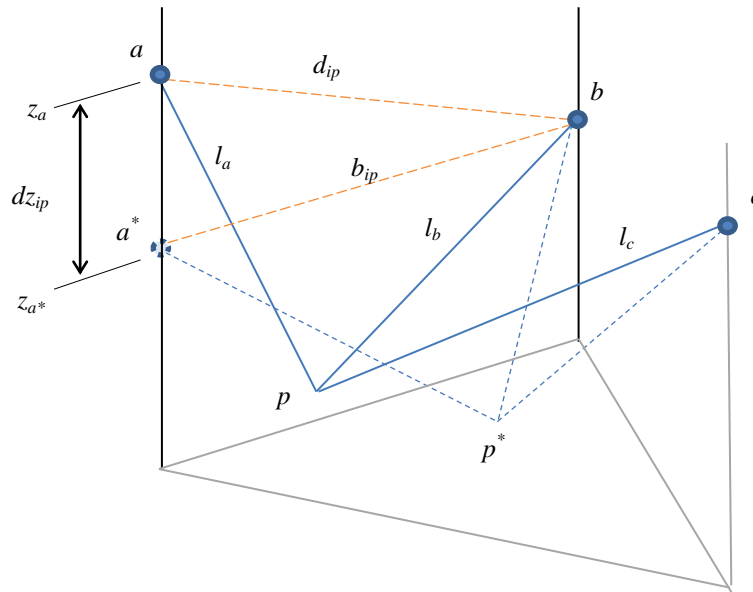
Figure 26: Schematic drawing of the micro-CMM machine
Point *b* is stationary, points *a* and *c* are moving.

Since points *a, b* and *c* move in a linear path, thus their *x* and *y* components can also be defined as a function of the *z* component

$$x_i = g_i + h_i\, z_i \tag{10}$$

$$y_i = m_i + n_i\, z_i \tag{11}$$

Where: *g* and *m* are the intercept, *h* and *m* are the slope of the linear path of the motors.

At the start of the operation *z* is assumed to be equal to zero, or alternatively, the stationary point will have $z = -z_i$, and $z_i = 0$.

Replace for z_b and z_c from equation (4) in equations (1), (2) and (3) to get:

$$l_a^2 - (x_a^2 + y_a^2 + z_a^2) = x^2 + y^2 + z^2 - 2\,x_a\,x - 2\,y_a\,y - 2\,z_a\,z \tag{12}$$

52

$$l_b^2 - \left(x_b^2 + y_b^2 + \left(dz_{a,b} + z_a\right)^2\right) = x^2 + y^2 + z^2 - 2 x_b x - 2 y_b y - 2\left(dz_{a,b} + z_a\right) z \quad (13)$$

$$l_c^2 - \left(x_c^2 + y_c^2 + \left(dz_{c,a} + z_a\right)^2\right) = x^2 + y^2 + z^2 - 2 x_c x - 2 y_c y - 2\left(dz_{c,a} + z_a\right) z \quad (14)$$

Let the left hand parts of the previous equations be equal to c_a, c_b and c_c

$$c_i = l_i^2 - x_i^2 - y_i^2 - z_i^2$$

Subtract equation (13) from equation (12), and equation (14) from equation (12),

$$2 x \left(x_a - x_b\right) + 2 y \left(y_a - y_b\right) - 2 z \, dz_{a,b} = c_b - c_a \quad (15)$$

$$2 x \left(x_a - x_c\right) + 2 y \left(y_a - y_c\right) - 2 z \, dz_{c,a} = c_c - c_a \quad (16)$$

Solve equations (15) and (16) for z to get the following expressions

$$z = x \frac{\left(x_a - x_b\right)}{dz_{a,b}} + y \frac{\left(y_a - y_b\right)}{dz_{a,b}} - \frac{\left(c_b - c_a\right)}{2 \, dz_{a,b}} \quad (17)$$

$$z = x \frac{\left(x_a - x_c\right)}{dz_{c,a}} + y \frac{\left(y_a - y_c\right)}{dz_{c,a}} - \frac{\left(c_c - c_a\right)}{2 \, dz_{c,a}} \quad (18)$$

Eliminate z in the previous 2 equations and solve for x

$$x = A - B \, y \quad (19)$$

Replace for x in equation (17) and solve for z

$$z = F - D \, y \quad (20)$$

Where *A, B, D* and *F* represent the following expressions:

53

$$A = \frac{\left(\dfrac{c_{in} - c_i}{2\,z_{in}} - \dfrac{c_i - c_{ip}}{2\,z_{ip}}\right)}{\left(\dfrac{x_i - x_{ip}}{z_{ip}} - \dfrac{x_{in} - x_i}{z_{in}}\right)}$$

$$B = \frac{\left(\dfrac{y_i - y_{in}}{z_{ip}} - \dfrac{y_{ip} - y_i}{z_{in}}\right)}{\left(\dfrac{x_i - x_{ip}}{z_{ip}} - \dfrac{x_{in} - x_i}{z_{in}}\right)}$$

$$D = \frac{y_{in} - y_i}{z_{in}} - B\,\frac{x_{in} - x_i}{z_{in}}$$

$$F = A\,\frac{x_{in} - x_i}{z_{in}} - \frac{c_{in} - c_i}{2\,z_{in}}$$

The coordinate of the probe location can be found by solving equation (12) and replacing x and z from equations (19) and (20), respectively.

$$y^2(1 + B^2 + D^2) + y(2DF + 2x_aB - 2AB - 2y_a) + A^2 + F^2 - 2x_aA - c_a = 0 \quad (21)$$

This yields explicit expressions for the y coordinates of the centre point of the probe as follows:

$$y = \frac{-v \pm \sqrt{v^2 - 4\,u\,w}}{2\,u} \tag{22}$$

Where: u, v and w can be calculated using the following expressions:

$$u = 1 + B^2 + D^2$$

$$v = 2\,D\,F + 2\,x_i\,B - 2\,A\,B + 2\,y_i$$

$$w = A^2 + F^2 - 2\,x_i\,A - c_i$$

54

Equations (19), (20) and (22) are used to calculate the position of the probe (x,y,z) in the Cartesian coordinate system, given the values for the mechanism variables. These equations represent the direct position kinematic model (DPKM) of the system. Computer code developed with Python version 3.2 is used to solve the DPKM. The code is listed in Appendix B-1.

4.3.2 Inverse kinematic model

An inverse position kinematic model (IPKM) is used to calculate the mechanism's variables for a position of the probe. The IPKM is beneficial to the movement control system of the machine, where the probe pose is defined and the mechanism variables need to be found.

The inverse position kinematic model is created by solving the initial position of the mechanism. In the IPKM the desired probe coordinates are set as the input parameters and the outputs are the mechanism variables. The non-linear set of equations that relate the manipulator variables and the probe pose are solved using numerical methods.

From the non-linear set of equations given by equations (1), (2) and (3), mechanism variables for the IPKM are l_a, l_b, and l_c, and the input parameters are (x,y,z).

Consider the case when motor a is stationary and motors b and c are moving, z_a = constant for the stationary point a. z_b and z_c are calculated using equations (4) – (9) to give the following expressions:

$$z_b = z_a \pm \left(\sqrt[2]{l_a^2 + l_b^2 - 2\, l_a\, l_b\, cos(\beta_b)} - b_{a,b}^2 \right) \tag{23}$$

$$z_c = z_a \pm \left(\sqrt[2]{l_a^2 + l_c^2 - 2\, l_a\, l_c \cos(\beta_c)} - b_{a,c}^2 \right) \tag{24}$$

It is possible now to rewrite equations (1), (2) and (3) to eliminate z_a, z_b, z_c. using the resulted set of nonlinear equations. It is possible to calculate the values for the mechanism variables, given the position of the probe (x,y,z) in the Cartesian coordinate system. These equations represent the inverse position kinematic model (IPKM) of the system. They are very complicated and difficult to solve analytically. To find the roots of the resulting set of equations the nonlinear least-squares algorithms was used based on the Gauss-Newton method.

Computer code developed with Python version 3.2 is used to solve the IPKM. The command optimize.fsolve is useful. The code is listed in Appendix B-2.

4.4   Analysis of the workspace

The reachable workspace of a parallel manipulator is defined as all the positions within the region of the Cartesian space that can be reached by the tip of the probe which is attached to the central point of the platform.

The workspace can be determined using the previously described model. The boundary surfaces of the workspace are calculated taking into account all the geometrical limitations and the movement range of the prismatic joints of the legs (maximum extension l_{max} and the minimum extension l_{min}).

Figure 27 shows a 3D plot of the reachable workspace and the work envelope is represented by the red cube within the workspace in Figure 28 The code used to analyse the workspace is given in Appendix B-3. The processes of constructing the workspace can be summarized as follows:

- Set boundary conditions

$y_{max} = (R_f - x) \, tan(30)$, $y_{min} = -(R_f - x) \, tan(30)$,

$x_{max} = R_f$, $x_{min} = - R_f \, / \, 2$

- Set one leg $l_i = l_{min}$, increase the other two legs by δl from l_{min} to l_{max}.

- Solve the position components (x,y,z) for the outer surfaces $S_{out\text{-}li}$.

- Set one leg $l_i = l_{max}$, increase the other two legs by δl from l_{min} to l_{max}.

- Solve the position components (x,y,z) for the inner surfaces $S_{in\text{-}li}$.

- Repeat for each leg.

- Solve for the side surfaces S_a, S_b, S_c.

    - S_a: $y = (R_f - x) \, tan(30)$, with x in the range $(x_{min} \leq x \leq x_{max})$

    - S_b: $y = - (R_f - x) \, tan(30)$, with x in the range $(x_{min} \leq x \leq x_{max})$

    - S_c: $x = x_{max}$ and y in the range $(y_{min} \leq y \leq y_{max})$
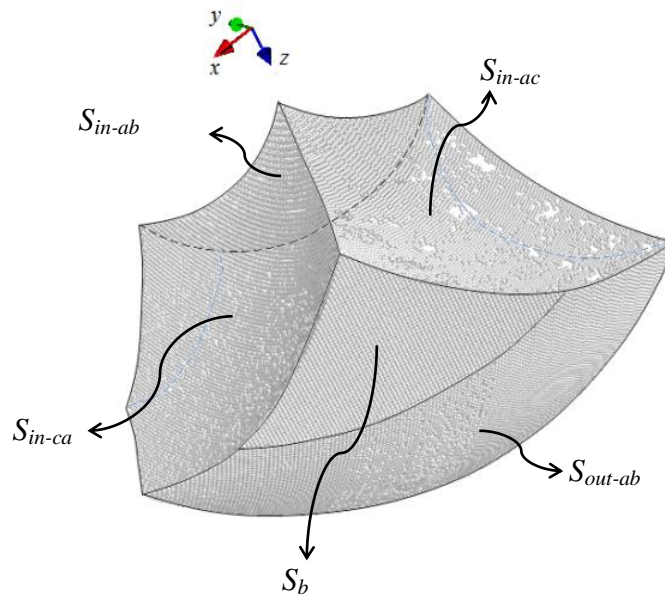
Figure 27: 3D plot of the reachable workspace.

57
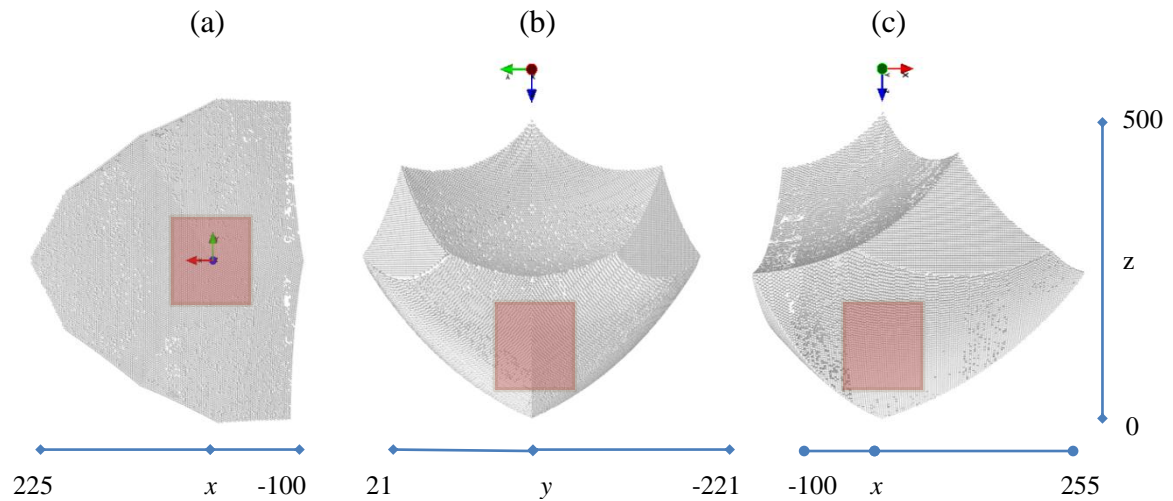
Figure 28: The reachable workspace of the micro-CMM. (a) top view; (b) front view; (c) side view.

The results of workspace calculations illustrated in Figure 27 and Figure 28 show that: (1) The workspace is formed by surfaces cascaded together. (2) The workspace is symmetric about the xz plane. (3) The workspace range in xy plane vanishes at z_{min} where $l_a = l_b = l_c$, and reaches its maximum range when two legs are maximum and the third is minimum, then the range decreases as z increases and vanishes at $z > 500$ mm when $l_a = l_b = l_c = l_{max}$. The red cube in the workspace represents the work envelope (100x100x100) mm. This proves that this design can easily achieve the goal of 100x100x100 mm work envelope.

4.5   Modelling of the kinematic error

The positioning accuracy of parallel mechanisms is usually limited by many errors. Some authors identified the errors affecting the precision of parallel mechanisms as follows [52], [59 − 61]: manufacturing errors, assembly errors, errors resulting from distortion by force and heat, control system errors and actuators errors, calibration, and even mathematical models. These errors should be divided into two main sources: static errors for those not dependent on the

58

dynamics and process forces, and dynamic errors for errors due to the movement and measuring method [62].

4.5.1   Analytical kinematic error model

Suggesting an error model for the proposed machine is of great importance in order to evaluate the structure and understand the effect of the different parameters on its accuracy. The derivation of the covariance matrix is well known and can be found in [98] and [99]. For more clarification the details of the derivation will be given here:

Function $F(x)$ can be represented by its Taylor series as follows:

$$F(x) = F(\bar{x}) + J(\bar{x}) \,.\, (x - \bar{x}) + (\varepsilon \|x - \bar{x}\|^2) \tag{25}$$

Where: $J(x)$ is the Jacobian matrix of $F(x)$, and ε is the error term, $\bar{x}$ is the average of all x samples.

Let's assume that the last term is small enough to be neglected. Then the previous equation can be rewritten as:

$$F(x) - F(\bar{x}) = J(\bar{x}) \bullet (x - \bar{x}) \tag{26}$$

The formula for computing the covariance is:

$$\Lambda_F = \frac{1}{n-1} \big(F(x) - F(\bar{x})\big) \bullet \big(F(x) - F(\bar{x})\big) \tag{27}$$

Replacing the dot product by the transpose of two matrices $A \bullet B = A^T B$, we get:

$$\Lambda_F = \frac{1}{n-1} \big(F(x) - F(\bar{x})\big)^T \big(F(x) - F(\bar{x})\big) \tag{28}$$

59

Replace equation (26) in equation (27) to get:

$$\Lambda_F = \frac{1}{n-1}\big(J(\bar{x}) \bullet (x - \bar{x})\big)^T \big(J(\bar{x}) \bullet (x - \bar{x})\big) \tag{29}$$

Remember, the dot product is commutative $A \bullet B = B \bullet A$, and $(AB)^T = B^T A^T$, then Λ_F can be rewritten as:

$$\Lambda_F = \frac{1}{n-1} J(\bar{x}) \, (x - \bar{x})^T (x - \bar{x}) \big(J(\bar{x})\big)^T \tag{30}$$

Since the covariance matrix of x is:

$$\Lambda_x = \frac{1}{n-1} \, (x - \bar{x})^{\mathrm{T}} (x - \bar{x}) \tag{31}$$

Then the covariance matrix can be written as:

$$\Lambda_F = J(\bar{x}) \, \Lambda_x \, J(\bar{x})^{\mathrm{T}} \tag{32}$$

The last equation is very useful to determine the covariance matrix using the input covariance and the Jacobian of the process function.

In this study, the error of each stage (or link) is a combination of errors in the leg lengths l_i and the position of each spherical joint p_i in the Cartesian coordinate system.

These measurement errors are created mainly by the error in the spherical joints es_i, parallelism in the runner blocks eb_i, backlash in the motors em_i, capability of the laser distance sensor er_i, angular errors of the actuator, cosine error $ecos_i$, and Abbé error eab_i. Elastic deformations and deflection of the moving structure is represented by the small change in the angle between the legs of the tetrahedron

$e\beta_i$. Probe error and effects of thermal expansions were not included in the error model.

Therefore, in total 24 parameters will be investigated. For each link, *eab*, *er* and *ecos* will be combined and together will contribute to *el*. A full size Jacobian matrix is used in carrying out error analysis. The Jacobian consists of the first-order partial derivatives of *x, y* and *z* in equations (19), (20) and (22), respectively, with respect to the error sources. The Jacobian needed is organized in a 3×15 matrix, as follows:

$$J = \begin{bmatrix} \frac{\partial x}{\partial x_a} & \frac{\partial x}{\partial x_b} & \frac{\partial x}{\partial x_c} & \frac{\partial x}{\partial y_a} & \frac{\partial x}{\partial y_b} & \frac{\partial x}{\partial y_c} & \frac{\partial x}{\partial z_a} & \frac{\partial x}{\partial z_b} & \frac{\partial x}{\partial z_c} & \frac{\partial x}{\partial l_a} & \frac{\partial x}{\partial l_b} & \frac{\partial x}{\partial l_c} & \frac{\partial x}{\partial \beta_a} & \frac{\partial x}{\partial \beta_b} & \frac{\partial x}{\partial \beta_c} \\ \frac{\partial y}{\partial x_a} & \frac{\partial y}{\partial x_b} & \frac{\partial y}{\partial x_c} & \frac{\partial y}{\partial y_a} & \frac{\partial y}{\partial y_b} & \frac{\partial y}{\partial y_c} & \frac{\partial y}{\partial z_a} & \frac{\partial y}{\partial z_b} & \frac{\partial y}{\partial z_c} & \frac{\partial y}{\partial l_a} & \frac{\partial y}{\partial l_b} & \frac{\partial y}{\partial l_c} & \frac{\partial y}{\partial \beta_a} & \frac{\partial y}{\partial \beta_b} & \frac{\partial y}{\partial \beta_c} \\ \frac{\partial z}{\partial x_a} & \frac{\partial z}{\partial x_b} & \frac{\partial z}{\partial x_c} & \frac{\partial z}{\partial y_a} & \frac{\partial z}{\partial y_b} & \frac{\partial z}{\partial y_c} & \frac{\partial z}{\partial z_a} & \frac{\partial z}{\partial z_b} & \frac{\partial z}{\partial z_c} & \frac{\partial z}{\partial l_a} & \frac{\partial z}{\partial l_b} & \frac{\partial z}{\partial l_c} & \frac{\partial z}{\partial \beta_a} & \frac{\partial z}{\partial \beta_b} & \frac{\partial z}{\partial \beta_c} \end{bmatrix} \qquad (33)$$

The related variances matrix is given by the following 15×15 diagonal matrix:

$$\Lambda_p = \begin{bmatrix} \sigma_{x_a}^2 & 0 & \cdots & 0 \\ 0 & \sigma_{x_b}^2 & & \\ \vdots & & \ddots & \\ 0 & 0 & \cdots & \sigma_{\beta_c}^2 \end{bmatrix} \qquad (34)$$

In the previous matrix the variance along the diagonal is given for, x_a, x_b, x_c, y_a, y_b, y_c, z_a, z_b, z_c, l_a, l_b, l_c, β_a, β_b, β_c. Precision error values are mostly considered as three times the standard deviation value ($\varepsilon = 3\sigma$). Thus, the variance can be estimated by:

$$\sigma_p{}^2 = \left(\frac{\varepsilon_p}{3} \right)^2 \qquad (35)$$

Where: $\sigma_p{}^2$ and ε_p are the variance and the error of the parameters, respectively.

Error in the link el_i includes: the error due to uncertainty in determination of the lengths of the legs ed_i, laser sensor reading er_i, cosine error $ecos_i$ and Abbé error eab_i. Therefore, the variance $\sigma_{l_i}^2$ must be determined based on the same principle.

$$el_i = ed_i + er_i + ecos_i + eab_i \tag{36}$$

Computer code developed with Python is used to overcome the heavy computational cost of solving the analytical error model. The code is listed in Appendix B-4.

4.5.2 Monte-Carlo simulation

In Monte-Carlo studies, random parameter values are generated from an allowed error range. A large number of runs are carried out, and the position is estimated for each run. Parameter values and standard errors are averaged over the samples.

The Monte-Carlo simulations have been used as uncertainty evaluation for CMMs in [100 − 103]. This method was documented in an ISO document [7]. In this study simulations have been performed to examine the validity of the analytical error model. Computer software developed with Python was used to overcome the amount of work needed for the simulation.

The standard deviation of the probe coordinate is calculated at several deferent positions within the work envelope. At each position the standard deviation is calculated passed on the results of the huge number of Monte-Carlo iterations (n). In each run m, ($m = 1,…, n$), a random error value is added to each variable.

Let V represent the 24 system variables, where $V = [x_i, y_i, z_i, d_i, r_i, cos_i, ab_i, \beta_i]$, and eV represent the maximum amount of error associated with that variable. Then new estimated values for the variables dV_m are estimated at each iteration m, where $m = 1,..,n$.

62

$dV_m = V + \delta V_m$

Where δV_m is a random error value added or subtracted from the variables as per the following, where R is a random value in the range (0, 1).

$\delta V_m = 2\ eV\ R - eV$

This will eventually create samples of *x, y* and *z* of *n* values each. Standard deviations and errors are averaged over the samples.

The equations (19), (20) and (22) of the kinematics problem must be rewritten as follows:

$$y_m = \frac{-h \pm \sqrt{h^2 - 4\ g\ k}}{2\ g} \tag{37}$$

$$x_m = A_m - B_m\ y_m \tag{38}$$

$$z_m = F_m - D_m\ y_m \tag{39}$$

Where *A, B, D* and *F* represent the following expressions:

$$A_m = \frac{\left(\dfrac{c_{in,m} - c_{i,m}}{2\ z_{in,m}} - \dfrac{c_{i,m} - c_{ip,m}}{2\ z_{ip,m}}\right)}{\left(\dfrac{x_{i,m} - x_{ip,m}}{z_{ip,m}} - \dfrac{x_{in,m} - x_{i,m}}{z_{in,m}}\right)}$$

$$B_m = \frac{\left(\dfrac{dy_{i,m} - dy_{in,m}}{z_{ip,m}} - \dfrac{dy_{ip} - dy_i}{z_{in,m}}\right)}{\left(\dfrac{dx_{i,m} - dx_{ip,m}}{dz_{ip,m}} - \dfrac{dx_{in,m} - dx_{i,m}}{dz_{in,m}}\right)}$$

$$D_m = \frac{dy_{in,m} - dy_{i,m}}{z_{in,m}} - B_m\ \frac{dx_{in,m} - dx_{i,m}}{z_{in,m}}$$

63

$$F_m = A_m \frac{dx_{in,m} - dx_{i,m}}{z_{in,m}} - \frac{c_{in,m} - c_{i,m}}{2\, z_{in,m}}$$

And similarly, *g, h* and *k* can be calculated using the following expressions:

$$g = 1 + B_m{}^2 + D_m{}^2$$

$$h = 2\, D_m\, F_m + 2\, x_{i,m}\, B_m - 2\, A_m\, B_m + 2\, y_{i,m}$$

$$k = A_m{}^2 + F_m{}^2 - 2\, x_{i,m}\, A_m - c_{i,m}$$

the standard deviation is:

$$\sigma_x^2 = \frac{1}{n} \sum_{m=1}^{n} (x_m - \bar{x})^2$$

$\bar{x}$ is the overall average *x* values:

$$\bar{x} = \frac{1}{n} \sum_{m=1}^{n} x_m$$

Computer code developed with Python for estimation Monte-Carlo simulation is given in Appendix B-5.

CHAPTER 5:

Computer controlled measurement

5.1   Introduction

This chapter describes the development and construction of the computer measurement interface and the machine control control algorithm for the micro-CMM apparatus control system. It also describes the user interface of the software developed for controlling and taking measurements using the machine, based on National Instruments LabView [104].

65

5.2   Programing environment

National Instruments LabView is a general purpose programming environment. It is a graphical programming language that is powerful in automation control and data acquisition. Moreover, its graphical representations provide an intuitive programming environment for scientists and engineers. The key features of LabView, such as simple network communication and turnkey implementation of common communication protocols (RS232, USB, GPIB, etc.), makes LabView a very good automation environment choice [105]. Another advantage of using LabView is the flexibility to call software codes written with other programing languages, such as Python, which is used to solve the inverse and direct kinematics problems.

For the purpose of this study, programming with LabView was preferred over programming in other software like Visual Basic or C++ for a number of reasons. Most importantly, LabView offers the convenience of simultaneous control of all independent components of the machine. Furthermore, the software flexibility, when choosing the hardware components, and the capability of further system improvements, makes LabView a less tiresome progrmming language [90].

LabView monitors the systematic parameters by gathering the readings of the instruments through data acquisition cards (DAQ). Moreover, LabView has a powerful toolset for process control and data fitting that is capable of analysing and controlling the input data signal. Measurements can become easy to reproduce since the software allows logging, saving and loading data.

In order to fully control the operation of the micro-CMM, the devices and sensors were connected; that include the linear motors, laser distance sensors, and the touch trigger probe. A photograph of the computer system used to control the machine is shown in Figure 29.
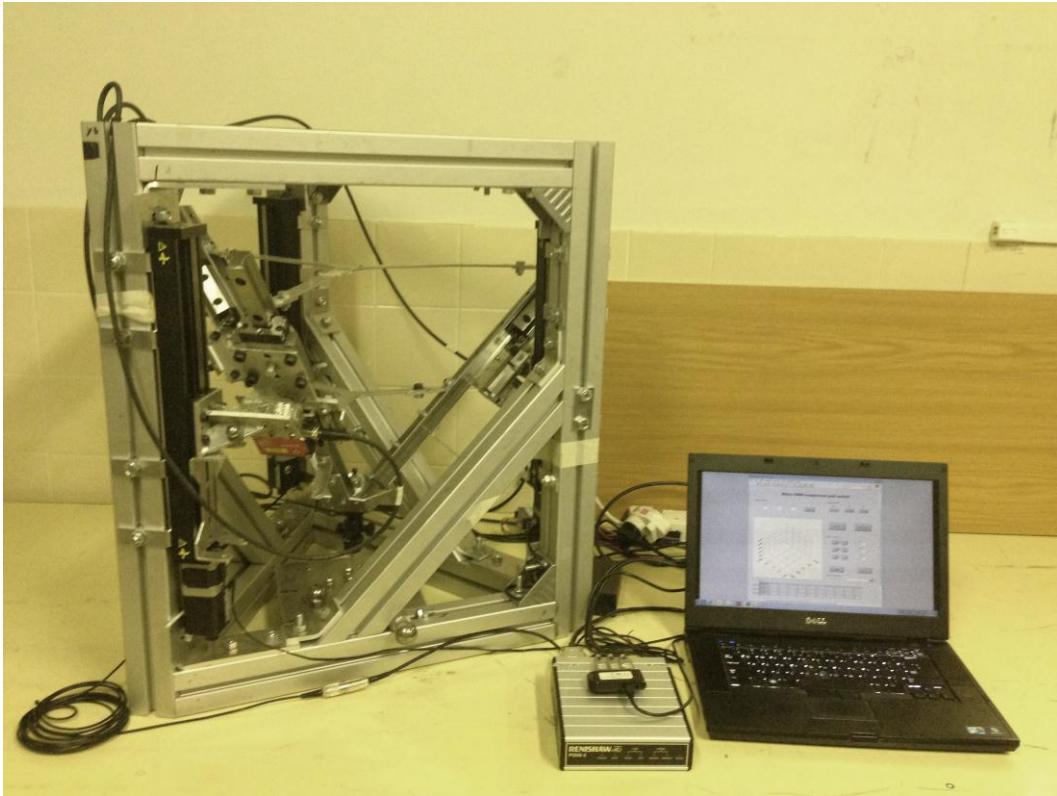
Figure 29: Photograph of the computer control system.

5.3   Programming the machine control system

This computer control system is developed and implemented to be able to fully control the system variables and manipulate the movement of the probe, and to take and record the measurements.

5.3.1   Movement control module

The movement control allows the user to move the probe to a certain position (P) on the workspace. Point P(x,y,z) can be found by solving the direct kinematics model (DPKM), where the input parameters to the DPKM include: readings from the three laser distance sensors (r_a, r_b and r_c) and the coordinate of the pivot points of the spherical joints (p_a, p_b and p_c).

The x and y components of the pivot points are accurately identified during the geometrical identification step, z components represent the axial movement of the ball joints and must be calculated by solving the inverse kinematics model (IPKM) of the machine.

The following steps summarize the movement control model of the machine:

1- Input desired position P.

2- Solve IPKM for a desired position $P(x,y,z)$, the numerical solution gives z_a, z_b and z_c.

3- Move first motor to the new location (z_a) while the other two motors remain stationary.

4- Acquire readings from the laser distance sensors to get the distance from the pivot points of the ball joints to the probe (r_a, r_b and r_c).

5- Use the sensor reading of the first and second laser sensors to apply cosine rule and calculate the height difference between first (moved) and second (stationary) pivot points $dz_{a,b}$.

6- Use z_b (the height of the second point of the stationary motor) to calculate the new position of the first pivot point due to moving the first motor, $z_a^* = dz_{a,b} + z_b$.

7- Compare z_a^* calculated in the last step with z_a calculated in step 1. If there is an error the difference must be added to z_a and steps 2 to 6 must be repeated till z_a is reached.

8- Repeat from step 2, keep first and third motors stationary and move the second motor, using r_b, r_c and z_b, z_c in the calculations till z_b is reached.

9- Repeat from step 2, keep second and third motors stationary and move the third motor, using r_a, r_c and z_a, z_c in the calculations till z_c is reached.

10- Find probe location $P(x,y,z)$ by solving DPKM, use laser sensors readings and pivot points locations as input parameters.

When approaching the object and expecting measurement, the probe must move slowly, this can be done by dividing the travel distance from current position to the desired position into several segments. Once the probe comes in contact with the object it will trigger a signal and the motor will stop immediately then the DPKM will be solved using the acquired reading from the laser sensors.

In a closed-loop control, feedback measurements must be made to indicate the current value of the variable controlled by the loop. The measurement signals to the control system from the laser distance sensors are continuously acquired and the DPKM is calculated. Then the calculated position is compared to the desired set position entered into the control system. Based on a comparison of the values, the control system can tell whether the measurement position achieved the set point, and develop the output signals to the motor accordingly until the probe comes to its final desired destination (set point). The output signal value (volts) depends on the difference between the desired set position and the current DPKM results. Figure 30 shows a block diagram of the movement control module of the micro-CMM machine. The block diagram of the position calculation is given in Figure 31.

5.3.2   Measurement control module

The probe location in space can be achieved by solving the DPKM. When the probe comes into contact with an object, a signal is immediately sent to the computer control system; this signal triggers the measurement control module and stops any motor movement. Then the DPKM is solved to define the probe position.

The following steps summarize the steps of the measurement control model of the machine:

1.   Signal trigger when the probe makes contact with an object.

69

2. Stop motors.

3. Acquire readings from the laser distance sensors to get the distance from the pivot points of the ball joints to the probe (r_a, r_b and r_c)

4. Solve DPKM, use laser sensors readings and pivot points locations as input parameters to find probe location P(x,y,z).

5. Record point P.

This type of control is an open-loop control (no feedback), see Figure 32.

.

Motor controller; $i = a, b, c$
When $i = c$ *make* $in = a$
$i = a$ *make* $ip = c$

Input target position (x,y,z)

Solve IPKM,

z_{ip}, z_i, z_{in}

Move motor i to new position z_i

Read laser distance sensors

r_{ip}, r_i, r_{in}

Solve DPKM

Output position (x,y,z)

dz_{in}

Calculate dz
$dz_{in} = r_i^2 \, r_{in}^2 - 2 \, r_i \, r_{in} \, cos(\beta)$
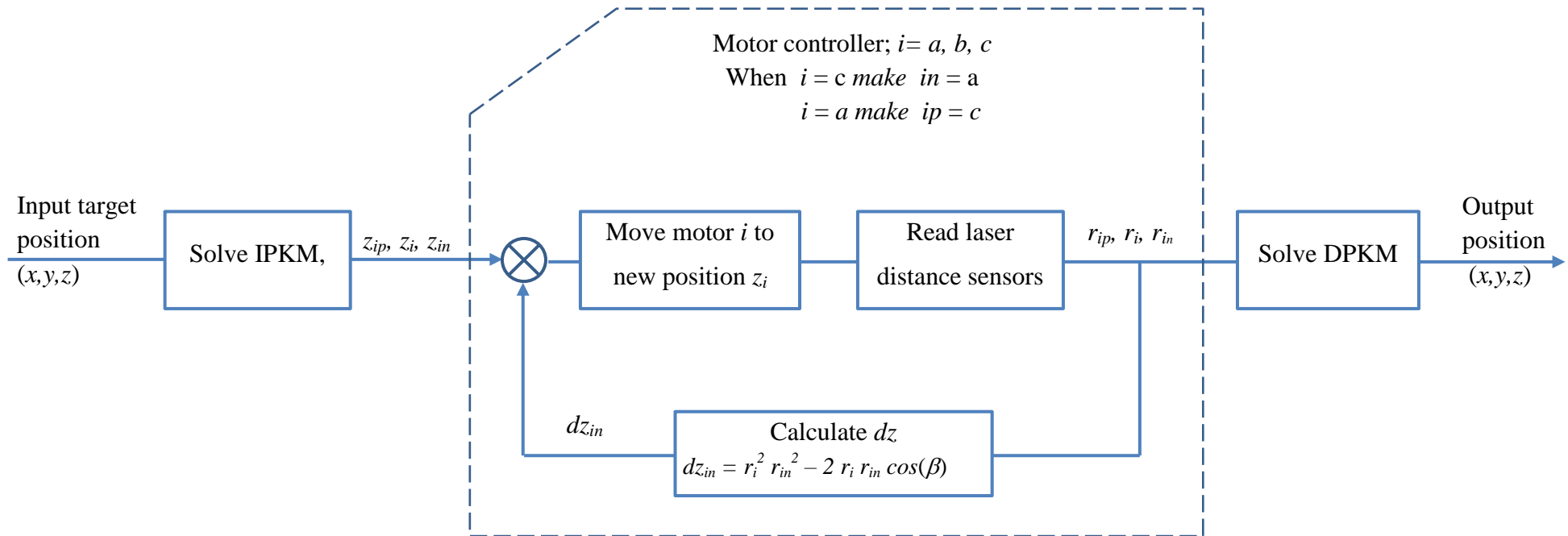
Figure 30: Block diagram for the movement control module.
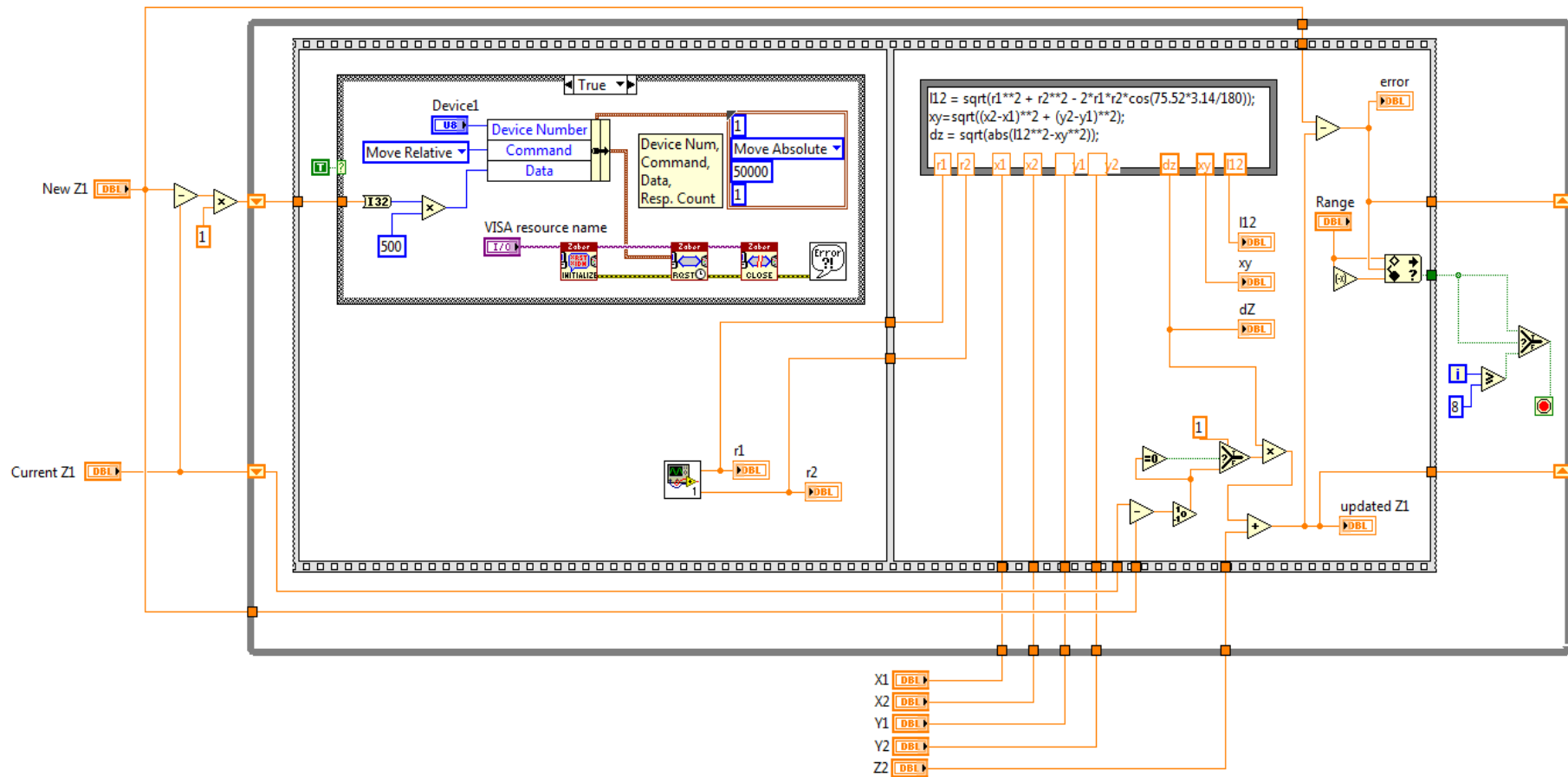
Figure 31: Block diagram of the movement algorithm.
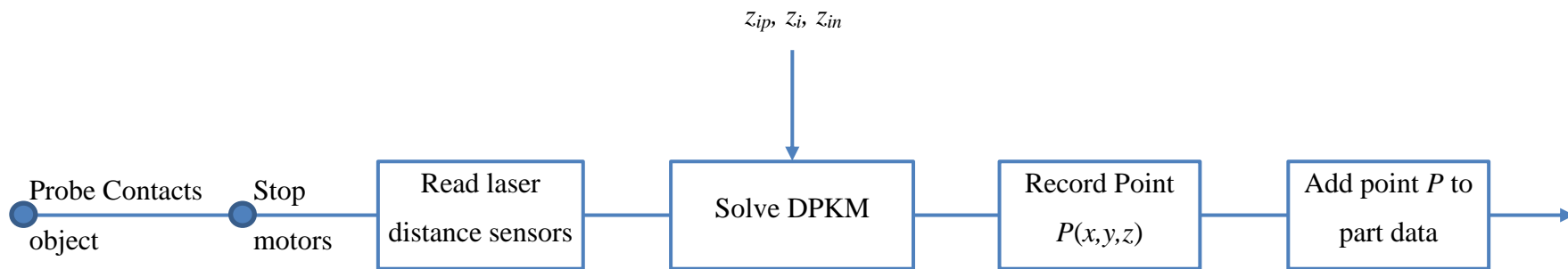
Figure 32: Block diagram for the measurement control module.

5.3.3 Display module

The objective of the display module is to measure and send the signals to the control system to be displayed and used for further calculations. The measurement signal from the sensors is continuously indicating the current value of the laser sensors (lengths of arms), these readings are used to continuously solve the IPKM to define the location of z_a, z_b and z_c. Figure 33 illustrates the computer display module. This is very important to solve the IPKM with every motor move to keep the positions of z_i known.
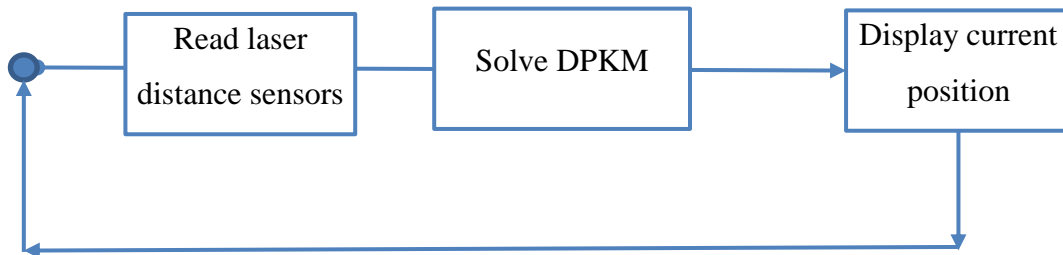
Figure 33: Block diagram for the display control module.

5.3.4 Control flow chart

The final flow chart of the measurement and control software is illustrated in Figure 34.
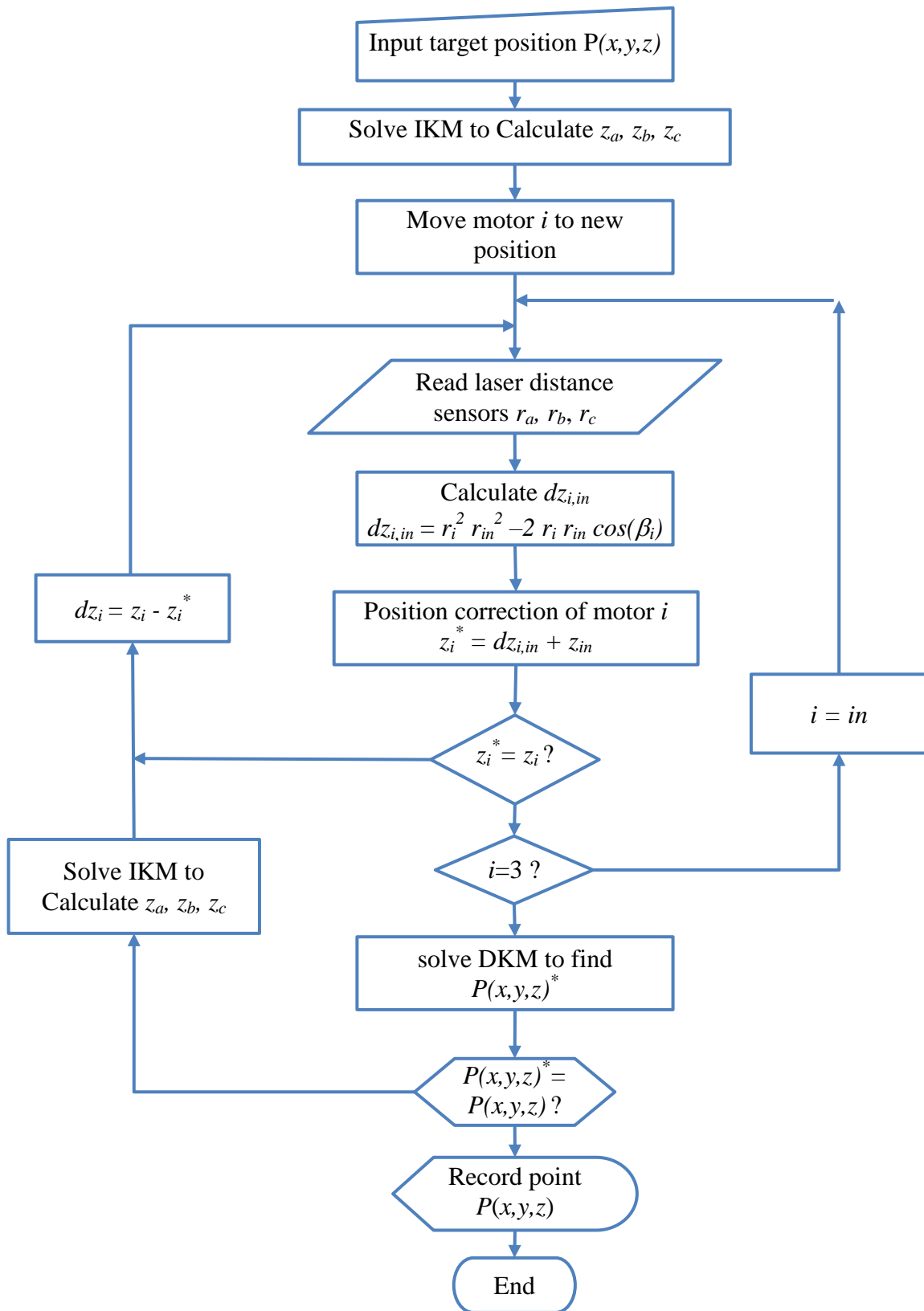
Figure 34: Flow chart of the measurement and control software.

5.4 User interface

Figure 35 shows the main user interface of the program after all the modifications have been done, with short descriptions of each feature.
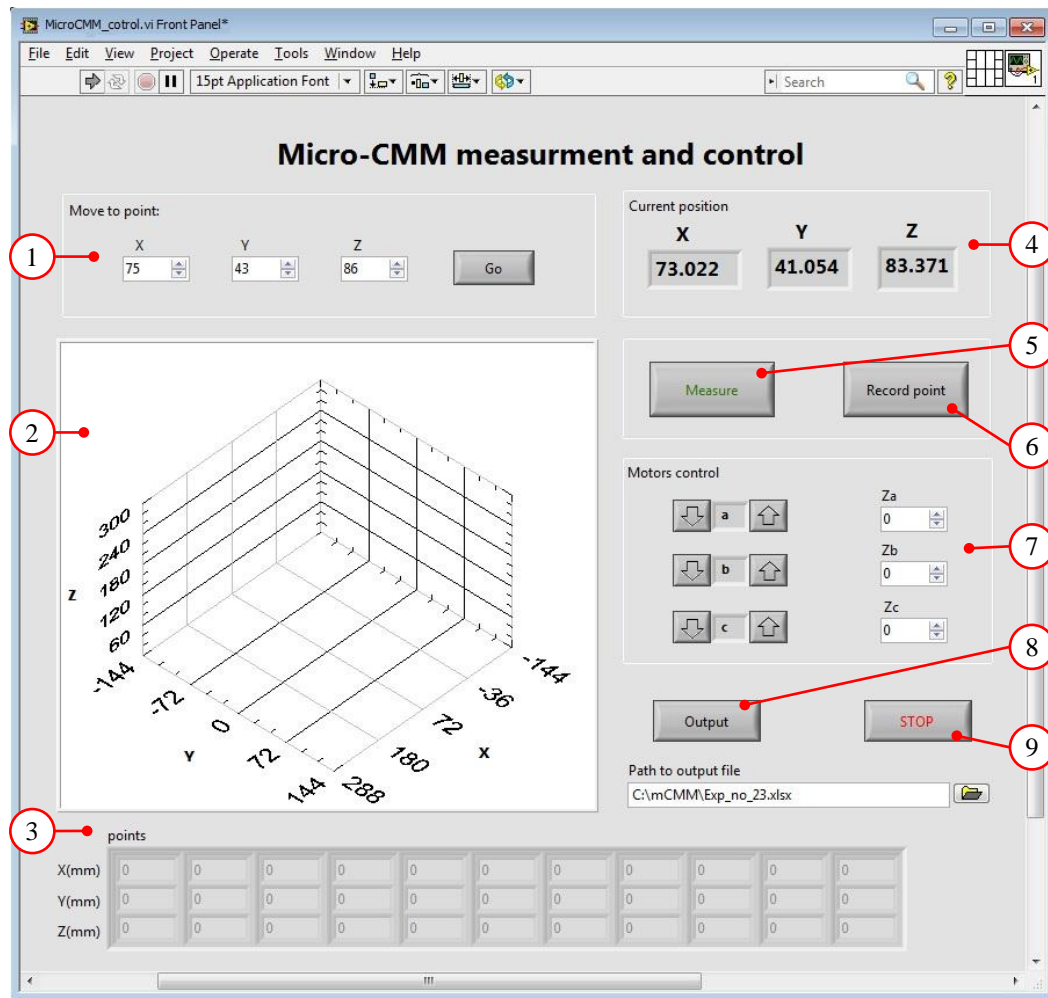
1: Destination/desired position   6: Record last reading

2: Measured points in 3D   7: Manually move motors

3: List of measured points   8: Export file

4: Current probe position   9: Stop the machine

5: Expect measurement

Figure 35: User interface of the control software.

CHAPTER 6:

Parameter identification

6.1 Introduction

Careful identification of the system parameters is very important. This chapter describes a number of experiments done to determine values for the system parameters, as well as the corresponding parametric errors. The results of the parameter identification step will provide the necessary information to solve the kinematics problem and the error modelling as well as the calibration of the machine.

77

6.2 Parameter identification and calibration

Calibration of the novel micro-CMM under study was performed by the means of a Mitutoyo CMM Bright Apex 710, which is available at the metrology laboratory of the Stellenbosch University. The CMM has a volumetric accuracy of 5 µm as per the last calibration. The main cause of errors is a result of geometrical deviation of the structure and the legs due to the weight of the machine, errors caused by the process of manufacturing and assembling of the machine components, run out error in the joints caused by the motion of machine and elastic deformation of the frame structure.

6.2.1 Coordinate setup

Before starting with the calibration process of the micro-CMM, a permanent coordinate reference relative to the structure was introduced. This coordinate system is important for any future calibration or parameter identification. Reference standard ball (*O*) was used to represent the origin (see Figure 36). Ball *O* is attached to the middle of the lower horizontal frame connecting points *a* and *b*. The *xz* plane is parallel to the outer surface of the frame, and plane *xy* is parallel to the upper surface of the same frame.
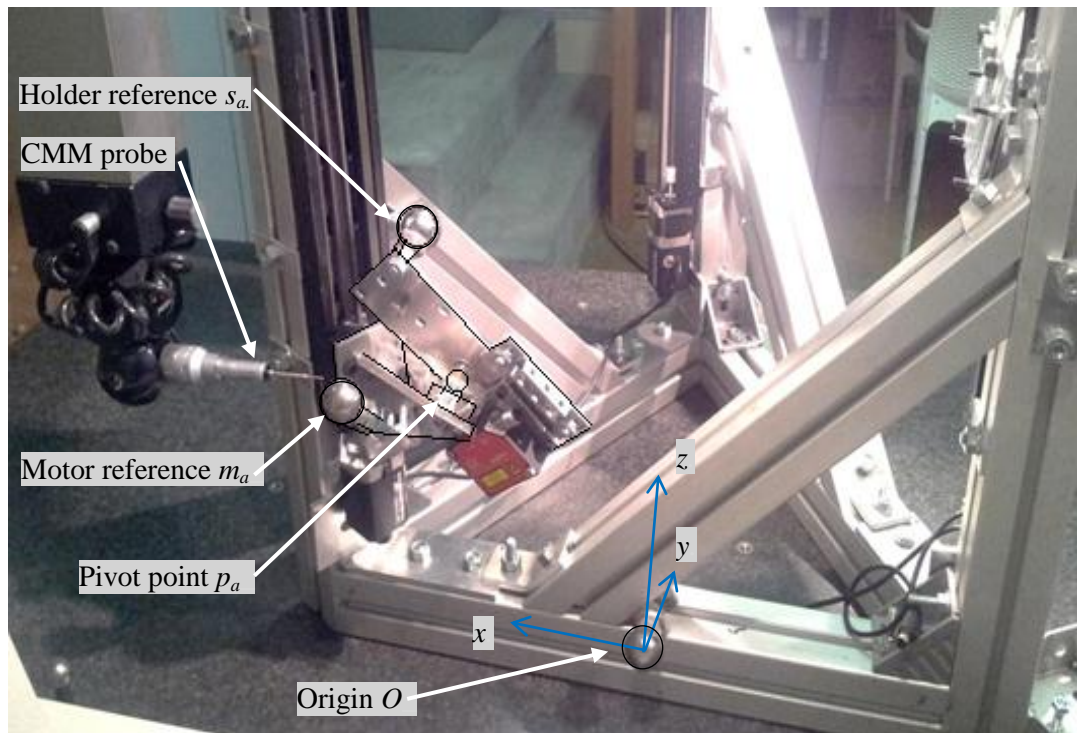
Figure 36: Photograph of the structure setup.

6.2.2   Motion path of pivot points

The spherical joints are connected by brackets to the linear motors. This gives a translational movement in the vertical direction. The linear path of movement is identified by the following technique: reference balls (m_i) are attached to each bracket of the three motors. The master CMM is used to measure m_i at six different positions along the horizontal path of the moving motors. At each position the spherical joints' pivot points p_i were calculated using another standard balls (s). Ball s_i is attached to the base of the runner block holder. Figure 37 illustrates the pivot point and the location of the reference balls p, s and m, respectively, for one of the links.

The centre of s_i was measured at least at 8 different positions, the centre of a sphere fitting of the points' s_i's represent point p_i.

79
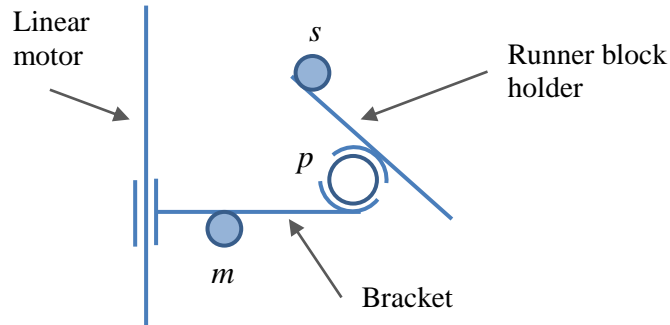
Figure 37: Spherical joint (p) and reference balls (m) and (s).

To identify the linear path of movement of the motor and the support, sphere fitting is performed to determine pivot points p_i at 6 positions of point m_i. Considering the fact that distance m_i–p_i is supposed to be always fixed; the position of point p_i can be determined with respect to the position of point m_i. The CAD drawing for these measurements is displayed in Figure 38.
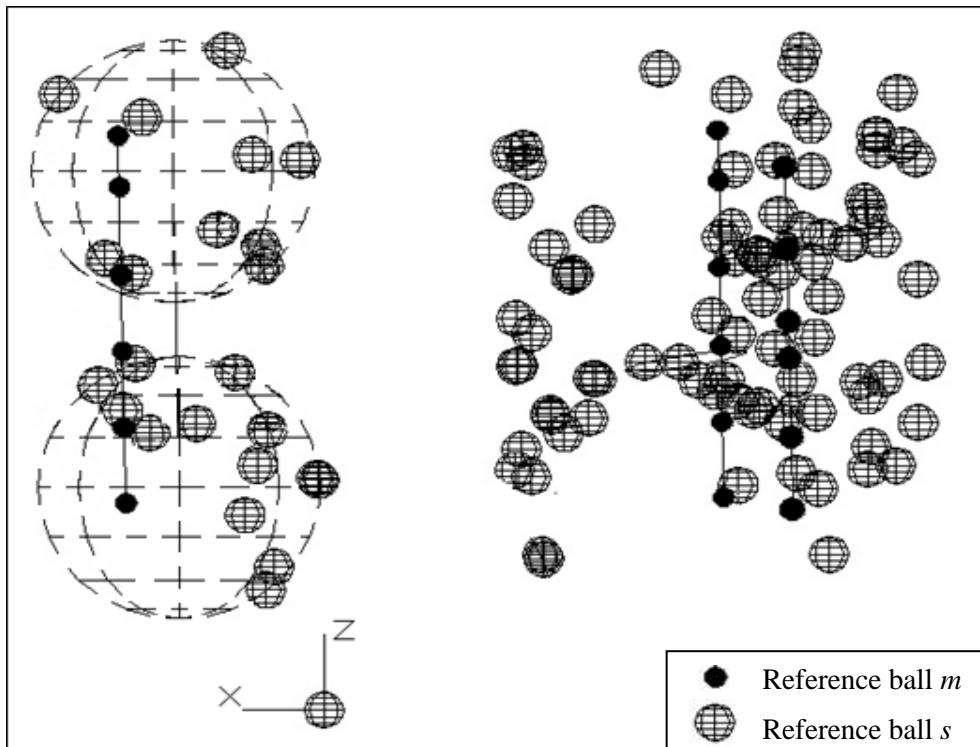
Figure 38: Pivot points determination, measurement taken by means of CMM.

In Figure 38, the centres of the solid black spheres represent points m_i, the hollow spheres represent ball s_i, and the centre of the big dashed spheres represent point p_i. The figure shows the measurements of m_i at 6 positions, and for clarity, measurements taken for s_i are shown at only 2 positions of m_i, namely position no.1 and position no. 5. Figure 39 and Figure 40 show the calculated position p_i of spherical joints a, b and c, as well as the linear path of movement in x and y directions, respectively. The x and y coordinate components are calculated as a function of the z component.
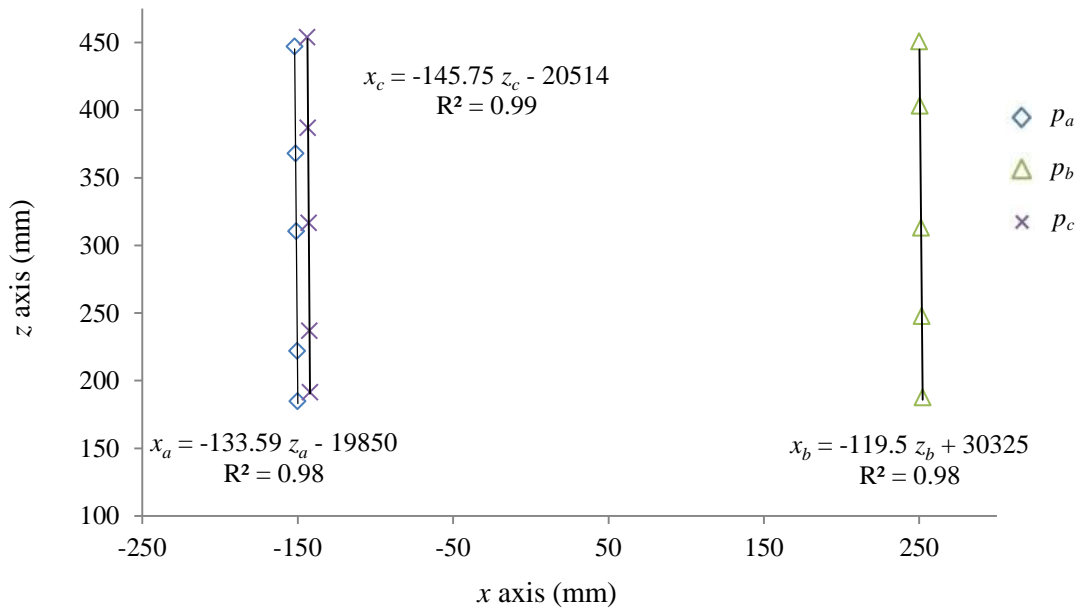
Figure 39: Calculation of points p_i, xz plane.
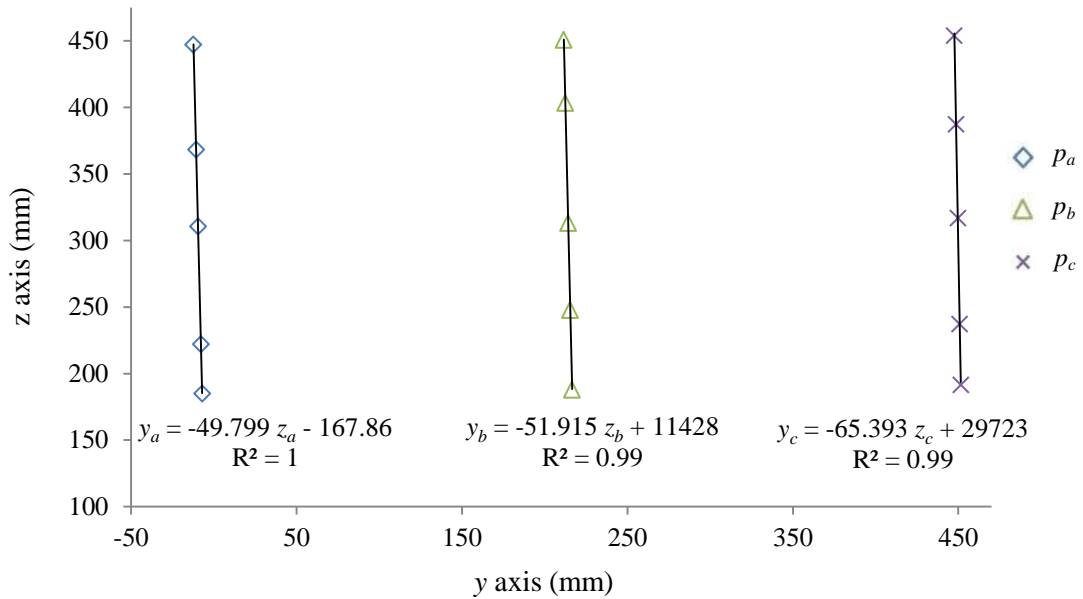
Figure 40: Calculation of points p_i, yz plane.

The linear motion error was estimated as the difference between the calculated values for p_i based on CMM measurements, and the position calculated using the set of equations given in Figure 39 and Figure 40. Standard deviations in the x direction for points a, b and c are (0.015, 0.035, 0.010) mm, respectively. In the y direction they are (0.013, 0.016, 0.041) mm, respectively.

6.2.3   Tetrahedron geometry

In this step the geometrical parameters of the tetrahedron were measured. Figure 41 shows the tetrahedron while taking measurements using the master CMM. The angles between the legs and the distance between the leg outer surface and the probe tip were measured. Figure 42 shows the results of the CMM measurements.

82
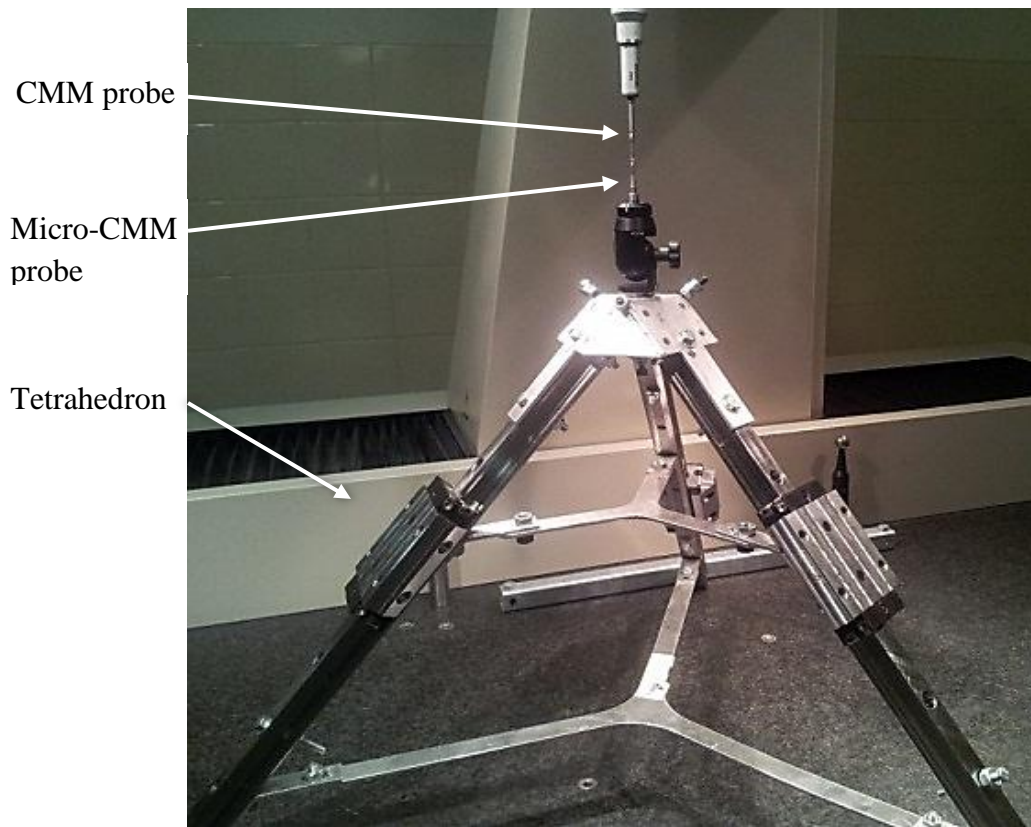
Figure 41: Parameter identification of the moving part, fixed tetrahedron.
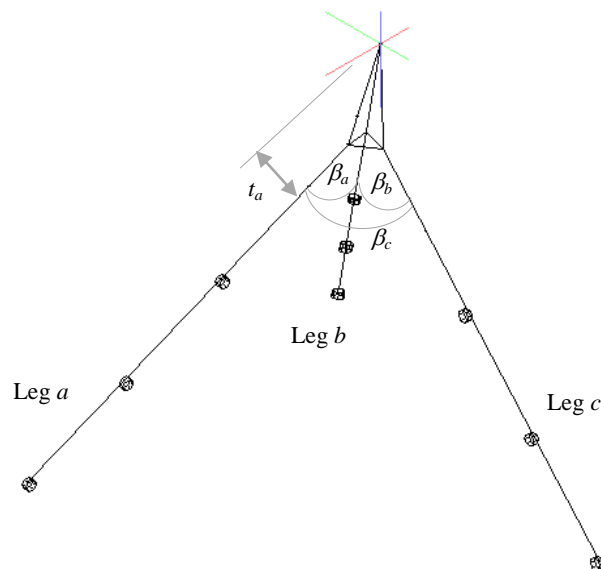
Figure 42: Determination of the tetrahedron geometry,
measurements taken by means of CMM.

Once the geometrical parameters are determined for the structure and the moving part, the micro-CMM is assembled, and further investigation is done to confirm the measurements and correct for any errors due to the assembly process. The geometric parameters of the tetrahedron are tabulated in Table 4.

Table 4: Geometry parameters of the tetrahedron

	Angle between legs β_i	Distance t_i (mm)
Leg a	68.746°	37.333
Leg b	68.545°	38.953
Leg c	68.638°	37.141

6.2.4   Dead distance

Dead distance on the link is fixed and does not change with the movement and the change on the reading of the laser sensors (r_i) (see Figure 43). Dead distance (d_i) includes; distance between p_i and the laser source and the distance between the reflective surface and p_o, measured in the direction of laser. The total length of the link l_i is the total distance between the spherical joint's pivot point p_i and the probe tip p_o. The length l must be corrected for the offset distance t' between the measuring axis and the pivot point as shown in Figure 43.
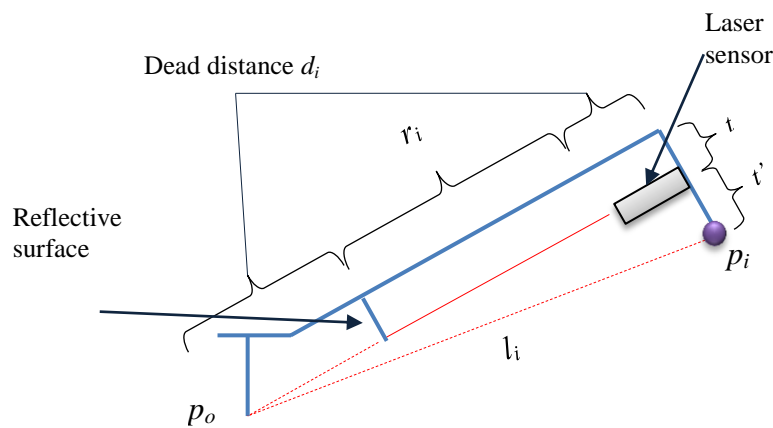
Figure 43: Dead distance on the links.

The length d_i can be found if the positions p_i and p_o are known; where p_i is calculated using reference point m_i (as shown in section 6.2.2), and p_o is measured using the master CMM by measuring the centre of the ball tip of the micro-CMM's probe, as shown in Figure 44. Then the inverse kinematics of the machine is solved to identify the length of the link l_i. The dead distance d_i can then be calculated.

For this step the length was calculated at 10 known positions and the IPKM was solved to determine d_i, see Figure 45, the detailed readings and the calculation can be viewed in Table C-1.
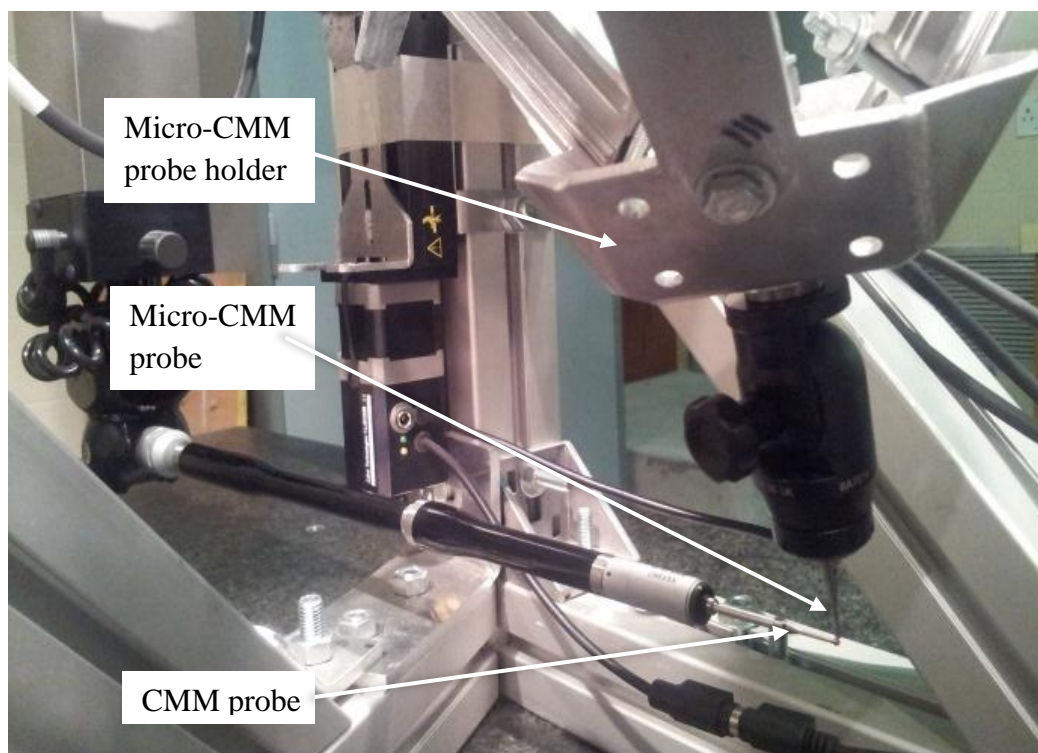
Figure 44: Photograph of measuring the probe tip position with a CMM.
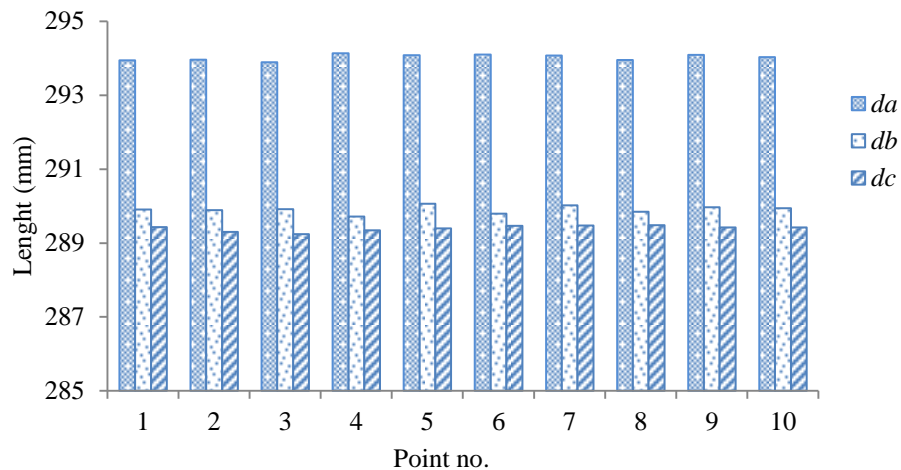
Figure 45: Results of dead distance calculation.

The average dead distance for the legs found to be: $d_a = 294.047$ mm, $d_b = 289.906$ mm and $d_c = 289.402$ mm, with the following standard deviations: $\sigma_a = 0.107$ mm, $\sigma_b = 0.126$ mm and $\sigma_c = 0.113$ mm, respectively.

6.2.5 Abbé error

The most important angular error affecting linear positioning accuracy is the result of Abbé error. The Abbé effect decreases as the offset distance between the axes of measurement and the probe tip decreases. Since the laser distance sensor is located in the axes of movement and pointing towards the probe tip, the resulting offset is virtually avoided.

Nevertheless, as shown in Figure 46, the arrangement may suffer from some offset created by the effect of imperfect alignment during the setup process. Suppose that the arrangement can produce an angle of $\alpha = 50$ arcseconds, and the offset of the laser distance sensor is not more than 0.2 mm. Then Abbé error can be approximated as:

$eab_i = offset$ x $tan(\alpha_i)$
$= 0.2$ mm x $tan(50$ arcseconds$) = 48$ nm

86
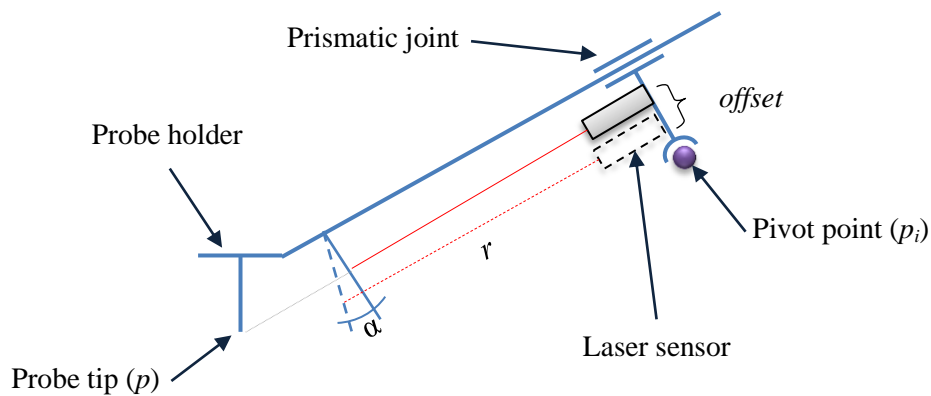
Figure 46: Abbé error due to offset in laser position.

6.2.6   Cosine error

Angular misalignment of the encoder and the object can produce cosine error. Cosine error is resulting from the fact that the laser may not be perfectly parallel to the leg of the tetrahedron it is trying to measure. Even though, in practice there will always be some degree of poor sensor alignment, the influence of cosine error can only be of significant value when a high degree of misalignment is present; therefore, cosine error in most cases can be neglected. Cosine error can be calculated as shown in Figure 47 by:

$$ecos = r\,(cos(\theta) - 1)$$

If the misalignment of the laser sensor with the probe tip at the maximum travel distance is as large as 0.1 mm, as shown in Figure 48. The angle of cosine error $\theta \cong 85$ arcsecond. Cosine error can be approximated at $r_{max} = 250$ mm as:

$$ecos = r\,(cos(\theta) - 1) \cong 20 \text{ nm}$$
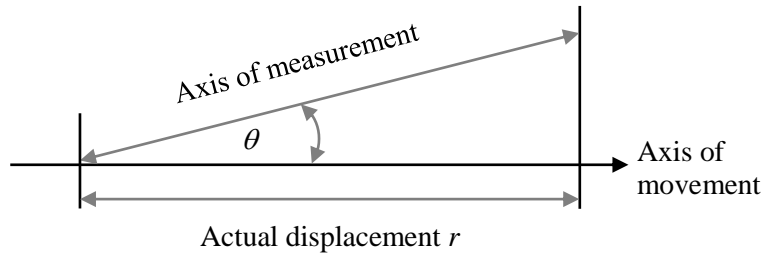
Figure 47: Cosine error illustrated.

Figure 48 shows the laser misalignment with the probe tip as the probe moves from minimum to maximum travel distance.
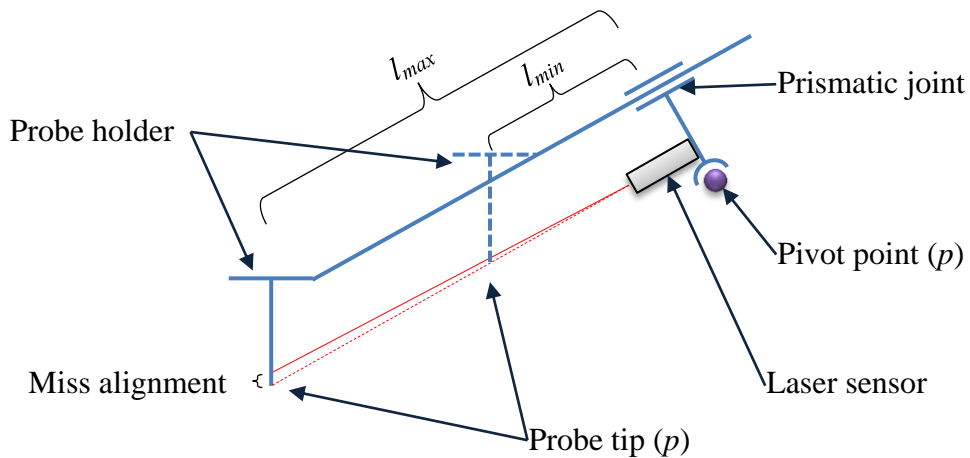
Figure 48: Cosine error due to laser misalignment.

6.2.7   Performance limitation

Table 5 lists the design values of the expected errors, which are claimed by the manufacturers of the state-of-the-art precision instruments available in the market,

and the actual values given by the manufacturers of the devices and hardware used to build the current prototype of the micro-CMM.

Table 5: Error sources on the micro-CMM

Error	Source	Affects	Design Values	Actual Values
es_i	machining limitation	x_i, y_i, z_i	1 µm	1.5 µm
eb_i	machining limitation	x_i, y_i	nano meter	40 µm
ed_i	manufacturing limitation	l_i	1 nm	150 µm
em_i	backlash	z_i	nano meter	1 µm
$ecos$	assembly	x, y, z	0	~20 nm
$eabbé$	design/assembly	x, y, z	angle 0.05 arcsec offset 10µm	~50 nm
ep	manufacturing limitation	x, y, z	0.08 µm	0.5 µm
$e\beta_i$	geometry	z_{in}, z_{ip}	0	70 µm

6.2.8   Motor displacement

The laser distance sensor is used to investigate the performance of the motors. The setup of the laser distance sensor and the motor is shown in Figure 49. The reflective surface is attached to the moving part of the motor and the sensor is fixed to the machine structure.

The movement range of the selected motors is 300 mm, with a mean backlash of 45 µm. Starting from zero position, a travel distance of 200 mm was completed four times with the following number of steps 50, 20, 8 and 4, which is equivalent to step sizes 5 mm, 10 mm, 25 mm and 50 mm, respectively. The laser distance sensor is used to capture the position on each step.
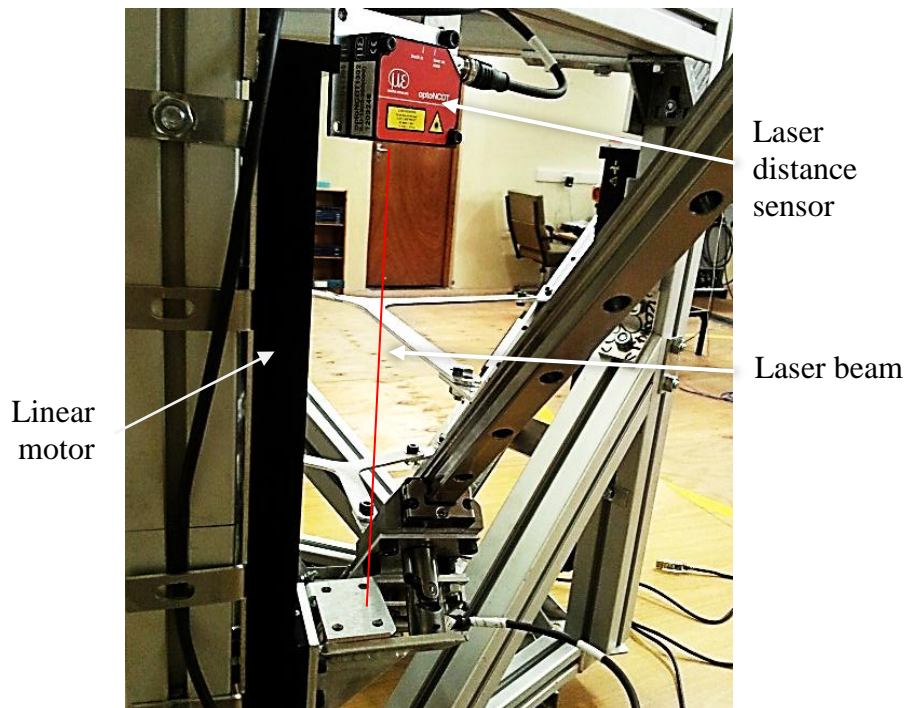
Figure 49: Motor characterization.

Figure 50 shows the differences between the motor commands and the readings of the laser sensor at 150 mm and 200 mm.
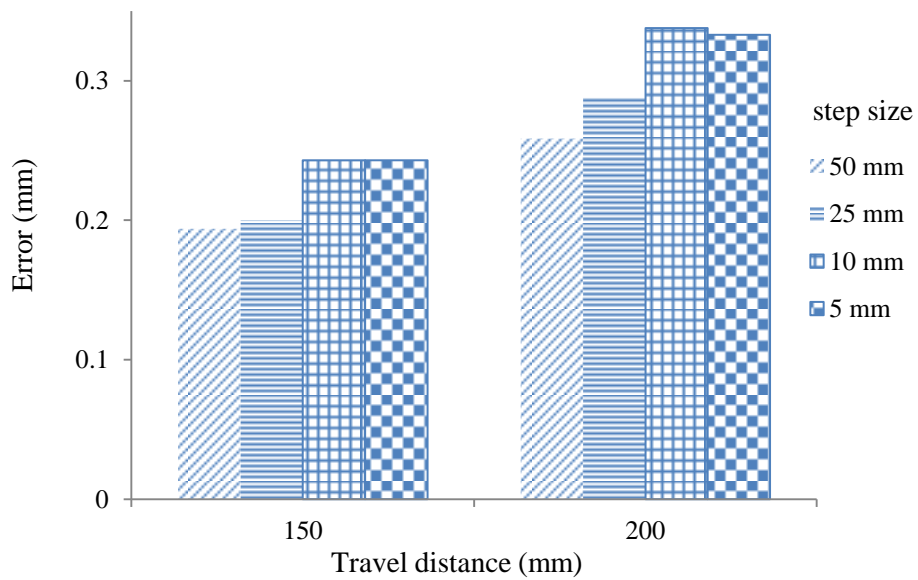
Figure 50: Motor test results.

90

Figure 50 shows that there is significant error associated with the motors. This error increases as the travel distance increases. It is also clear that larger step sizes result in less error as the number of required steps to reach the destination decrease. This result concludes that the motors cannot be used as a reliable displacement measurement of the travel distance.

It should be noted that the error associated with the motors does not affect the kinematic model of the machine, because the calculation of the position and travel distance does not depend on information from the motors. Position is corrected with every movement using the control algorithm (as shown in the movement control model in section 5.3.1).

CHAPTER 7:

Error modelling

7.1   Introduction

The micro-CMM is characterized to confirm the validity of the proposed kinematic model and the analytical error model. The measurements of the micro-CMM are compared to the measurements done with the master CMM. The analytical error model is used to confirm that the difference in measurements falls within the error budget estimated by the error model. Monte-Carlo simulation is also included in the comparison to confirm the validity of the results.

7.2 CMM measurements

The master CMM is used to determine the probe position of the micro-CMM. When the probe is stationary, measurements are taken at random positions. In each position the micro-CMM measurement is compared with the master CMM by measuring the micro-CMM's probe tip with the master CMM.

Total of 30 points were measured, the positions of these measured points in the *xy* plane are illustrated in Figure 51. A 3D view of the measured points is given in Figure 52.
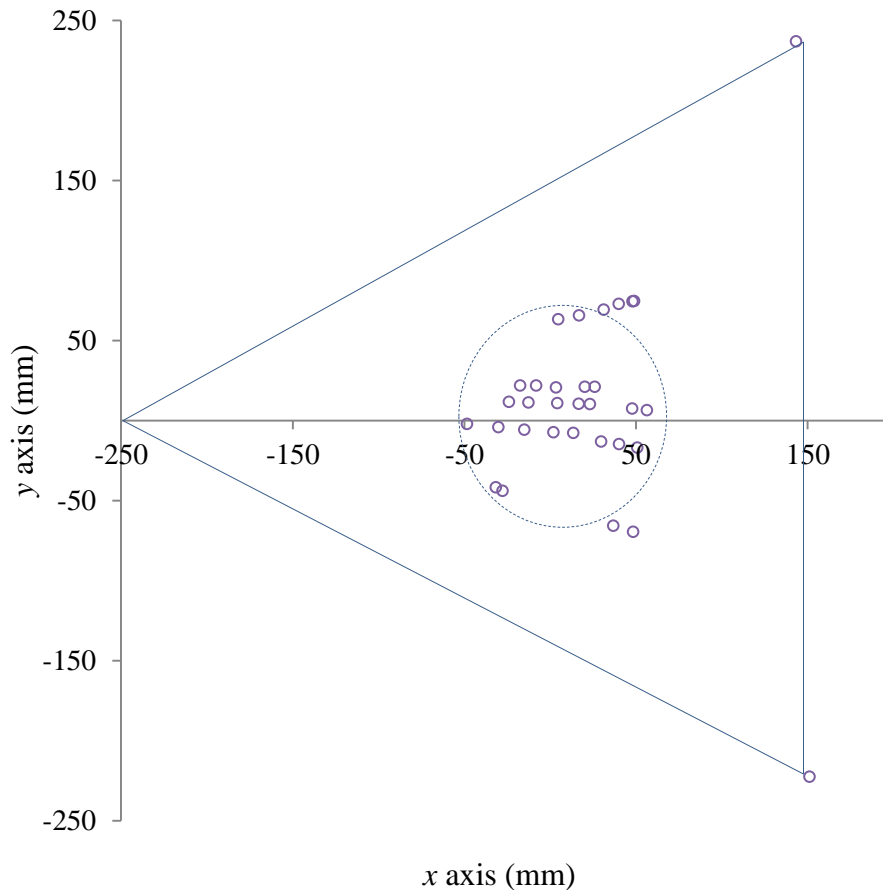
Figure 51: Measured points and the workspace of the micro-CMM.

93
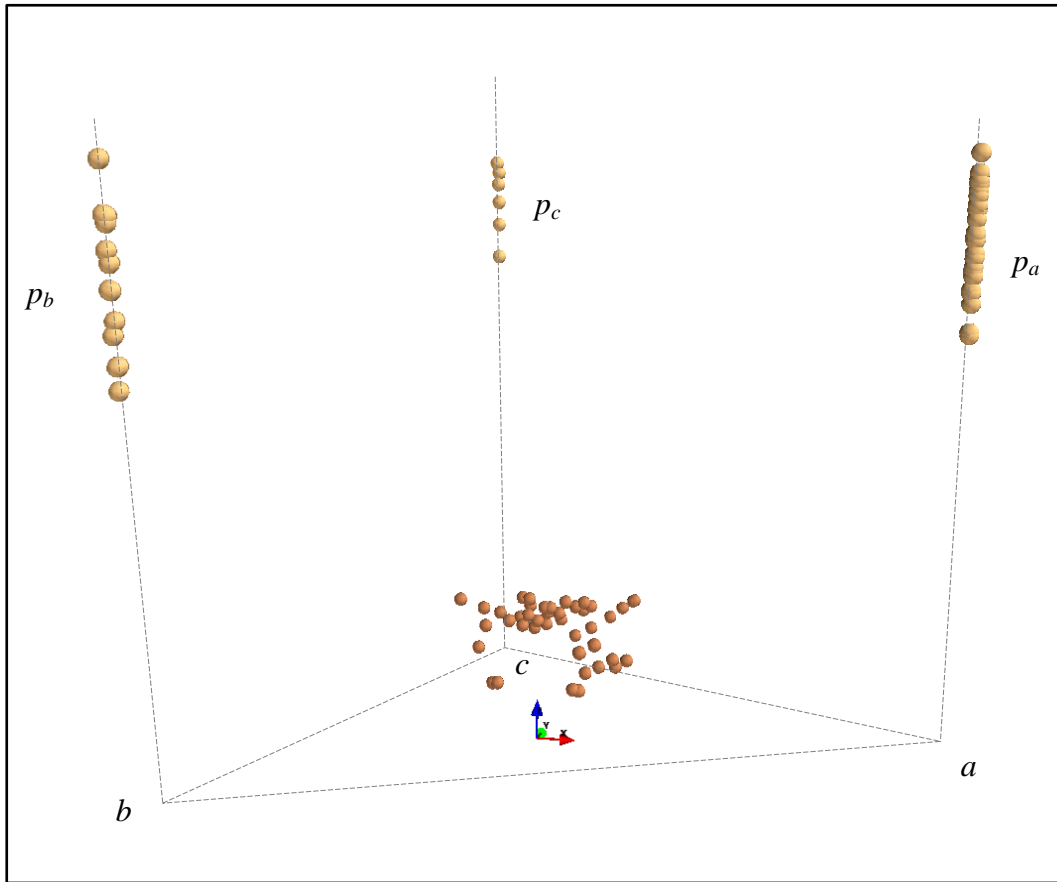
Figure 52: 3D plot of the micro-CMM measured points.

The measurements of the micro-CMM are compared to the measurements done with the master CMM. The difference between the two measurements are shown in Figure 53.
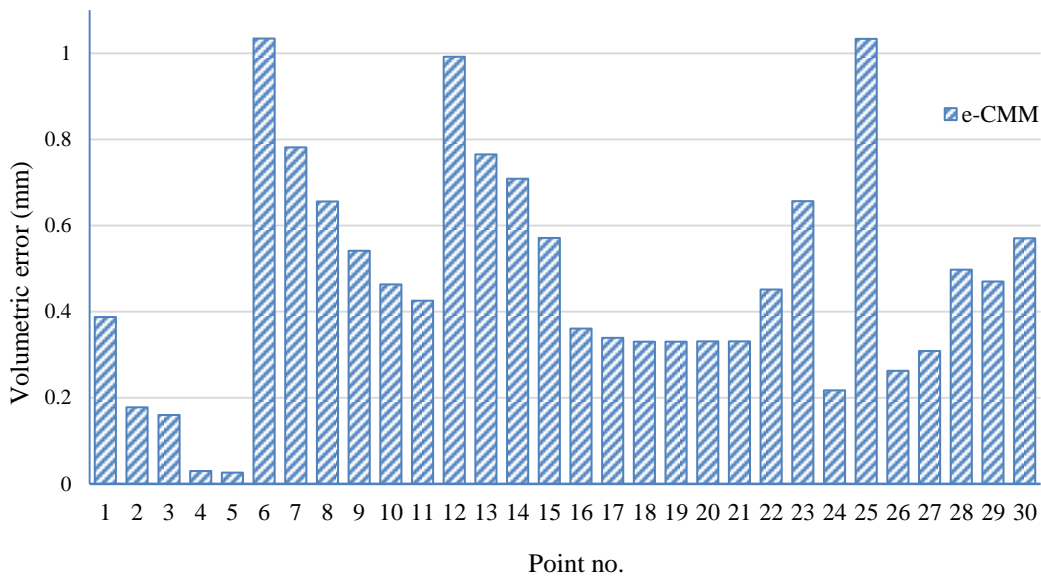
Figure 53: Volumetric error between micro-CMM and master CMM.

The detailed CMM readings can be viewed in Table C-2. From these results, it is clear that the difference in the vector length between the master CMM and the micro-CMM is mostly positive, where the readings from the micro-CMM are generally larger than the readings from the master CMM. This gives an indication that the error might by systematic. Using good calibration techniques effectively reduces this kind of errors.

7.3   Analytical modelling

The covariance matrix of measurement errors is found by the proposed analytical approach in equation (32). The variance-covariance matrix (equation 34) consists of the variances of x, y and z along the main diagonal and the covariances between each pair of variables in the other matrix positions. Variance is calculated using the relation given in equation (35).

Using the method described in section 4.5.1. The results of the error model for (0,0,0) position is the following variance-covariance matrix:

95

$$\Lambda_p = \begin{bmatrix} \sigma_x^2 & \sigma_x\sigma_y & \sigma_x\sigma_z \\ \sigma_y\sigma_x & \sigma_y^2 & \sigma_y\sigma_z \\ \sigma_z\sigma_x & \sigma_z\sigma_y & \sigma_z^2 \end{bmatrix} = \begin{bmatrix} 0.027 & -0.005 & -0.003 \\ -0.003 & 0.022 & -0.004 \\ -0.003 & -0.004 & 0.018 \end{bmatrix}$$

0.729 mm, y= 0.484, z= 0.324 The covariance between *xy*, *xz* and *yz* is very small and can be neglected, hence *x, y* and *z* can be assumed uncorrelated.

7.4   Monte-Carlo

In Monte-Carlo studies, random parameter values are generated from an allowed error range. A large number of runs ($n = 20,000$) are carried out, and the model is estimated in each run. Parameter values and standard errors are averaged over the whole samples. As shown in section 4.5.2, equations (37), (38) and (39) are used to estimate the error model at different positions within the work envelope. The simulation produce results in the form of standard deviation.

The process parameters used for the error modelling and their corresponding error budget values are tabulated in Table 6.

Table 6: Error budget used for the error modelling

Parameters	Error budget
x_i	$\pm$ 50 µm
y_i	$\pm$ 50 µm
z_i	$\pm$ 250 µm
r_i	$\pm$ 50 µm
d_i	$\pm$ 110 µm
α_i	$\pm$ 0.02°
β_i	$\pm$ 0.05°
θ_i	$\pm$ 0.02°
$offset_i$,	200 µm

Error in the links include the accuracy of the laser sensors, uncertainty of the dead distance calculation, cosine error and the effect of Abbé error (*dl = er, ed, eab, ecos*).

The error results from calculating the position of the pivot points (*z* components) is influenced by the error in the links, as well as the rigidity of the moving part (tetrahedron), where the legs are only connected at the probe holder, therefore, the angle *β* between the legs is subject to the mechanical deformation.

The results of the Monte-Carlo simulation are represented in the form of a typical histogram in Figure 54, 54 and 55 for *x, y* and *z*, respectively, at zero position (0,0,0). The histograms are useful as an aid to understanding the nature of the data distribution.
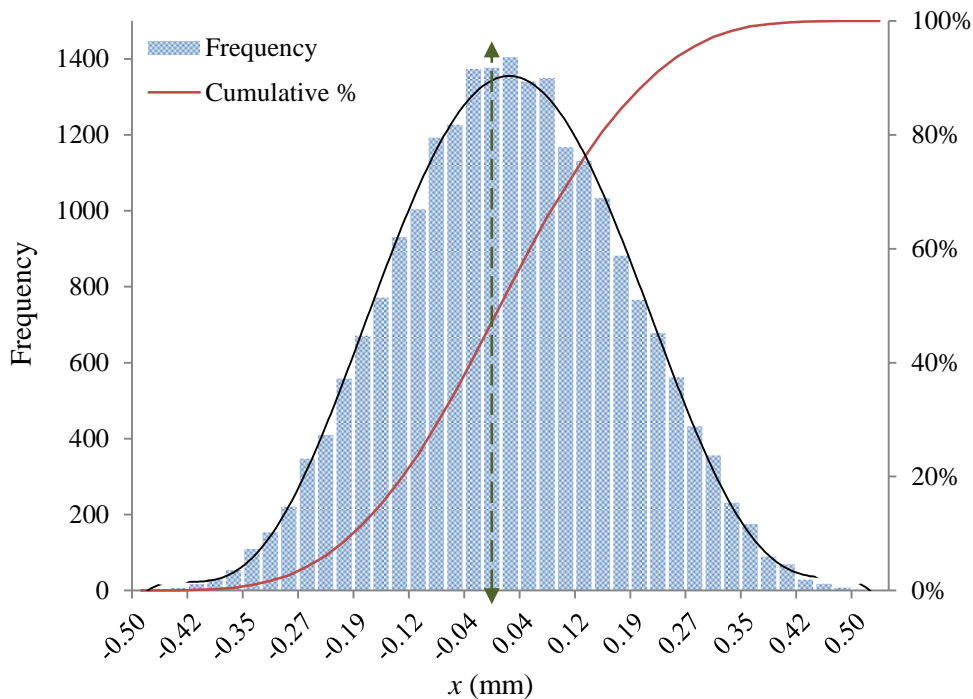
Figure 54: Histogram of error in *x*, results of Monte-Carlo simulation.
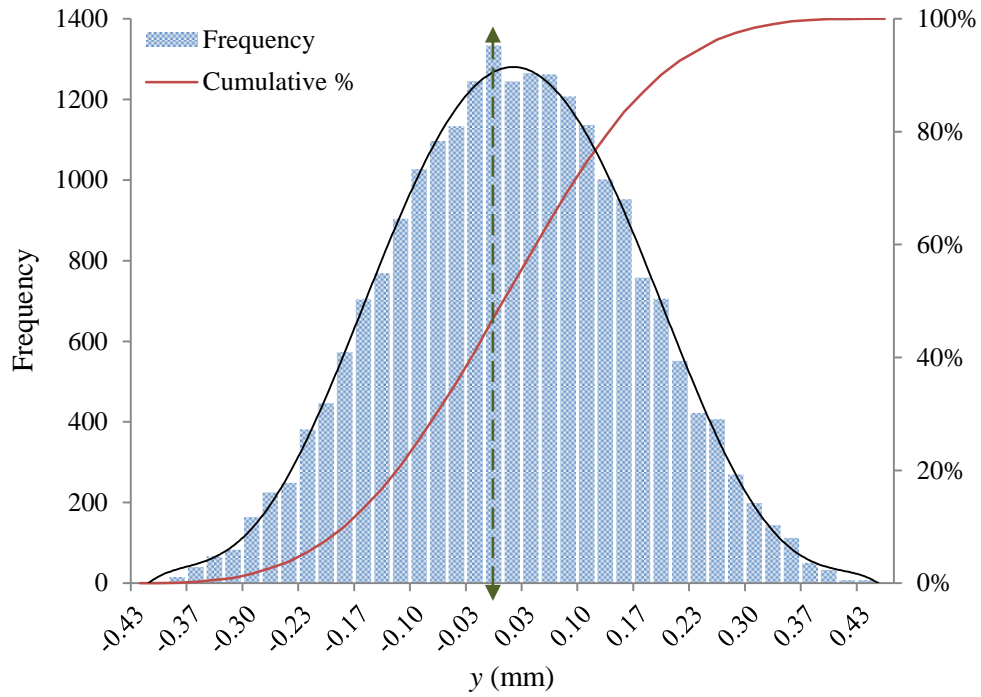
Figure 55: Histogram of error in *y*, results of Monte-Carlo simulation.
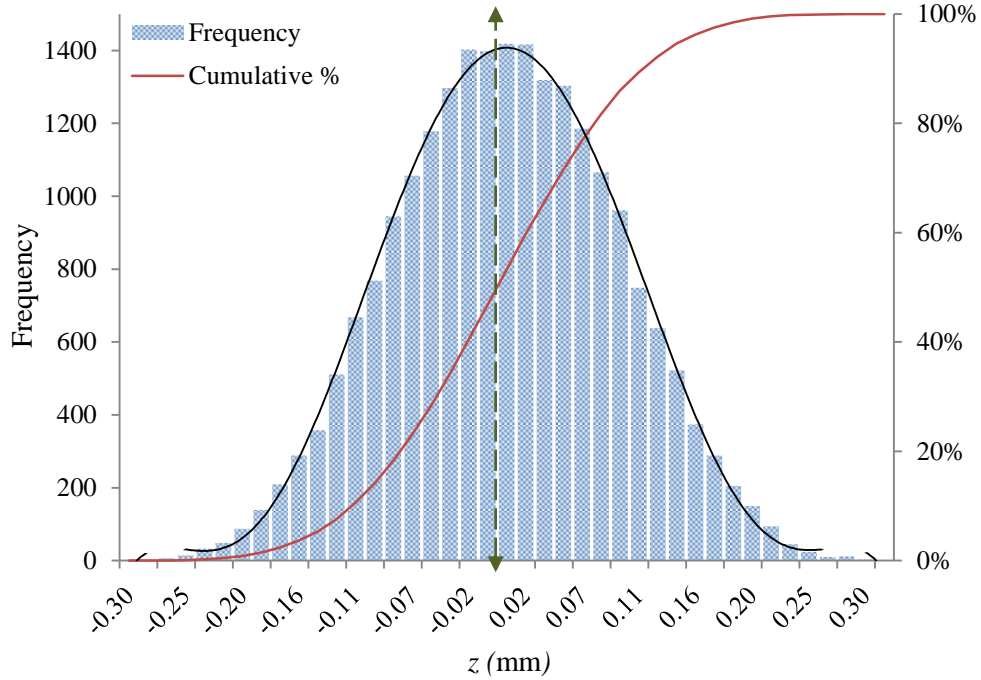
Figure 56: Histogram of error in *z*, results of Monte-Carlo simulation.

From the previous figures, histogram plots for *x, y* and *z* indicate that the data are approximated well by a normal distribution, therefore it is reasonable to use the standard deviation as the distribution estimator.

7.5   Verification of error model

Comparisons of a sample calculation of simulated results with the analytical results in terms of standard deviations (σ) are given in Figure 57. The results of the analytical error model (AM) match very well with the simulation results (MC). The standard deviation results of AM and MC follows the same trend as shown in the figure.
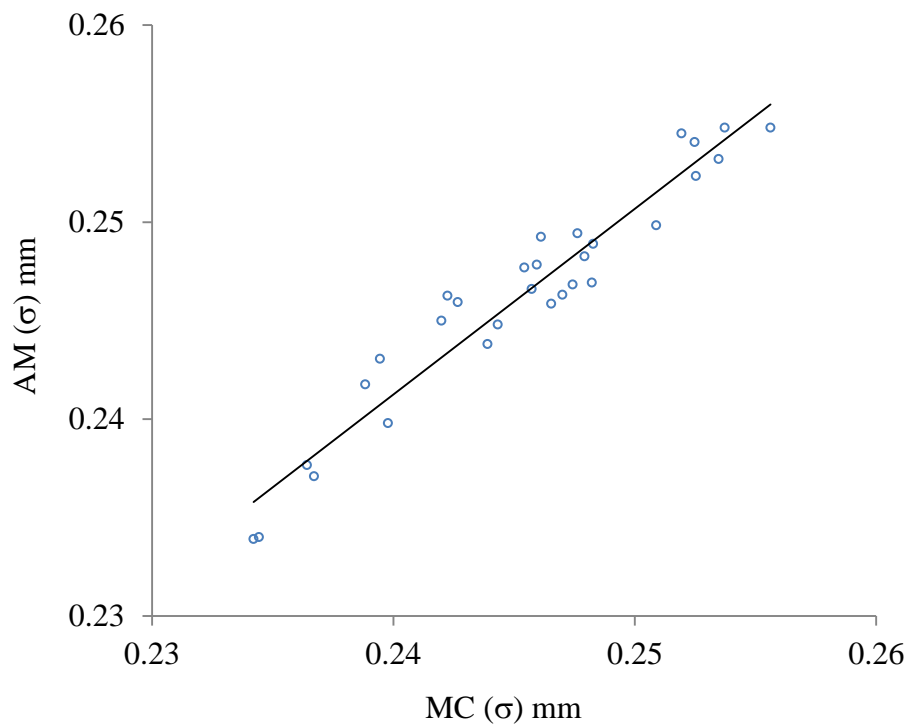
Figure 57: Error model results, analytical (AM) versus simulation (MC).

7.6   Results of the error model

A comparison of the expected error budget of the micro-CMM reading, estimated by; difference between actual CMM measurements, Monte-Carlo simulation (MC) and analytical error model (AM), respectively in 30 different positions is given by Figure 58.

The error comparison is given by three bars for each point. Hatched bars represent the error values between the micro-CMM readings and the master CMM, solid bars represent the estimated error using AM, and the unfilled bars represent the expected error using MC simulation. In the figure all the results are presented as a volumetric error value, estimated as 3σ by MC, and $3\left(\sqrt{\sigma^2}\right)$ by AM. These results can be viewed in more details in Table C-3.
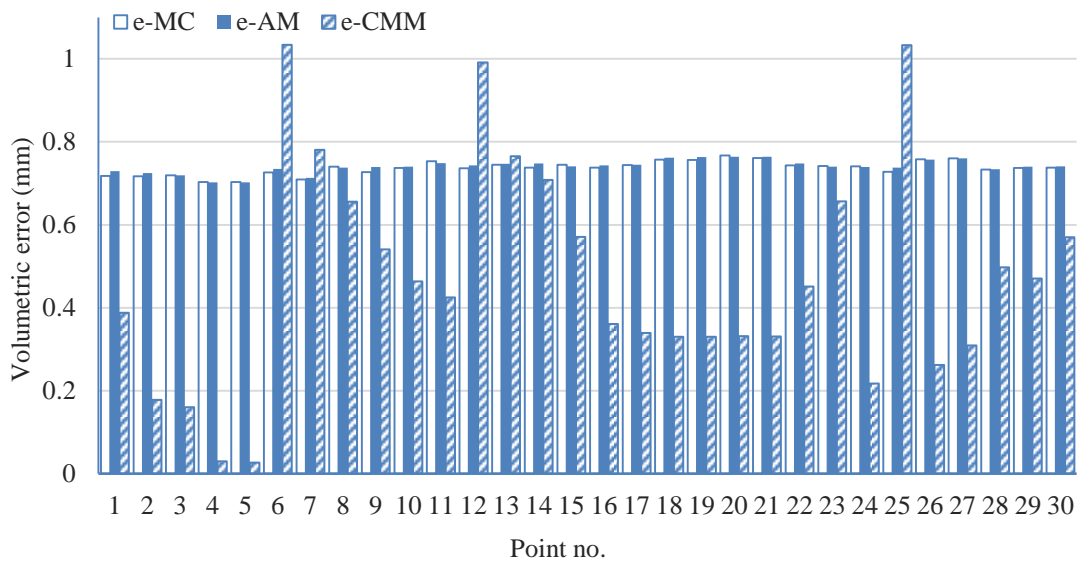
Figure 58: Error estimation, e-CMM vs AM vs MC.

From Figure 58, it is clear that for most of the measured points the error falls within an acceptable range of the error budget estimated by the simulation and analytically. Even though the graph shows some points that have outliers such as

on points number 6, 12 and 25, these errors can be attributed to the effect of a lot of external factors, such as human error in taking measurements or mechanical vibration.

7.7   Parameter contribution to the error

The significance of the errors associated with the geometric parameters on the positioning accuracy of the probe was studied. The error model is used to investigate the individual contribution of each parameter to the total estimation of the machine error. The results of the investigation are shown in Figure 59.
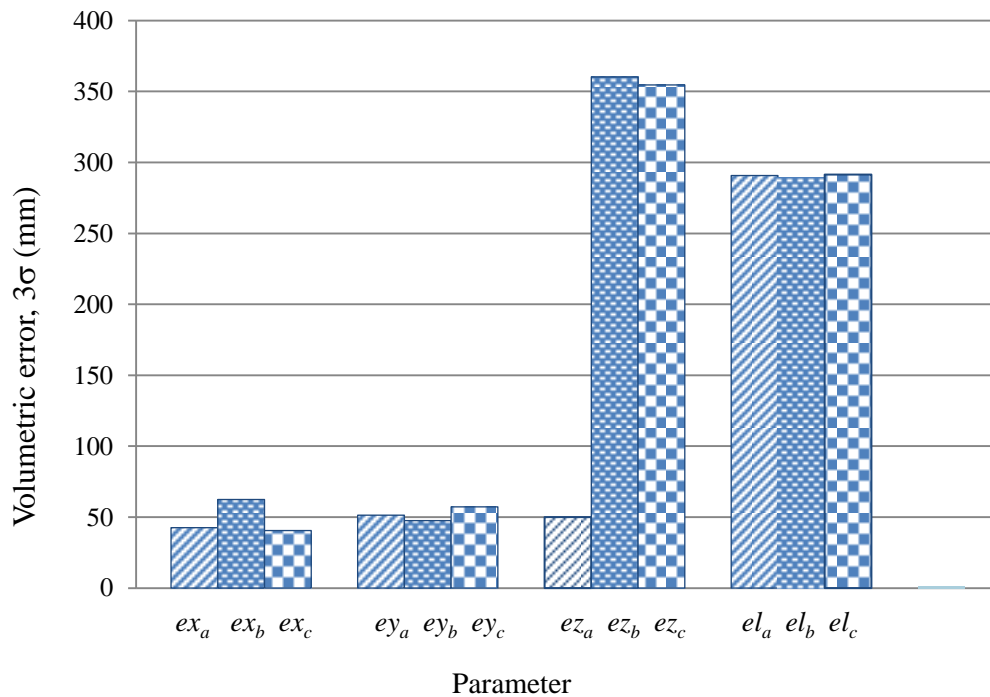
Figure 59: Parameters contribution to the total error.

From the above figure, it is clear that z and l are responsible for the major contributions that significantly affect the machine accuracy. The position of the pivot points in the vertical direction (z component) is responsible for the most

significant contribution to the overall machine error, followed by the uncertainty in determining the lengths of the links.

ex and *ey* includes the *x* and *y* components of the run out error in the joints, parallelism in the slides and error in the motors. *ez* is due to run out in joints, backlash in motors, deflection and elastic deformation of the moving tetrahedron, and error in measuring the length of the links. *el* is affected by Abbé effect, cosine error and uncertainty in the laser reading.

The error in z_i is cumulative. That is because every time the probe is moved to a new position one motor stays stationary and the positions of the other two motors are calculated relative to the stationary motor, as explained in Chapter 4. The accuracy of these calculations can be improved by improving the rigidity of the moving tetrahedron and the uncertainty of angle between the moving legs.

The second main error source "l_i" is solely due to the limitation of the measuring device "laser distance sensor". This error can be reduced if the angular errors can be avoided and a laser interferometer with resolution in the nano meter range is used.

7.8   Recommended configuration of the micro-CMM

Previous results show that the proposed analytical error model is valid and can be used as a robust tool for an error estimation model for the micro-CMM under study. The same error model is still valid to estimate the error values for the machine. The best possible configuration of the micro-CMM can be achieved as per the information provided for the design values in Table 7, with the following recommendations:

- Improving the rigidity of the structure to reduce the dynamic errors resulting from the effect of vibration and the weight of the moving parts,

- Adding triple beam laser interferometer to replace the existing optoNCDT 1302 laser distance sensor from micro-epsilon, virtual elimination of Abbé error is achieved by using a triple beam laser interferometer, which is capable to measures pitch and yaw angles with 0.02 arcsecond angular resolution.

- Moreover, reducing the legs' length and mounting the encoder at minimum possible dimensional offset between the probe tip and the measuring axes would be effective.

- Using of super precision class spherical rolling joints run-out less than 0.1 micron compared to the existing 2 micron for the standard precision class SRJ joints. Moreover the other suggestion is the use of capacitive sensors to measure the run out error in the spherical joints.

- Runner blocks can be replaced by sliding contact bearings to achieve nano meter accuracy as proposed by Smith and Robbie [106].

- The probe is a critical factor in the measurement limitation. Improving the probe capability results in improving the overall accuracy of the machine.

- Moreover, operating in a temperature controlled environment minimizes the thermal effect.

A comparison is shown in Table 7. The table lists the parameters used in error modelling of the current prototype and the recommended improvements to achieve the goal of submicron measurements.

The results of the kinematic error model are used as a comparison between the two different combinations, the results are tabulated in Table 8.

Table 7: Error budget of the parameters of the micro-CMM

Parameters	Current prototype	Design values
x_i	$\pm$ 50 μm	$\pm$ 0.1 μm
y_i	$\pm$ 50 μm	$\pm$ 0.1 μm
z_i	$\pm$ 250 μm	$\pm$ 0.1 μm
r_i	$\pm$ 50 μm	$\pm$ 0.02 μm
d_i	$\pm$ 110 μm	$\pm$ 0.01 μm
α_i	$\pm$ 0.02^o	$\pm$ 0.005^o
β_i	$\pm$ 0.05^o	$\pm$ 0.005^o
θ_i	$\pm$ 0.02^o	$\pm$ 0.005^o
offset	200 μm	0.5 μm

Table 8 lists a comparison of the error model determined by the proposed analytical error model for the two different configurations.

Table 8: Error model results and comparison

	AM (σ) μm			$\sigma_{volumetric}$ μm	$e_{volumetric}$ μm
	x	y	z		
Current prototype	163.136	148.56	90.779	238.588	715.764
Recommended configuration	0.069	0.062	0.039	0.101	0.302

The results of the error modelling listed in Table 8 show that with the recommended combination proposed in Table 7, the micro-CMM can achieve measurements in submicron regime with standard deviation of not exceeding 70 nm in each direction (x = 70 nm, y = 60 nm, z = 40 nm).

CHAPTER 8:

Comparison with an alternative design

8.1   Introduction

The novel micro-CMM was eventually designed and built based on the problems identified with a preliminary micro-CMM prototype. This chapter represent the design, kinematics and modelling of the initial prototype; this work can be viewed in reference [107]. A comparison between the initial micro-CMM prototype and the final novel micro-CMM under study is given at the end of this chapter.

8.2   Design description

The initial micro-CMM prototype designed in this research consists of an upper equilateral triangular frame and a lower equilateral triangular moving platform connected to the upper frame with three extendable legs. Each leg contains a prismatic joint, the upper/lower ends of the legs are connected to the frame/platform (at points f_i / p_i) with spherical joints. Moreover, laser interferometers are installed on the legs in order to acquire accurate measurement of the length of the legs. To separate the measurement and movement loops and to overcome the kinematic modelling complexity, the lower platform can only move with respect to the upper frame. The movement of the platform is controlled by three linear motors attached to the upper frame. An isometric view and a top view of the machine are shown in Figure 60.
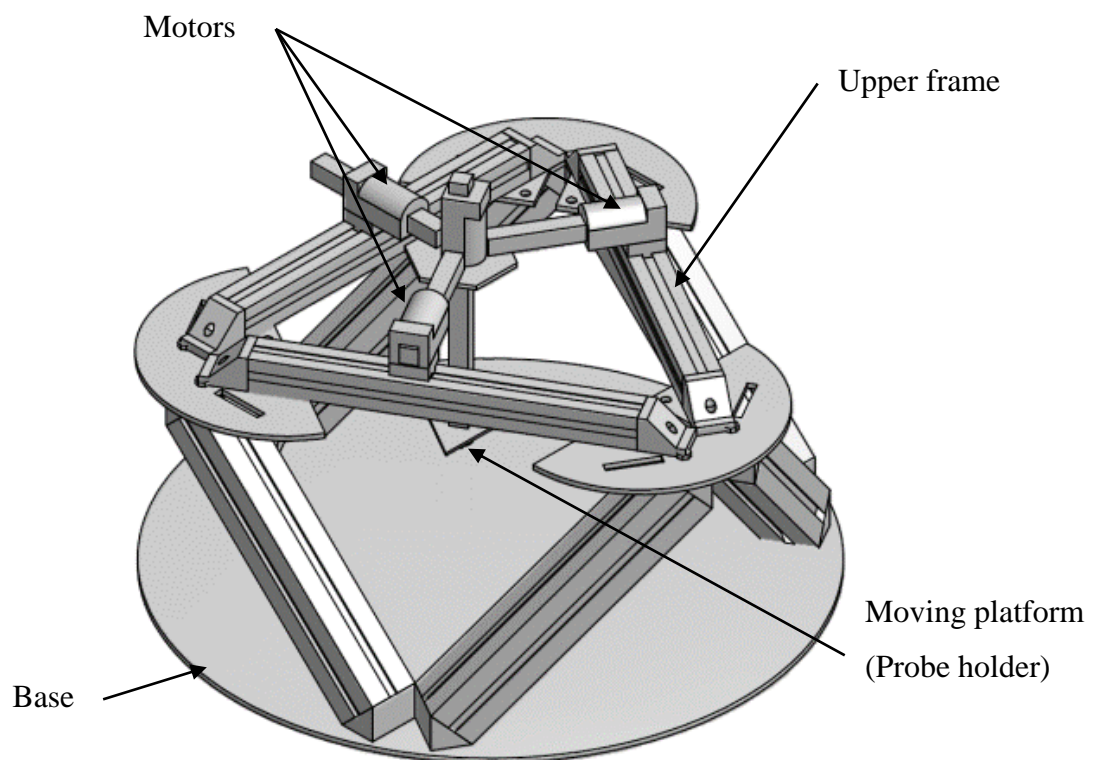
Figure 60-a: Isometric drawing of the initial micro-CMM design.
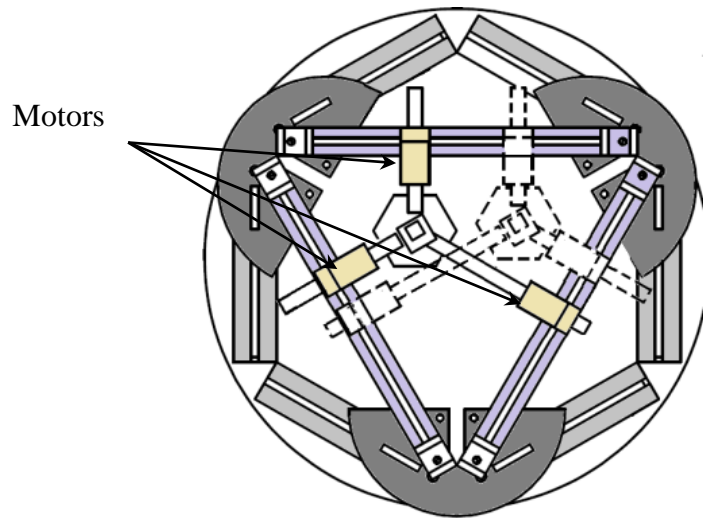
Figure 60-b: Top view of the initial micro-CMM design.

In this arrangement spherical joints are used to connect the three extendable legs to the moving platform and the upper frame were used. The spherical joints represent three rotational degrees of freedom (3-DOF). However, the movement of the platform is restricted to always be parallel to the upper frame. The sacrifice of the rotational movement of the moving platform around the axes is beneficial for solving the kinematics model. Figure 61 shows a schematic drawing of this design.
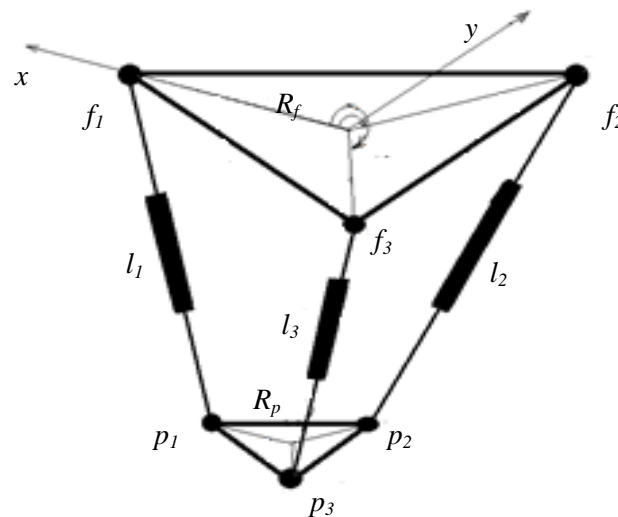
Figure 61: Schematic drawing of the micro-CMM machine.

8.3   Coordinate system

The coordinate system is shown in Figure 62. The origin O_f-(0,0,0) is placed at the centre of the upper frame. The x-axis equally divides the angle at point f_1 and the z-axis is perpendicular to the frame plane.
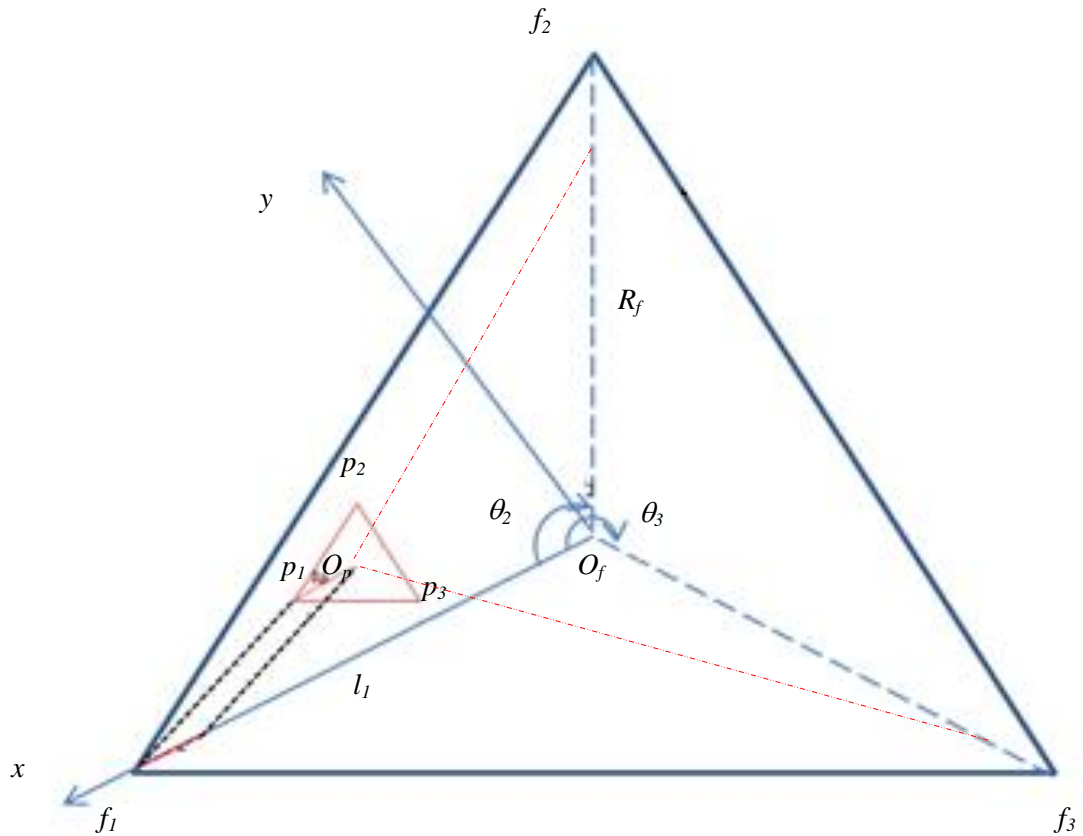
Figure 62: The coordinate system.

The geometrical parameters are as follows:

R_f : the distance between point f_i and the origin O_f

R_p : the distance between point p_i and the origin O_p

θ_i : the angle point f_i makes with the x-axis, $\theta_1 = 0^o$, $\theta_2 = 120^o$, $\theta_3 = 240^o$

l_{min}, l_{max} : the maximum and minimum extensions of the legs.

8.4   Kinematics modelling

Because of using spherical joints, the movement of the legs can be expressed by the equation of a sphere. Assuming that the central point of the moving platform (x,y,z) is the point of intersection of three spheres, and thus, point f_i must be shifted towards the point of origin O_f. by $(f_i - p_i)$ where:

$$p_i = [\; R_p \; \cos \theta_i \quad R_p \sin \theta_i \quad z]^T \tag{40}$$

$$f_i = [\; R_f \; \cos \theta_i \quad R_f \sin \theta_i \quad 0]^T \tag{41}$$

Then the equation of movement of the legs can be written as follows:

$$l_1^2 = \left[x - \left(R_f - R_p\right)\cos \theta_1\right]^2 + \left[y - \left(R_f - R_p\right)\sin \theta_1\right]^2 + [z]^2 \tag{42}$$

$$l_2^2 = \left[x - \left(R_f - R_p\right)\cos \theta_2\right]^2 + \left[y - \left(R_f - R_p\right)\sin \theta_2\right]^2 + [z]^2 \tag{43}$$

$$l_3^2 = \left[x - \left(R_f - R_p\right)\cos \theta_3\right]^2 + \left[y - \left(R_f - R_p\right)\sin \theta_3\right]^2 + [z]^2 \tag{44}$$

Where:

(x,y,z): the probe location

l_1, l_2 and l_3: the leg lengths.

The probe location can be found by solving equations (42), (43) and (44). This yields explicit expressions for the x, y and z coordinates of the centre point.

$$x = \frac{2l_1^2 + l_2^2 + l_3^2}{4\left(R_f - R_p\right)(\cos \theta_1 - \cos \theta_2)} - \frac{\left(R_f - R_p\right)\left(\cos \theta_2{}^2 - 1\right)}{2(\cos \theta_1 - \cos \theta_2)} \tag{45}$$

$$y = \frac{l_2^2 - l_3^2}{2\left(R_f - R_p\right)(\sin \theta_2 - \sin \theta_3)} - \frac{\left(R_f - R_p\right)\left(\sin \theta_2{}^2 - \sin \theta_3{}^2\right)}{2(\sin \theta_2 - \sin \theta_3)} \tag{46}$$

109

$$z = \sqrt{l_2^2 - \left[X + \left(R_f - R_p\right)\cos\theta_2\right]^2 - \left[Y + \left(R_f - R_p\right)\sin\theta_2\right]^2} \tag{47}$$

The previous equations are used to calculate the pose of the probe, given the values for the mechanism parameters. These equations represent the direct position kinematic model (DPKM) of the system.

8.5   Error model

Similar to the derivations given in Chapter 4, the law of error propagation is used to determine the machine's associated error analytically; the covariance matrix is given by equation (20).

Assuming that only mechanical errors among these errors have an influence on the positioning accuracy, the geometry of each stage (or leg) can be expressed by five geometrical parameters, which are the leg lengths l_i and the position of each spherical joint f_i and p_i in the Cartesian coordinate system. Therefore in total 15 parameters will be investigated. Thus, equations (45), (46), and (47) must be rewritten as:

$$x = \frac{(l_2^2 - l_3^2) - (x_2^2 - x_3^2) - (y_2^2 - y_3^2)}{2(x_3 - x_2)} - Y\frac{(y_3 - y_2)}{(x_3 - x_2)} \tag{48}$$

$$y = \frac{(l_1^2 - l_2^2) - (x_1^2 - x_2^2) - (y_1^2 - y_2^2) - \frac{(x_2 - x_1)}{(x_3 - x_2)}\left[(l_2^2 - l_3^2) + (x_3^2 - x_2^2) - (y_3^2 - y_2^2)\right]}{2\left[(y_1 - y_2) - \frac{(x_2 - x_1)}{(x_3 - x_2)}(y_3 - y_2)\right]} \tag{49}$$

$$z = \sqrt{l_2^2 - (X - x_2)^2 - (Y - y_2)^2} \tag{50}$$

where:

$$x_i = R_{fi}\cos\left(\theta_{fi}\right) - R_{pi}\cos\left(\theta_{pi}\right); \qquad y_i = R_{fi}\sin\left(\theta_{fi}\right) - R_{pi}\sin\left(\theta_{pi}\right); \qquad i = 1,2,3$$

A full size Jacobian matrix is used in carrying out error analysis, the Jacobian needed will be a 3×15 matrix as follows:

$$J = \begin{bmatrix} \frac{\partial x}{\partial l_1} & \frac{\partial x}{\partial l_2} & \frac{\partial x}{\partial l_3} & \frac{\partial x}{\partial R_{p1}} & \frac{\partial x}{\partial R_{p2}} & \frac{\partial x}{\partial R_{p3}} & \frac{\partial x}{\partial R_{f1}} & \frac{\partial x}{\partial R_{f2}} & \frac{\partial x}{\partial R_{f3}} & \frac{\partial x}{\partial \theta_{p1}} & \frac{\partial x}{\partial \theta_{p2}} & \frac{\partial x}{\partial \theta_{p3}} & \frac{\partial x}{\partial \theta_{f1}} & \frac{\partial x}{\partial \theta_{f2}} & \frac{\partial x}{\partial \theta_{f3}} \\ \frac{\partial y}{\partial l_1} & \frac{\partial y}{\partial l_2} & \frac{\partial y}{\partial l_3} & \frac{\partial y}{\partial R_{p1}} & \frac{\partial y}{\partial R_{p2}} & \frac{\partial y}{\partial R_{p3}} & \frac{\partial y}{\partial R_{f1}} & \frac{\partial y}{\partial R_{f2}} & \frac{\partial y}{\partial R_{f3}} & \frac{\partial y}{\partial \theta_{p1}} & \frac{\partial y}{\partial \theta_{p2}} & \frac{\partial y}{\partial \theta_{p3}} & \frac{\partial y}{\partial \theta_{f1}} & \frac{\partial y}{\partial \theta_{f2}} & \frac{\partial y}{\partial \theta_{f3}} \\ \frac{\partial z}{\partial l_1} & \frac{\partial z}{\partial l_2} & \frac{\partial z}{\partial l_3} & \frac{\partial z}{\partial R_{p1}} & \frac{\partial z}{\partial R_{p2}} & \frac{\partial z}{\partial R_{p3}} & \frac{\partial z}{\partial R_{f1}} & \frac{\partial z}{\partial R_{f2}} & \frac{\partial z}{\partial R_{f3}} & \frac{\partial z}{\partial \theta_{p1}} & \frac{\partial z}{\partial \theta_{p2}} & \frac{\partial z}{\partial \theta_{p3}} & \frac{\partial z}{\partial \theta_{f1}} & \frac{\partial z}{\partial \theta_{f2}} & \frac{\partial z}{\partial \theta_{f3}} \end{bmatrix} \tag{51}$$

The related variances matrix is given by the following 15×15 diagonal matrix:

$$\Lambda_p = \begin{bmatrix} \sigma_{l_1}^2 & 0 & \cdots & 0 \\ 0 & \sigma_{l_2}^2 & & \\ \vdots & & \ddots & \\ 0 & 0 & \cdots & \sigma_{\theta_{f3}}^2 \end{bmatrix} \tag{52}$$

In the previous matrix the variance along the diagonal is given for l_1, l_2, l_3, R_{p1}, R_{p2}, R_{p3}, R_{f1}, R_{f2}, R_{f3}, θ_{p1}, θ_{p2}, θ_{p3}, θ_{f1}, θ_{f2}, θ_{f3}. Precision error values are mostly considered as three times the standard deviation value ($\varepsilon = 3\sigma$). Thus, the variance can be estimated by:

$$\sigma_p{}^2 = \left(\frac{\varepsilon_p}{3} \right)^2 \tag{53}$$

Where: $\sigma_p{}^2$ and ε_p are the variance and the error of the parameters, respectively.

8.6   Mechanical errors estimation

This arrangement suffers from large angular error. The effect of Abbé error cannot be avoided. The offset distance between the axis of measurement and the probe tip changes with the movement of the probe, it may reach upto ±8.6 mm see Figure 63. This amount of offset in 3D results on significant Abbé error. Even

with very good alignment, an angle of only 0.005° results in Abbé error of ± 0.75 µm.
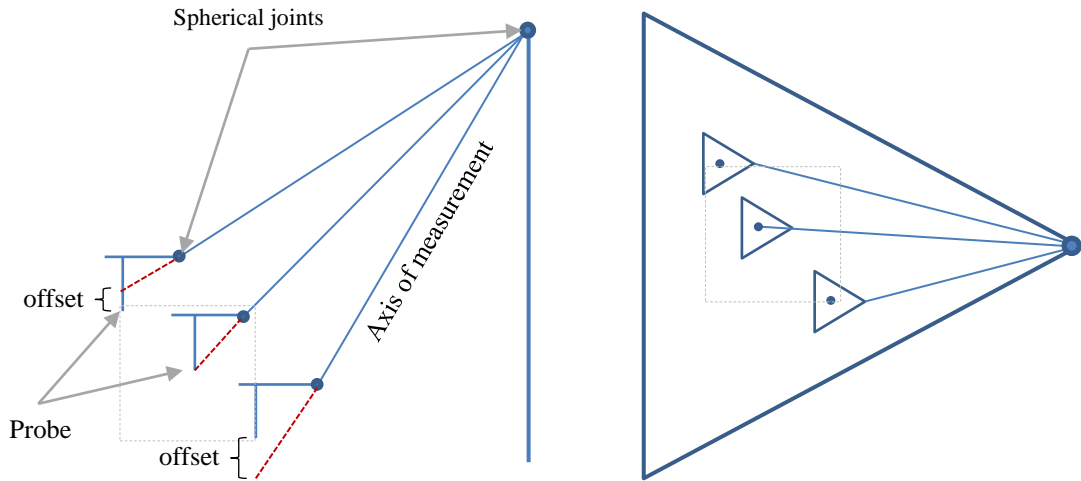
Figure 63: Abbé effect in 3D.

When the state-of-the-art instruments and components are to be used, the following values of the mechanical errors assigned to the system parameters and used in the kinematic error model estimation: $\varepsilon R_{fi} = \pm 0.1$ µm, $\varepsilon R_{pi} = \pm 0.1$ µm, $\varepsilon l_i = \pm 1$ µm, $\varepsilon \theta_{fi} = \pm 0.005^{\circ}$ and $\varepsilon \theta_{pi} = \pm 0.005^{\circ}$

The result of the kinematic error model shows that the best readings this arrangement can achieve is not in the submicron regime, with volumetric standard deviation of ($\sigma_{volumetic} = 1.2$ µm).

Figure 64 shows the σ_x, σ_y, and σ_z estimated using the analytical model. The three continuous lines represent σ_x, σ_y and σ_z with an error of $\varepsilon l_i = \pm 1$µm, the dashed line represents σ_z when the total error in the legs is ± 2 µm.
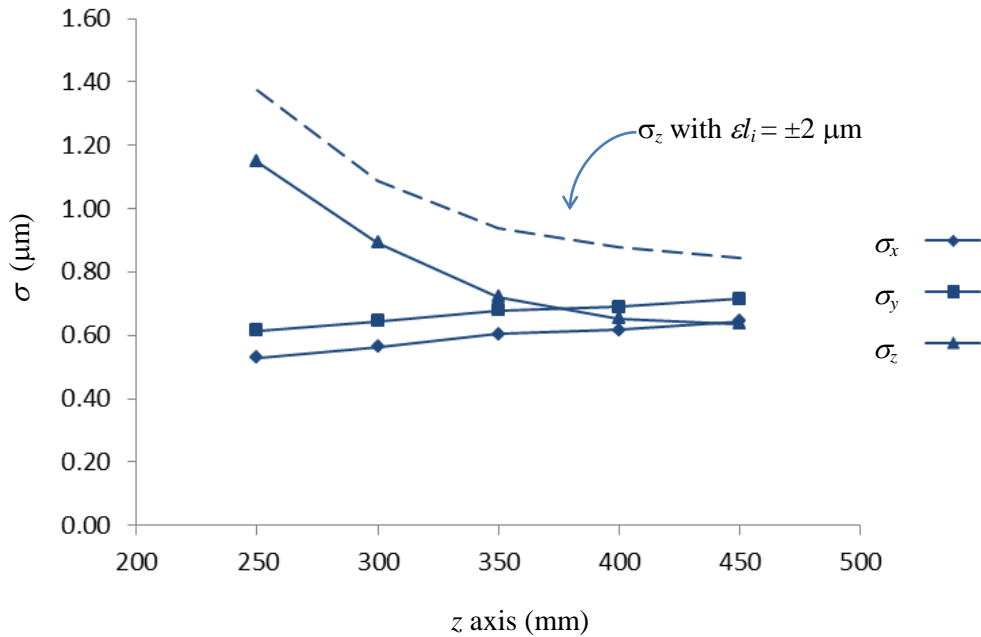
Figure 64: Error estimation along z axis.

From Figure 64, σ_z decreases dramatically as the moving platform translates away from the point of origin in the z direction, the σ_z starts to decrease very slowly when z value is greater than 350 mm, in other words, the probe is 350 mm below the upper frame. The work envelope in the z direction is in the range (350 – 450).

8.7   Comparison with micro-CMM

The results of the error model show that submicron measurements are difficult to achieve even when the best available instruments and components are considered, concluding that the initial prototype is not really a micro measurement machine. The major drawbacks of the initial prototype can be attributed to the following issues:

- The initial design suffers from significant Abbé effect, where all the sensors are not pointing towards the probe tip. This creates an offset distance between

113

the measuring axes and the object to be measured, this offset changes with the movement of the platform and position of the probe. This problem was solved by introducing the final design concept of the micro-CMM.

- The number of joints and connections are relatively high compared to the final design. Having three joints in each link, two of them are spherical joints, results in aggregating the run out error of determining the pivot points of each joint. The links in the final design only include one spherical joint.

- In practice, it is difficult to ensure that the moving platform is moving in a plane parallel to the base, this is due to the effect of elastic deformation, parallelism and backlash in the motors.

CHAPTER 9:

Conclusions and recommendations

9.1   Conclusions

The scope of this dissertation focuses on the growing need of highly accurate and precise measuring machines, specifically the use of PKM in micrometrology. PKMs are known to have useful advantages over their serial counterpart CMMs, these advantages include; high stiffness, high accuracy, and low inertia. Unfortunately, there are some disadvantages of using PKMs. The author proposes answers to some of these questions such as solving the complex kinematics, overcoming the workspace limitation, avoiding singularity and eliminating the effects of Abbé error.

Different types of errors which significantly affect the machine accuracy are given. Static errors are claimed to have the most significant effect. Nevertheless, dynamic errors must be considered for precise measurements. The static errors are caused by manufacturing and assembly errors, non-exact transformation and by the deformations of the machine structure through weight forces. Dynamic errors were not considered; they occur only during the operation and depend on the velocity, the acceleration and the forces.

A novel micro-measurement machine is introduced for the measurement of part dimensions in micro scale. The design of the novel machine is described in detail. The structure, parts, instruments and devices used in the machine are described and compared with their state-of-the-art rivals. The design is considering a completely new system module. The axes of measurement of the three laser measurement devices intersect with the probe tip, thus, the angular errors due to the effect of Abbé error are eliminated.

The novel micro-CMM also features a singularity free movement within the whole workspace. Moreover, it provides that very large workspace is reachable, where the targeted work envelope of 100 mm range in all three directions can easily be covered. An algorithm to define the workspace was implemented.

Moreover, the proposed novel design provides movement in 3-DOF, translation in z direction, rotation around x axis, and rotation around y axis. The position of the probe is determined analytically by solving the direct position kinematic module. The solution to the kinematics problem explicitly define the coordinates of the probe in the Cartesian coordinate system (x,y,z). The inverse position kinematic problem of the system is solved numerically.

In this research, a fully functional prototype of the novel micro-CMM was built, for the purpose of demonstrating the machine and to prove the design concept, as well as to validate the kinematic and error models.

A computer interface with LabView software was developed, where the algorithms of the movement and measurement modules were programed using the Python programming language and were linked to the control software.

Geometrical parameters of the machine structure were identified using a master CMM, and the uncertainties of these parameters were estimated and used as an input to the error model.

A reliable kinematic error modelling technique to estimate and analyse the errors was derived analytically. The theory of error propagation was used, where the results of the error modelling are given by the variance-covariance matrix.

The results of the analytical kinematic error model were verified numerically. The Monte-Carlo method was used to simulate the results. Comparing the results of the error model, both analytical and numerical, show that they represent a very good match and follow the same trend.

A set of experiments was carried out to characterized the micro-CMM and to practically confirm the validity of the proposed system model. A master CMM was used to validate the solution of the kinematic model. Results show that the position kinematic model is efficient in determining the position when compared with measurements taken by means of the master CMM. An average difference of less than 0.5 mm over 30 points was achieved. This result of the micro-CMM measurements falls within the error budget of approximately 0.75 mm estimated by the proposed analytical error model.

The significance of the errors associated with the geometric parameters on the positioning accuracy of the probe show that the uncertainty in determining the lengths of the links is responsible for the most significant contribution to the overall machine error, followed by the position of the pivot points in the vertical direction.

Practical experiments confirmed that the error model is efficient in estimating the expected error in the measurements. It is possible to achieve measurements in the submicron regime with this concept, provided that state-of-the-art instruments and components are to be used, taking into consideration all other important factors, such as: operating in a temperature controlled environment, implementing error compensation and good calibration models.

9.2   Recommendations

In order to achieve the ultimate goal of measuring 3D objects with accuracies in the regime of nano meter, more research and attention may be focused on the following issues in the future:

- To enhanced the stiffness and structure optimization.
- To build an accurate prototype with state-of-the-art components and devices.
- To conduct a kinematics calibration and error compensation study.
- To perform a comprehensive study on the effect of dynamic errors.
- To extend the error model to include the effects of dynamic errors.
- To investigate the possibility of other practical applications of this design.

REFERENCES

[1]   H N Hansen, K Carneiro, H Haitjema, and L De Chiffre, "Dimensional micro and nano metrology," Annals of The International Academy for Production Engineering CIRP, vol. 55, no. 2, pp. 721–743, 2006.

[2]   P Bariani, "Dimensional metrology for microtechnology," Department of Manufacturing Engineering and Management, Technical University of Denmark, Copenhagen, PhD Thesis 2005.

[3]   P McKeown, "Nanotechnology-special article," in Nano-metrology in Precision Engineering, Hong Kong, 1998, pp. 5–55.

[4]   K C Fan, Y Chen, and W Wang, "Probe technologies for micro / nano measurements," in 7th IEEE International Conference on Nanotechnology, Hong Kong, 2007, pp. 989–993.

[5]   A Weckenmann, T Estler, G Peggs, and D McMurtry, "Probing systems in dimensional metrology," The International Academy for Production Engineering CIRP Annals Manufacturing Technology, vol. 53, no. 2, pp. 657–684, 2004.

[6]   "Guide to the expression of uncertainty in measurement (GUM) — supplement 1: numerical methods for the propagation of distributions using a Monte Carlo method," Joint Committee for Guides in Metrology, (ISO), Draft 101:2008, 2008.

[7]   C J Feng, A L Saal, J G Salsbury, and A R Ness, "Design and analysis of experiments in CMM measurement uncertainty study," Precision Engineering, vol. 31, pp. 94–101, 2007.

[8]   K McCarthy, "Accuracy in positioning systems," in The Motion Control Technology, Massachusetts, 1991, pp. 19–21.

[9]   J D Claverley and R K Leach, "A vibrating micro-scale CMM probe for measuring high aspect ratio structures," Microsystem Technologies, vol. 16, no. 9, pp. 1507–1512, 2009.

[10]   J R Taylor, An introduction to error analysis: the study of uncertainties in physical measurements, 2nd ed. USA: University Science Books, 1999.

[11]   BIPM, IEC, IFCC, ILAC, ISO, IUPAC, IUPAP, and OIML, International vocabulary of basic and general terms in metrology VIM, 3rd ed. Geneva, Switzerland: International Organization for Standardization, 2004.

[12]   (2102, May) The National Institute of Standards and Technology. [Online]. http://www.nist.gov/traceability/index.cfm

[13]   K C Fan, Y T Fei, X F Yu, Y J Chen, W L Wang, F Chen, and Y S Liu, "Development of a low-cost micro-CMM for 3D micro/nano measurements," Measurement Science and Technology, vol. 17, no. 3, pp. 524–532, 2006.

[14]   K Takamasu, B W Guo, R Furutani, and S Ozano, "Basic concept of feature-based metrology," in 6th ISMQC symposium, Vienna, 1998.

[15]   G N Peggs, A Lewis, and R K Leach, "Measuring in three dimensions at the mesoscopic level," in ASPE Winter Topical Meeting—Machines and Processes for Micro-scale and Meso-scale Fabrication, Metrology and Assembly, FL, USA, 2003, pp. 53–57.

[16]   T Hausottee and G Jäger, "Traceable nanometrology with a nanopositioning and nanomeasuring machine," Journal of the Chinese Society of Mechanical Engineers, vol. 25, pp. 399–404, 2004.

[17]   K C Fan, C L Chu, S H Chang, and T T Chung, "Development of a micro-CMM for nanometrology," in KSPE Spring Conference, Keynote paper, 2001, pp. 1–6.

[18]   S Liang, "Mechanical machining and metrology at micro/nano scale," in
        The First International Conference on Positioning Technology, Keynote
        speech, Hamamatsu, Japan, 2004, pp. 23–28.

[19]   L Wang and J Xi, Smart devices and machines for advanced
        manufacturing, 1st ed.: Springer Publishing Company, 2008.

[20]   M Vermeulen, P Rosielle, and P Schellekens, "Design of a high-precision
        3D-coordinate measuring machine," The International Academy for
        Production Engineering CIRP Annals - Manufacturing Technology, vol.
        47, no. 1, pp. 447–50, 1998.

[21]   Nanometer F25 Measuring. (2011, August) Industrial Measuring
        Technology from Carl Zeiss. [Online].
        http://www.micromanu.com/library/14/F25_Brochure.pdf

[22]   Robotics Nanometer Precision. (2011, August) Alio industries. [Online].
        http://www.alioindustries.com/product_brochures/Hexapod___Tripod_Bro
        chure_2006-04.pdf

[23]   Product overview Micropositioning. (2011, August) physik instrumente.
        [Online].
        http://www.physikinstrumente.com/en/pdf_extra/2009_PI_Micropositionin
        g_Brochure.pdf

[24]   P Yang, T Takamura, S Takahashi, K Takamasu, O Sato, S Osawa, and T
        Takatsuji, "Development of high-precision micro-coordinate measuring
        machine: Multi-probe measurement system for measuring yaw and
        straightness motion," Precision Engineering, vol. 35, pp. 424–430, 2011.

[25]   K Takamasu, "Present problems in coordinate metrology for nano and
        micro scale measurements," Journal of Metrology Society of India, vol.
        26, no. 1, pp. 3–14, 2011.

[26]   K Takamasu, "Mesoscale profile measurement improved by intelligent measurement technology," Journal of Japan Society for Precision Engineering, vol. 74, pp. 213–216, 2008.

[27]   (2012, May) International Metrology Systems Ltd web site. [Online]. http://www.virtual-dmis.com/about.aspx.htm

[28]   (2012, May) COORD3 Metrology. [Online]. http://www.coord3-cmm.com/50-years-of-coordinate-measuring-machine-industry-developments-and-history/

[29]   T Oiwa, "New coordinate measuring machine featuring a parallel mechanism," International Journal of the Japan Society for Precision Engineering, vol. 31, no. 3, pp. 232–233, 1997.

[30]   P R Ouyang, R C Tjiptoprodjo, W J Zhang, and G S Yang, "Micro-motion device technology: the state of arts review," The International Journal of Advanced Manufacturing Technology, vol. 38, no. 4-5, pp. 463–478, 2007.

[31]   A Rugbani, and K Schreve, "The use of parallel mechanism micro-CMM in micrometrology," in 4th Robotics & Mechatronics Conference, Pretoria South Africa, 2011.

[32]   K C Fan, F Yetai, and Y Xiaofen, "Development of a micro-CMM," in International Manufacturing Leaders Forum on "Global Competitive Manufacturing", Adelaide, Australia, 2005, pp. 1–7.

[33]   F Gao, W M Lin, and X C Zhao, "New kinematic structures for 2-, 3-, 4-, and 5-DOF parallel manipulator designs," Mechanism and Machine Theory, vol. 37, pp. 1395–1411, 2002.

[34]   X J Liu, J S Wang, and G Pritschow, "A new family of spatial 3-DOF fully-parallel manipulators with high rotational capability," Mechanism and Machine Theory, vol. 40, pp. 475–494, 2005.

122

[35]   D Liu, Y Xu, and R Fei, "Study of an intelligent micromanipulator,"
         Journal of Material Processing Technology, vol. 139, pp. 77–80, 2003.

[36]   A collection of contributions based on lectures presented at the Third
         Toyota Conference, Integrated micromotion systems: micromachining,
         control and applications, Fumio Harashima, Ed. Aichi, Japan: Elsevier
         Science Ltd, 1990.

[37]   M N Zubir, "Developemtn of a high precision flex-based microgripper,"
         Precision Enginering, vol. 33, pp. 362–270, 2009.

[38]   Y Bang, K M Lee, J Kook, W Lee, and I S Kim, "Micro parts assembly
         system with micro gripper," IEEE Transactions on Robotics, vol. 21, no. 3,
         pp. 465–470, 2005.

[39]   J D Gilsinn, B N Damazo, R Silver, and Hu Zhou, "A macro-microsystem
         for a scanning tunneling microscope," in World Automation Congress
         (WAC) 2002 as Part of the International Symposium on Robotics &
         Applications (ISORA), Orlando, FL, 2002, pp. 1–10.

[40]   L W Tsai, Mechanism design, enumeration of kinematic structures
         according to function, Frank Kreith, Ed. Boca Raton: CRC Press, 2001.

[41]   J P Merlet, Parallel robots, 2nd ed., G.M.L. Gladwell, Ed. Sophia-
         Antipolis, France: Springer, 2006.

[42]   H J Su, P Dietmaier, and J M McCarthy, "Trajectory planning for
         constrained parallel manipulators," Journal of Mechanical Design, vol.
         125, pp. 709–716, 2003.

[43]   W L V Pollard, "Position controlling apparatus," Grant US2,286,571 A,
         June 16, 1942.

[44]   R Clavel, "DELTA, a fast robot with parallel geometry," in 18th
         International Symposium on Industrial Robot, Lausanne, 1988, pp. 91–
         100.

[45]   P Wenger and D Chablat, "Kinematic analysis of a new parallel machine-tool: the Orthoglide," in Advances in Robot Kinematics, Piran, 2000, pp. 305–314.

[46]   X Kong and C M Gosselin, "Kinematics and singularity analysis of a novel type of 3-CRR 3-DOF translational parallel manipulator," International Journal of Robotics Research, vol. 21, no. 9, pp. 791–798, 2002.

[47]   L W Tsai, "Kinematics of a three-DOF platform with three extensible limbs," in Advances in Robot Kinematics, Portoroz-Bernadin, 1996, pp. 401–410.

[48]   R Di Gregorio, "A new parallel wrist using only revolute pairs: the 3-RUU wrist," Robotica, vol. 19, no. 3, pp. 305–309, 2001.

[49]   J M Hervé and M Karouia, "The novel 3-RUU wrist with no idle pair," in Workshop on Fundamental Issues and Future Research Directions for Parallel Mechanisms and Manipulators, Québec, 2002, pp. 3–4.

[50]   Y Fang and L W Tsai, "Structure synthesis of a class of 3-DOF rotational parallel manipulators," IEEE Trans. on Robotics and Automation, vol. 20, no. 1, pp. 117–121, 2004.

[51]   R Di Gregorio, "Kinematics of the 3-RSR wrist," IEEE Trans. on Robotics, vol. 20, no. 4, pp. 750–754, 2004.

[52]   C Gang, S R Ge, and Y Wang, "Error analysis of three degree-of-freedom changeable parallel measuring mechanism," Journal of China University of Mining & Technology, vol. 17, no. 1, pp. 101–104, 2007.

[53]   K H Hunt, "Structural kinematics of in parallel-actuated robot arms," ASME Journal of Mechanisms, Transmissions, and Automation in Design, vol. 105, pp. 705–712, 1983.

[54]   R Clavel and Delta, "A fast robot with parallel geometry," in International Symposium on Industrial Robots, Switzerland, 1988, pp. 91–100.

[55]   J J Craig, Introduction to robotics: mechanics and control, 2nd ed. New York, USA: Addison and Wesley, 1989.

[56]   K Sugimoto, J Duffy, and K H Hunt, "Special configurations of spatial mechanisms and robot arms," Mechanism and Machines Theory, vol. 17, no. 2, pp. 119–132, 1982.

[57]   Z M Ji, "Study of planar three-degree-of-freedom 2-RRR parallel manipulator," Mechanism and Machine Theory, vol. 38, pp. 409–416, 2003.

[58]   X J Liu, J S Wang, and G Pritschow, "Kinematics, singularity and workspace of planar 5R symmetrical parallel mechanisms.," Mechanism and Machine Theory, vol. 41, pp. 145–169, 2006.

[59]   Z Meng, and R S Che, "Error model and error compensation of six-freedom-degree parallel mechanism CMM," Journal of Harbin Institute of Technology, vol. 36, no. 3, pp. 317–320, 2004.

[60]   M Li, R Weibin, S Lining, and L Zheng, "Error compensation for a parallel robot using back propagation neural networks," in International Conference on Robotics and Biomimetics, Kunming, 2006, pp. 1658–1663.

[61]   Z Meng, R S Che, Q C Huang, and Z J Yu, "The direct-error-compensation method of measuring the error of a six-freedom-degree parallel mechanism CMM," Journal of Materials Processing Technology, vol. 129, pp. 574–578, 2002.

[62]   G Pritschow, C Eppler, and T Garber, "Influence of the dynamic stiffness on the accuracy of PKM," in 3rd Chemnitz Parallel Kinematics Seminar, Chemnitz, 2002, pp. 313–333.

[63]   J A Soons, "On the geometric and termal errors of a hexapod machine tools," in The First European-American Forum on Parallel Kinematic Machines, Milano, 1998, pp. 151–170.

[64]   M Weck and D Staimer, "Accuracy issues of parallel kinematic machine tools," in Proceedings of the Institution of Mechanical Engineers, Part K: 216, vol. 216, 2002, pp. 51–58.

[65]   R Yao, X Tang, and T Li, "Error analysis and distribution of 6-SPS and 6-PSS reconfigurable," Tsinghua Science and Technology, vol. 15, no. 5, pp. 547–554, 2010.

[66]   T Huang, Y Li, G Tang,S Li, X Zhao, D J Whitehouse, D G Chetewyn, and X Liu, "Error modeling, sensitivity analysis and assembly process of a 3-DOF parallel mechanism," Science in China (Series E), vol. 45, no. 5, pp. 628–635, 2002.

[67]   Z Pandilov and V Dukovski, "Survey of the dominant error types at parallel kinematics machine tools," International Journal of Engineering, vol. 8, no. 1, pp. 193–196, 2010.

[68]   L W Tsai, Robot analysis-the mechanics of serial and parallel manipulators. New York, USA: Wiley, 1999.

[69]   M Raghavan, "The Stewart platform of general geometry has 40 configurations," ASME Journal of Mechanical Design, vol. 115, pp. 277–82, 1993.

[70]   M Abderrahim and AR Whittaker, "Kinematic model identification of industrial manipulators," Journal of Robotic Computer Integrated, vol. 16, pp. 1–8, 2000.

[71]   R Pierre, A Nicolas, and M Philippe, "Kinematic calibration of parallel mechanisms: a novel approach using legs observation," IEEE Transactions on Robotics, vol. 4, pp. 529–538, 2005.

[72]   H Mahir and N Leila, "Design modification of parallel manipulators for optimum fault tolerance to joint jam," Mechanism and Machine Theory, vol. 40, pp. 559–577, 2005.

[73]   C Lin, X Tang, and L Wang, "Precision design of modular parallel kinematic machines," Tool Engineering, vol. 41, no. 8, pp. 38–42, 2007.

[74]   W Jian and M Oren, "On the accuracy of a stewart platform—Part I: The effect of manufacturing tolerances," in IEEE International Conference on Robotics and Automation Los Alamitos, Atlanta, GA, USA, 1993, pp. 114–120.

[75]   G Chunhe, Y Jingxia, and N Jun, "Nongeometric error identification and compensation for robotic system by inverse calibration," International Journal of Machine Tools and Manufacture, vol. 40, pp. 2119–2137, 2000.

[76]   A J Patel and K F Ehmann, "Calibration of a hexapod machine tool using a redundant leg," International Journal of Machine Tools and Manufacture, vol. 40, pp. 489–512, 2000.

[77]   A H Slocum, Precision machine design, illustrated edition ed. USA: Society of Manufacturing Engineers, 1992.

[78]   A Majarena, J Santolaria, and D Samper, "An overview of kinematic and calibration models using internal/external sensors or constraints to improve the behaviour of spatial parallel mechanisms," Sensors, vol. 10, pp. 10256–10297, 2010.

[79]   E F Fichter, "A stewart platform-Based manipulator: general theory and practical construction," International Journal of Robotics Research, vol. 5, pp. 157–182, 1986.

[80]   J P Merlet, "An algorithm for the forward kinematics of general 6 DOF parallel manipulators.," Rapports de recherche-INRIA, vol. 1331, pp. 1–27, 1990.

[81]   J P Merlet, Parallel robots, 1st ed., G Gladwell, ed. Norwell, MA, USA: Kluwer Academic Publishers, 2000.

[82]   Y Lu, Y Shi, and B Hu, "Kinematic analysis of two novel 3-UPU I and 3-UPU II PKMs," Robotics and Autonomous Systems, vol. 56, pp. 296-305, 2008.

[83]   H H Cheng, J J Lee, and R Penkar, "Kinematic analysis of a hybrid serial-and-parallel-driven redundant industrial manipulator," International Journal of Robotics and Automation, vol. 10, pp. 159–166, 1995.

[84]   N M Rao, "Dimensional synthesis of a spatial 3-RPSparallel manipulator for a prescribed range of motion of spherical joints," Mechanism and Machine Theory, vol. 44, pp. 477–486, 2009.

[85]   C Innocenti and V Parenti-Castelli, "Closed-form direct position analysis of A 5–5 parallel mechanism," Journal of Mechanical Design, vol. 115, pp. 515–526, 1993.

[86]   C Innocenti and V Parenti-Castelli, "Forward kinematics of the general 6–6 fully parallel mechanism: an exhaustive numerical approach va a mono-dimensional-search algorithm," Journal of Mechanical Design, vol. 115, pp. 932–947, 1993.

[87]   J P Merlet, "Closed-form resolution of the direct kinematics of parallel manipulators using extra sensors data," in IEEE International Conference on Robotics and Automation, Atlanta, GA, USA, 1993, pp. 200–204.

[88]   ISO (Internacional Organization for Standardizatio, "General requirements for the competence of testing and calibration laboratories," in ISO/IEC 17025, 2nd ed. Geneva, Switzerland: International Organization for Standardization, 2005.

[89]   J M Hollerbach, A Nahvi, and V Hayward, "Calibration of a parallel robot using multiple kinematics closed loops," in IEEE International Conference on Robotics and Automation, San Diego, CA, 1994, pp. 407–413.

[90]   D Daney, "Algebraic elimination for parallel robot calibration," in the 11 World Congress in Mechanism and Machine Science, Tianjin China, 2004.

[91]   G Yang, I M Chen, K Lim, and S Huat-Yeo, "Simultaneous base and tool calibration of a self-calibrated modular parallel robot," Robotica, vol. 20, no. 4, pp. 367–374, 2002.

[92]   P Last, D Schutz, A Raatz, and J Hesselbach, "Singularity based calibration of 3 dof fully parallel planar manipulators," in 12th IFToMM World Congress, Besacon, 2007.

[93]   E E Hernández-Martínez, C S López-Cajún, and J C Jáuregui-Correa, "Calibration of parallel manipulators and their application to machine tools. A state of the art survey," Ingeniería Investigación y Tecnología, vol. XI, no. 2, pp. 141–154, 2010.

[94]   Z S Roth, B W Mooring, and R Bahram, "An overview of robot calibration," IEEE Journal of Robotics and Automation, vol. 3, no. 5, pp. 377–385, 1987.

[95]   K Schreve, "Micrometrology," Stellenbosch University, Stellenbosch, Internal Report 2013.

[96]   R J Craig, "Structural design for a mcro-coordinate measuring machine," Stellenbosch University, Stellenbosch, Final Year Project Report 2011.

[97]   H Blaauw, "The measurement and calibration of high accuracy spherical joints," Stellenbosch Univeristy, Stellenbosch, Final Year Project Report 2012.

[98]   Z Zhao and F G Perey, "The covariance matrix of derived quantities and their combination," Oak Ridg National Laboratory, Beijing, China, Technical report ORNL/TM-12106, 1992.

[99]   J C Clarke, "Modelling uncertainty: a primer," Department of Engineering, Oxford University, Oxford, UK, Technical report 1998.

[100]   P B Dhanish and J Mathew, "Effect of CMM point coordinate uncertainty on uncertainties in determination of circular features," Measurement, vol. 39, pp. 522–531, 2006.

[101]   B W J J A Van Dorp, H Haitjema, and F L M Delbre, "A virtual CMM using Monte Carlo methods based on frequency content of the error signal," in The International Society for Optics and Photonics SPIE, Germany, Munich, 2001, pp. 158–167.

[102]   M Brizard, M Megharfi, and C Verdier, "Absolute falling-ball viscometer: evaluation of measurement uncertainty," Metrologia, vol. 42, pp. 298–303, 2005.

[103]   S J Canning, J C Ziegert, and T L Schm, "Coordinate metrology uncertainty using parallel kinematic techniques," International Journal of Machine Tools & Manufacture, vol. 47, pp. 658–665, 2007.

[104]   K N Whitley and A F Blackwell, "Visual programming in the wild: A survey of LabVIEW programmers," Journal of Visual Languages and Computing, no. 12, pp. 435–472, 2001.

[105]   C Elliott, V Vijayakumar, W Zink, and R H, "National Instruments LabVIEW: A programming environment for laboratory automation and measurement, in Technical Brief," pp. 17–24, 2007.

[106]   S Smith and C Robbi, "Subnanometer surface texture and profile measurement with 'Nanosurf 2'," Annals of The International Academy for Production Engineering CIRP, vol. 37, no. 1, pp. 519–522, 1988.

[107]   A. Rugbani and K. Schreve, "Modelling and analysis of the geometrical errors of a parallel manipulator micro-CMM," in Precision Assembly Technologies and Systems, S. Ratchev, Ed. Springer Berlin Heidelberg, 2012, pp. 105–117.

APPENDICES

Appendix A: Micro-CMM detailed design drawings

Micrometrology coordinate measurement machine comprises a

(1) frame

(2) three parallel upright frame members supporting

(3) three movable legs

(4) runner blocks

(5) probe support unit

(6) spherical joint

(7) support drive mechanism

(8) linear motors

(9) laser sensors

(10) probe

(11) centre of a probe ball
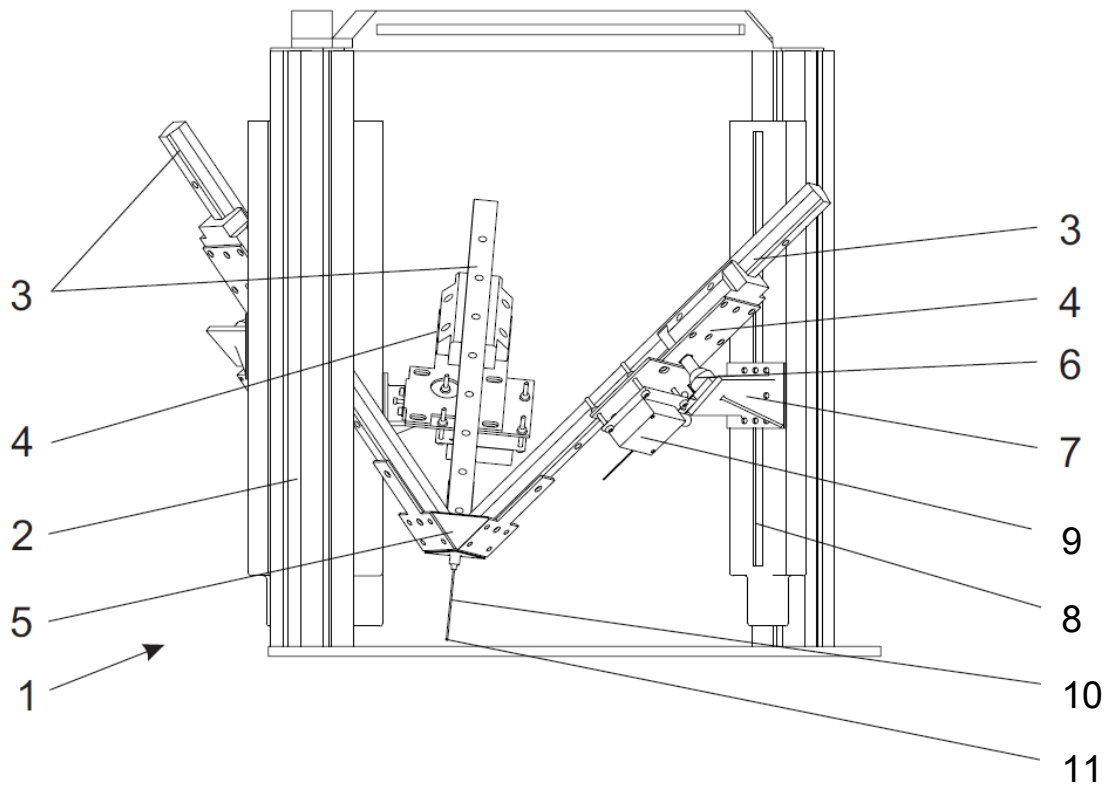
Figure A. 1

Figure A. 2

133
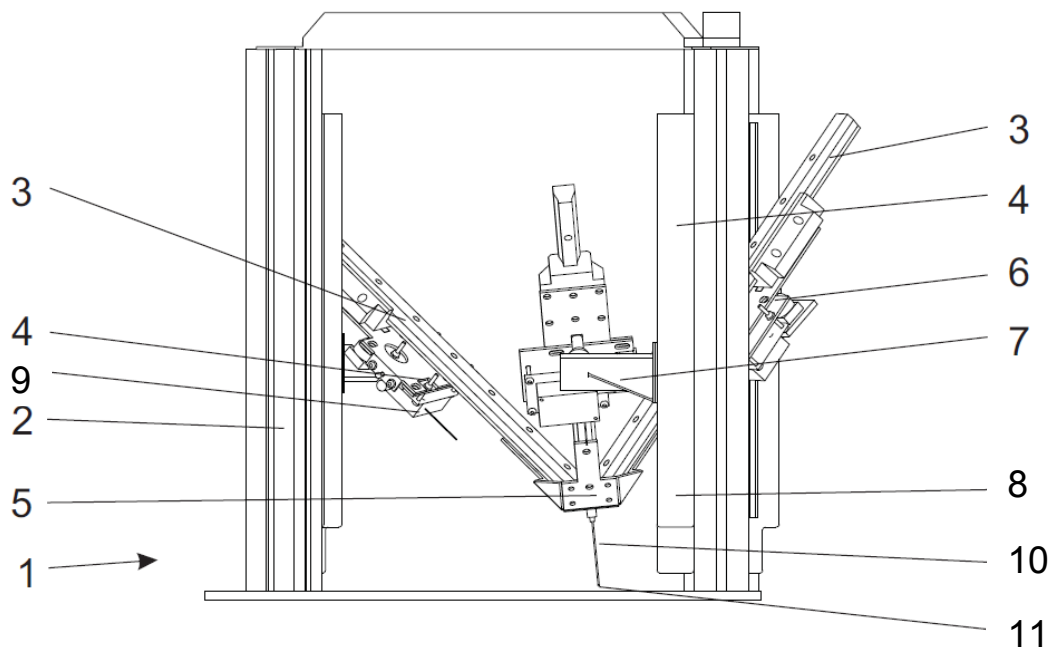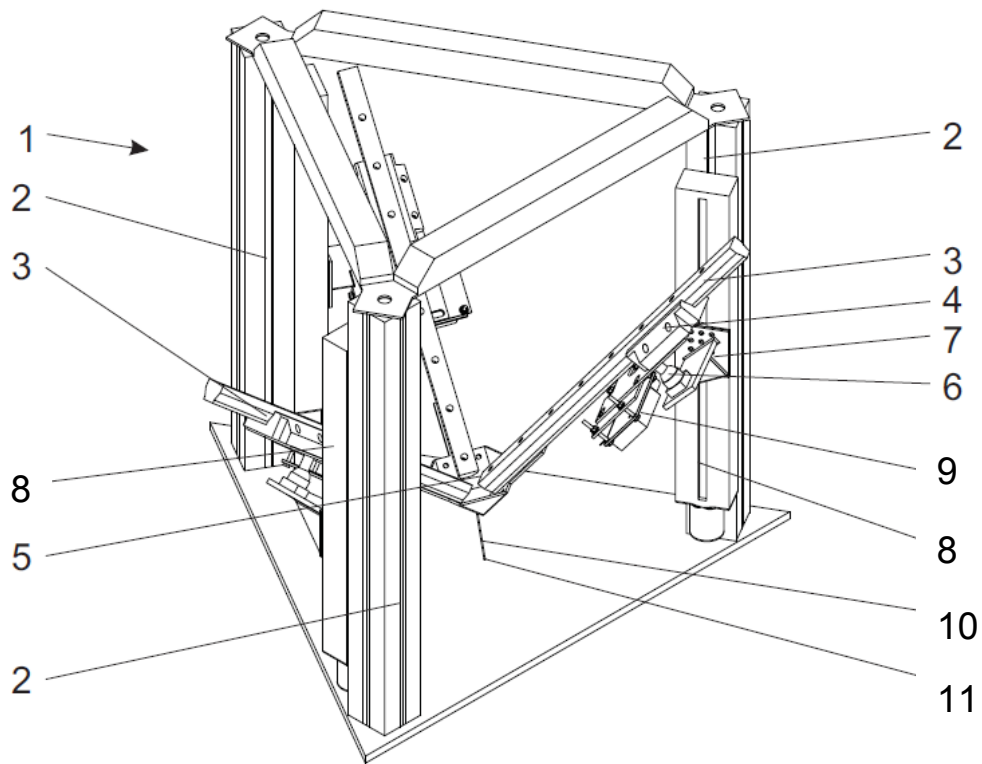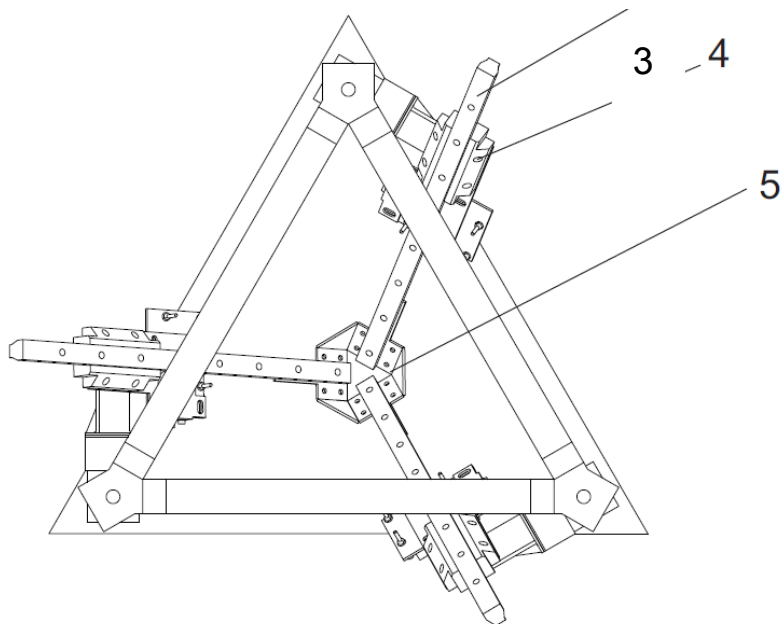
Figure A. 3

Figure A. 4
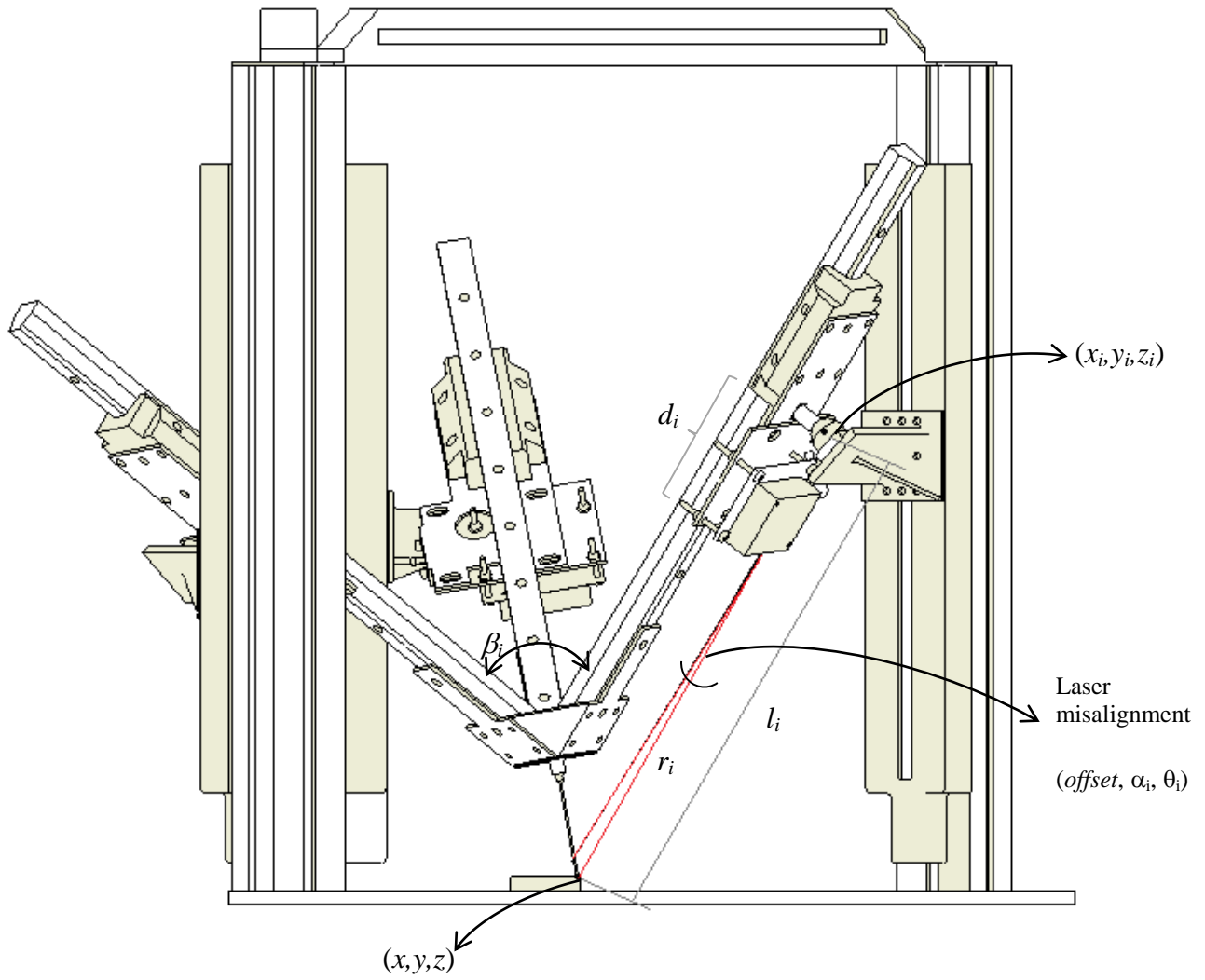
Figure A.5: Kinematic parameters of leg i

Appendix A-1: Detailed design drawings for the novel micro-CMM parts
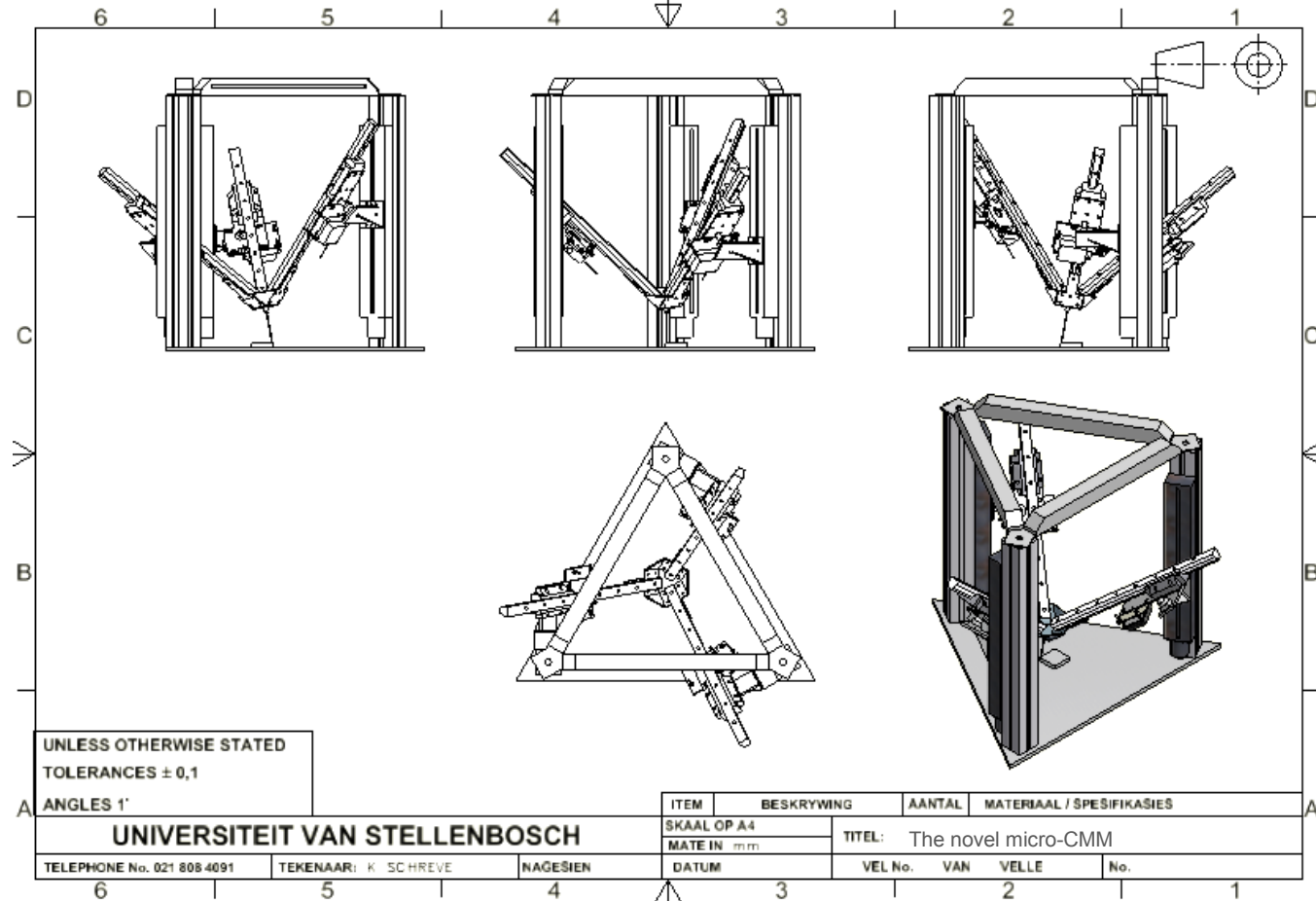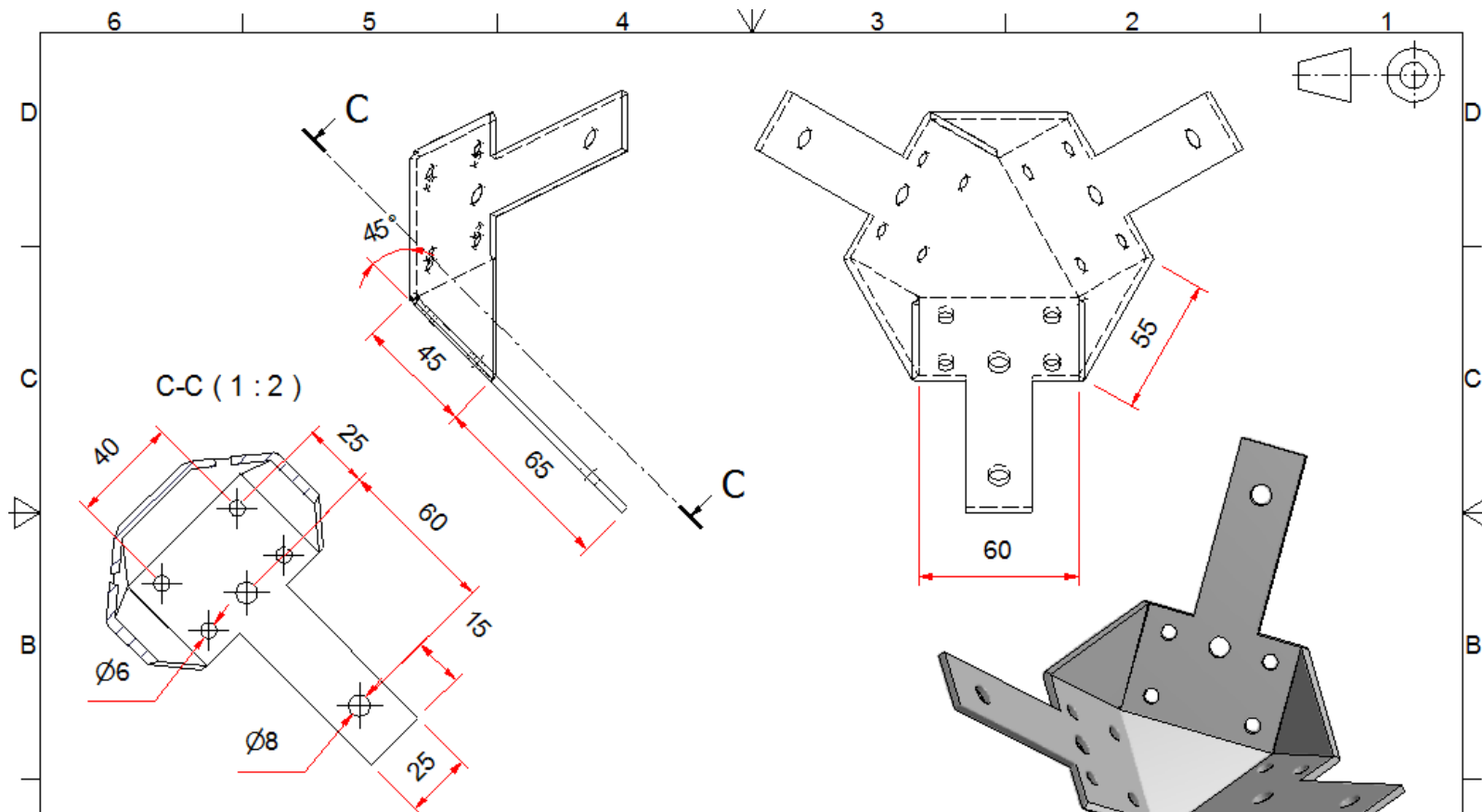
UNLESS OTHERWISE STATED
TOLERANCES ± 0,1
ANGLES 1°

UNIVERSITEIT VAN STELLENBOSCH

TELEPHONE No. 021 808 4091   TEKENAAR: K SCHREVE   NAGESIEN

ITEM	BESKRYWING	AANTAL	MATERIAAL / SPESIFIKASIES

SKAAL OP A4
MATE IN mm

TITEL: The novel micro-CMM

VEL No.   VAN   VELLE   No.

DATUM

C-C (1 : 2)

45°

45

65

40

25

60

15

25

Ø6

Ø8

55

60

ITEM	BESKRYWING	AANTAL	MATERIAAL / SPESIFIKASIES	

UNIVERSITEIT VAN STELLENBOSCH

SKAAL OP A4

MATE IN mm

TITEL: PROBE CARRYING UNIT
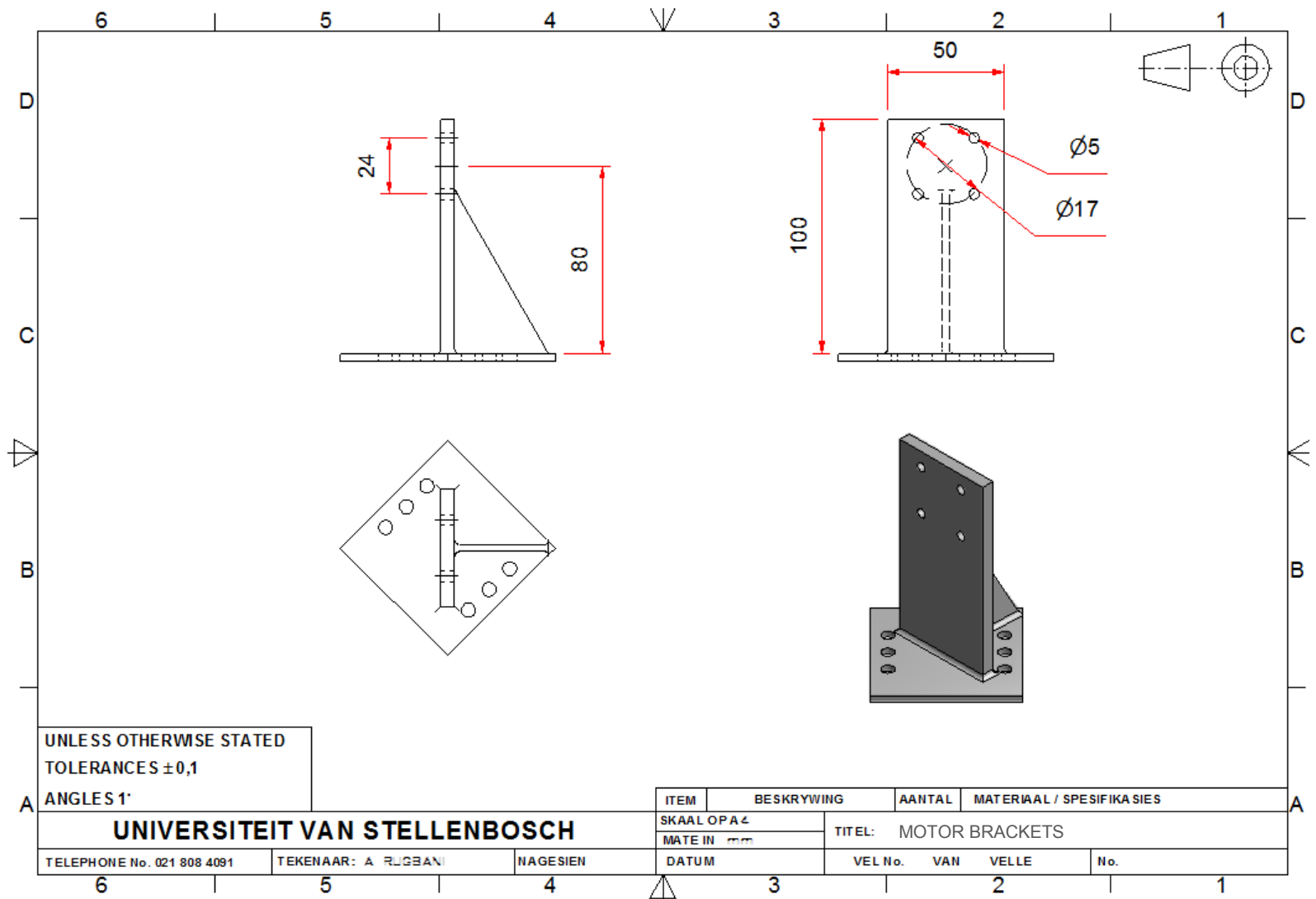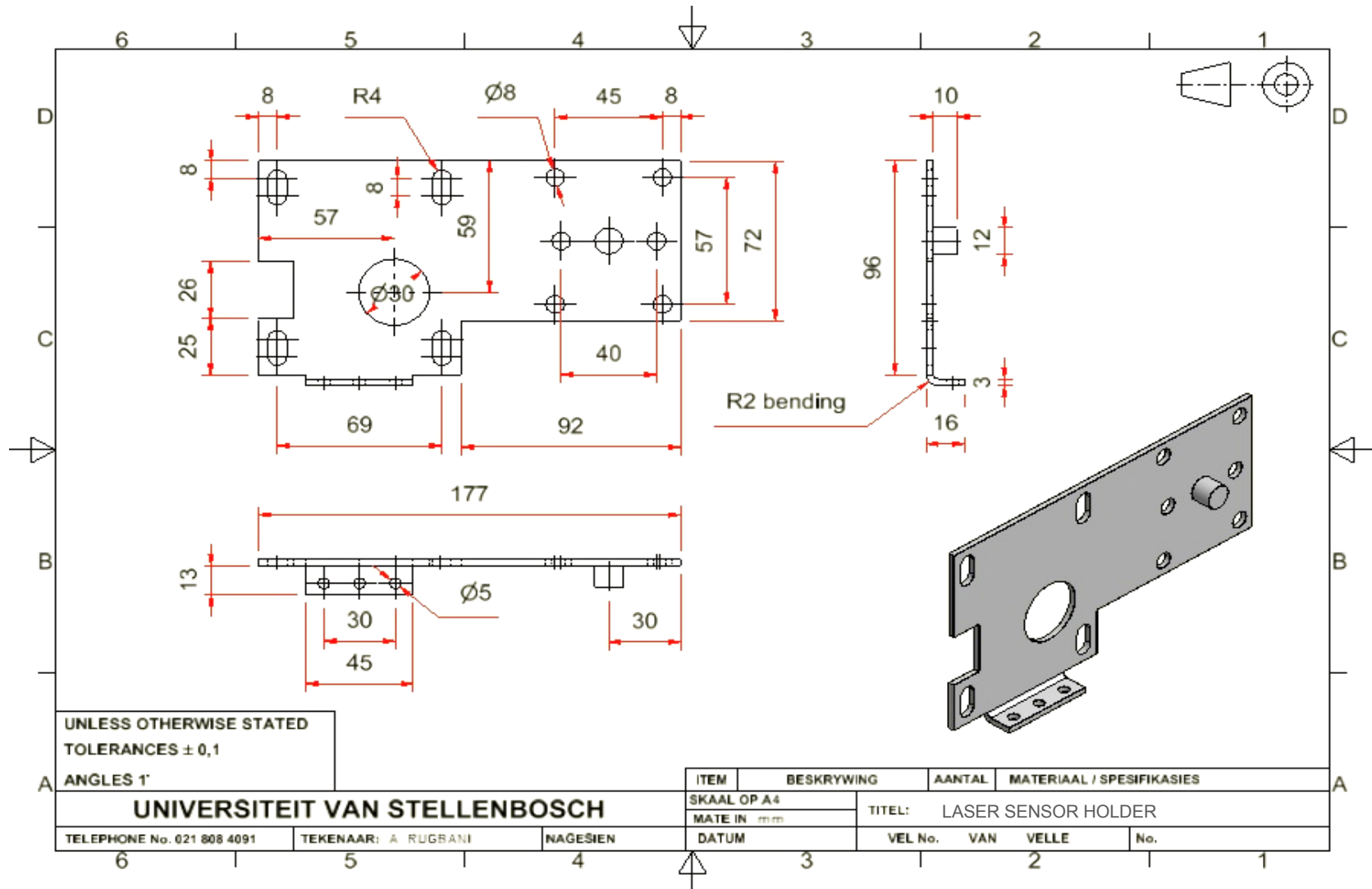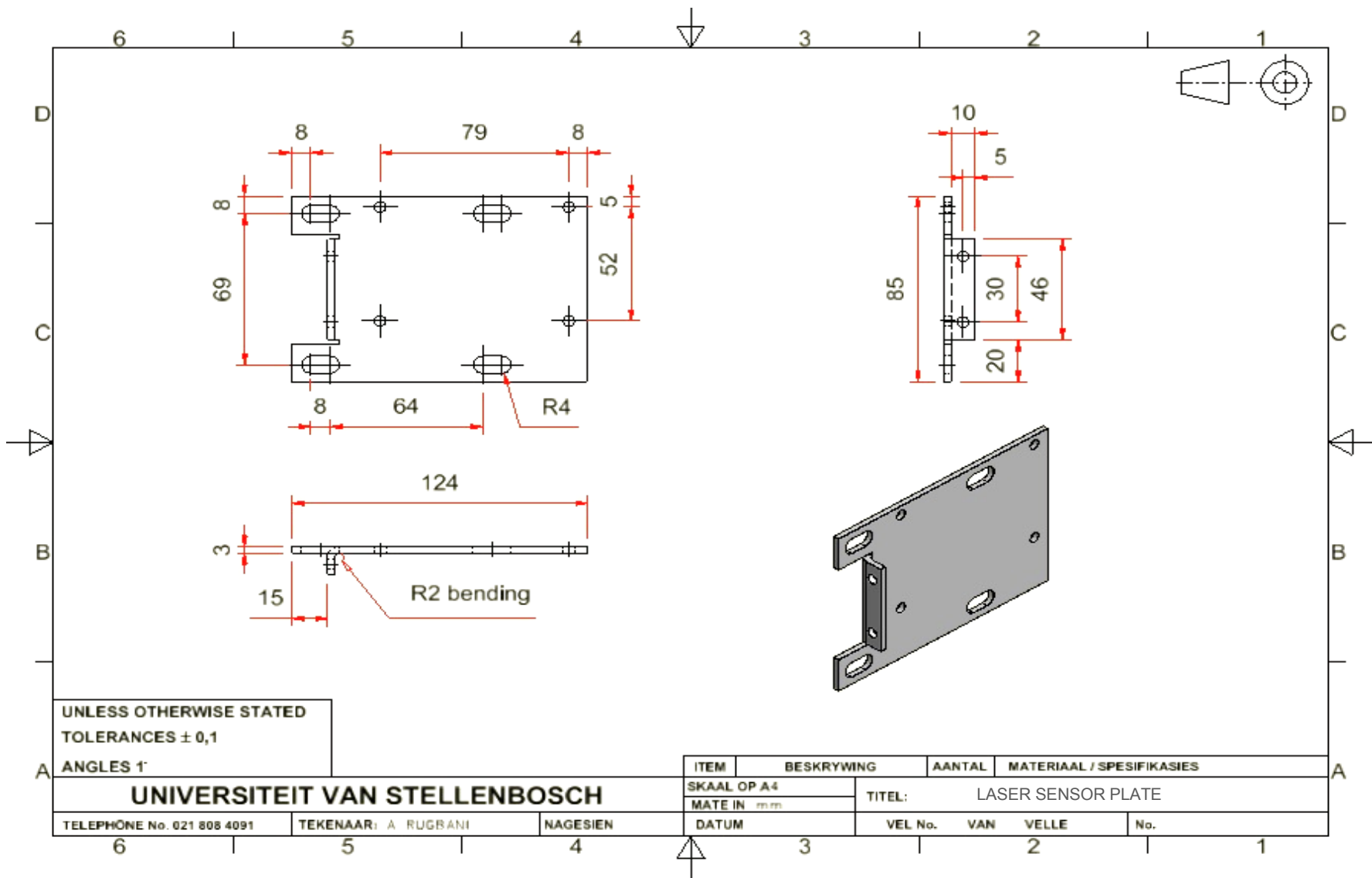
TELEPHONE No. 021 808 4091

TEKENAAR: A RUGBANI

NAGESIEN

DATUM

VEL No.	VAN	VELLE		No.

137

50

24

80

100

Ø5

Ø17

ITEM	BESKRYWING	AANTAL	MATERIAAL / SPESIFIKASIES

UNIVERSITEIT VAN STELLENBOSCH

| SKAAL OP A4 | | TITEL: | MOTOR BRACKETS |
| MATE IN mm | | | |

| TELEPHONE No. 021 808 4091 | TEKENAAR: A RUGBANI | NAGESIEN | DATUM | VEL No. | VAN | VELLE | No. |

138

8
79
8
8
5
69
52
8
64
R4

124
3
15
R2 bending

10
5
85
30
46
20

UNLESS OTHERWISE STATED
TOLERANCES ± 0,1
ANGLES 1˚

UNIVERSITEIT VAN STELLENBOSCH

TELEPHONE No. 021 808 4091

TEKENAAR: A RUGBANI

NAGESIEN

ITEM	BESKRYWING	AANTAL	MATERIAAL / SPESIFIKASIES

SKAAL OP A4
MATE IN mm

TITEL: LASER SENSOR PLATE

DATUM

VEL No.   VAN   VELLE

No.

LASER SENSOR ADJUSTMENT SYSTEM

ANGLES 1°

UNIVERSITEIT VAN STELLENBOSCH

TELEPHONE No. 021 808 4091 | TEKENAAR: A RUGBANI | NAGESIEN

ITEM	BESKRYWING	AANTAL	MATERIAAL / SPESIFIKASIES

SKAAL OP A4
MATE IN mm
TITEL:
DATUM

VEL No.	VAN	VELLE	No.

340

25

Ø6

50

R1 bending

60

60

10

R5

20 65

65

30

ITEM	BESKRYWING		AANTAL	MATERIAAL / SPESIFIKASIES

UNIVERSITEIT VAN STELLENBOSCH

SKAAL OP A4		TITEL:	MOTOR HOLDER	
MATE IN mm				

TELEPHONE No. 021 808 4091	TEKENAAR: A. RUGRANI	NAGESIEN	DATUM	VEL No.	VAN	VELLE	No.

142

Appendix A-2: Detailed design drawings for the initial micro-CMM prototype

UNLESS OTHERWISE STATED
TOLERANCES ± 0,1
ANGLES 1˚

UNIVERSITEIT VAN STELLENBOSCH

TELEPHONE No. 021 808 4091   TEKENAAR: K SCHREVE   NAGESIEN

ITEM	BESKRYWING	AANTAL	MATERIAAL / SPESIFIKASIES

SKAAL OP A4
MATE IN mm
TITEL:
DATUM   VEL No.   VAN   VELLE   No.
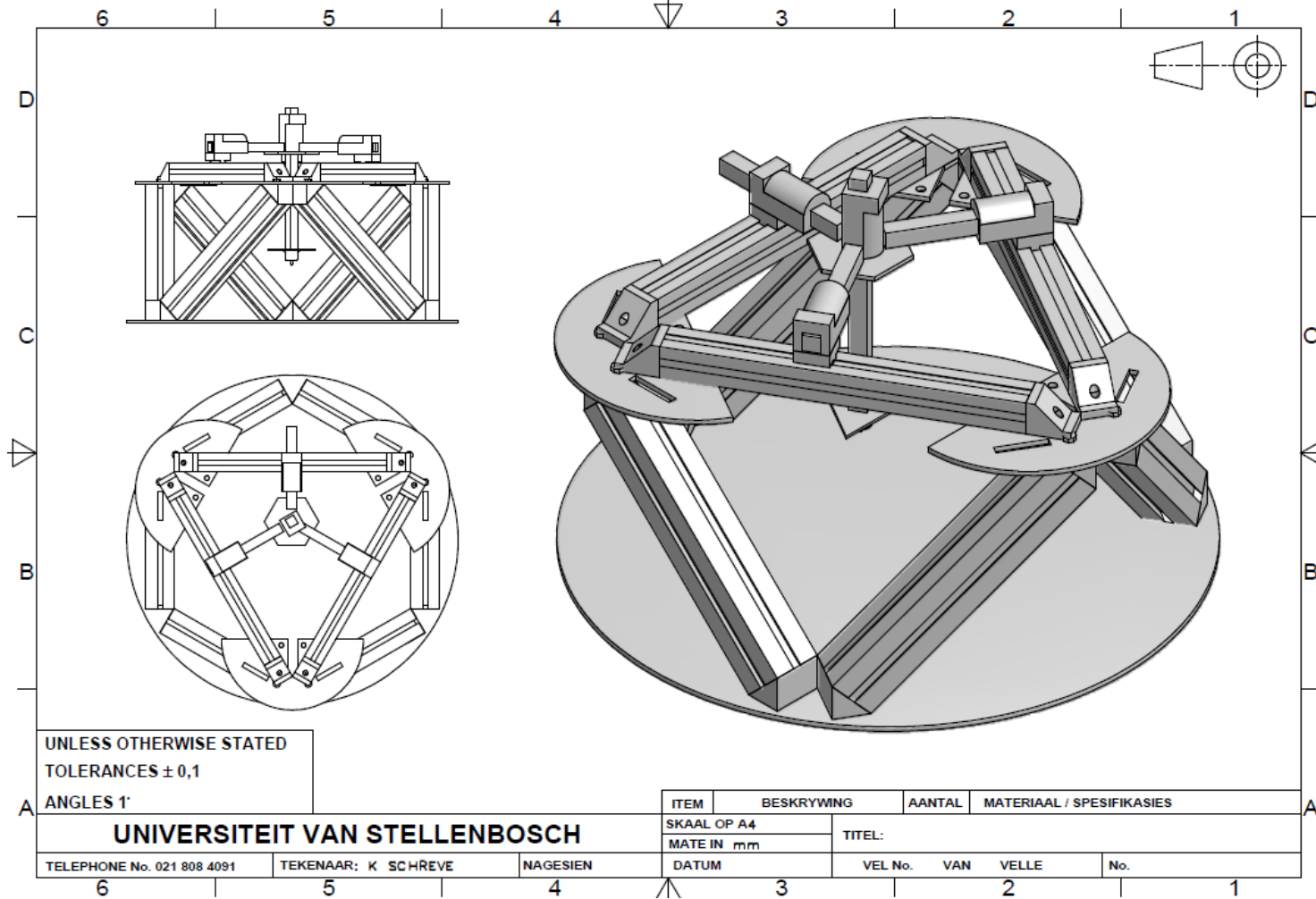
Appendix B: Program code solvers

Appendix B-1: Code for the DPKM solver

```
import sympy
import mpmath
from mpmath import pi, sqrt, sin, cos, tan, acos
from sympy import Matrix, S, Eq, solve
import sys
import scipy

' Direct Kinematic Model DPKM analytical solution'

z1=float(sys.argv[1])
z2=float(sys.argv[2])
z3=float(sys.argv[3])
r1=float(sys.argv[4])
r2=float(sys.argv[5])
r3=float(sys.argv[6])

x1= ((0.0075     *z1 +    148.59  -erx1))
x2= ((0.0082     *z2 +    -253.75 -erx2))
x3= ((0.0069     *z3 +    140.74  -erx3))
y1= (((0.0201    *z1 +    3.3691) -ery1))
y2= ((0.0192     *z2 +    -220.11 -ery2))
y3= ((0.0153     *z3 +    -454.53 -ery3))

x12=x1-x2
y12=y1-y2
x13=x1-x3
y13=y1-y3

l12=(x12**2+y12**2)
l13=(x13**2+y13**2)
r12=(r1**2+r2**2-2*r1*r2*cos(75.5224878140701*pi/180))
r13=(r1**2+r3**2-2*r1*r3*cos(75.5224878140701*pi/180))

c1= r1**2-x1**2-y1**2-z1**2
c2= r2**2-x2**2-y2**2-z2**2
c3= r3**2-x3**2-y3**2-z3**2
c21=c2-c1
c31=c3-c1

A=((c21/(2*z2))-(c31/(2*z3)))/(x12/z2-x13/z3)
B=(y12/z2-y13/z3)/(x12/z2-x13/z3)
D=(y12/z2)-B*(x12/z2)
F=A*(x12/z2) - c21/(2*z2)

k= 1 + B**2 + D**2
l= 2*D*F + 2*x1*B - 2*A*B - 2*y1
```

144

```
m= A**2 + F**2 - 2*x1*A - c1

Y1= (-l +sqrt(l**2-4*k*m))/(2*k)
Y2= (-l -sqrt(l**2-4*k*m))/(2*k)

X1= A - B*Y1
X2= A - B*Y2
Z1= F + D*Y1
Z2= F + D*Y2

print ("1st point x,y,z"), X1,Y1,Z1
print ("2nd point x,y,z"), X2,Y2,Z2
```

Appendix B-2: Code for the IPKM solver

```
import sympy
import mpmath
from mpmath import pi, sqrt, sin, cos, tan, acos
from sympy import Matrix, S, Eq, solve
import sys
import scipy
from scipy import optimize
from scipy.optimize import fsolve

'Inverse kinematic solver'

z1=float(sys.argv[1])
z2=float(sys.argv[2])
z3=float(sys.argv[3])

r1=float(sys.argv[4])
r2=float(sys.argv[5])
r3=float(sys.argv[6])

x1= ((0.0075      *z1 +    148.59  -erx1))
x2= ((0.0082      *z2 +   -253.75 -erx2))
x3= ((0.0069      *z3 +    140.74  -erx3))
y1= (((0.0201     *z1 +    3.3691) -ery1))
y2= ((0.0192      *z2 +   -220.11 -ery2))
y3= ((0.0153      *z3 +   -454.53 -ery3))

def funcC(xyz):
    out =    [((x1-xyz[0])**2+(y1-xyz[1])**2+(z1-xyz[2])**2)-r1**2]
    out.append(((x2-xyz[0])**2+(y2-xyz[1])**2+(z2-xyz[2])**2)-r2**2)
    out.append(((x3-xyz[0])**2+(y3-xyz[1])**2+(z3-xyz[2])**2)-r3**2)
    return out
P = scipy.optimize.fsolve(funcC, [40,40,40])

print str("%3.3f"%P[0]).zfill(7), str("%3.3f"%P[1]).zfill(7), str("%3.3f"%P[2]).zfill(7)
```

146

Appendix B-3: Code for the workspace

```
from mpl_toolkits.mplot3d import Axes3D
from matplotlib import cm
from matplotlib.ticker import LinearLocator, FixedLocator, FormatStrFormatter
import matplotlib.pyplot as plt
import numpy as np

' Workspace calculation'

y1= 0
y2= 250
y3= -250
di=y2*tan(60*pi/180)
x1=di*2/3
x2=-(x1/2)+1
x3=-x1/2


lmin = 350.0
lmax = 550.0
fig = plt.figure()
ax = fig.gca(projection='3d')
from enthought.mayavi import mlab
x=[]
y=[]
z=[]
s=[]
size=10
Xmin=-100
Xmax=288
#Ymin=-200
dx=dy=dz=4
Zin=100000.0
Zax=0.0
Yax=0.0
Yx=Xx=Zx=0.0
Yn=Xn=Zn=10000
for X in range (Xmin, Xmax, dx):
   Ymax=int((Rp1-X)*np.tan(30*np.pi/180.0))
   Ymin=int(-Ymax)
   for Y in range (Ymin, Ymax, dy):
      Zmin = (lmin**2-(X-x1)**2-(Y-y1)**2)**0.5
      if Zmin>0.0:
         l1 = ((X-x1)**2+(Y-y1)**2+Zmin**2)**0.5
         l2 = ((X-x2)**2+(Y-y2)**2+Zmin**2)**0.5
         l3 = ((X-x3)**2+(Y-y3)**2+Zmin**2)**0.5
         #print l1,l2,l3
         if l1<lmin or l2<lmin or l3<lmin or l1>lmax or l2>lmax or l3>lmax:
            p=0#print 'l1,l2,l3'
         else:
            if Y>Yx: Yx=Y
            if Y<Yx: Yn=Y
```

147

```
    if X>Xx: Xx=X
    if X<Xn: Xn=X
    if Zmin>Zx: Zx=Zmin
    if Zmin<Zn: Zn=Zmin
    Z = Zmin
    x.append(X)
    y.append(Y)
    z.append(Z)
    s.append(size)
if Zmin<Zin: Zin=Zmin
Zmin = (lmin**2-(X-x2)**2-(Y-y2)**2)**0.5
if Zmin>0.0:
  l1 = ((X-x1)**2+(Y-y1)**2+Zmin**2)**0.5
  l2 = ((X-x2)**2+(Y-y2)**2+Zmin**2)**0.5
  l3 = ((X-x3)**2+(Y-y3)**2+Zmin**2)**0.5
  if l1<lmin or l2<lmin or l3<lmin or l1>lmax or l2>lmax or l3>lmax:
    p=0
  else:
    if Y>Yx: Yx=Y
    if Y<Yx: Yn=Y
    if X>Xx: Xx=X
    if X<Xn: Xn=X
    if Zmin>Zx: Zx=Zmin
    if Zmin<Zn: Zn=Zmin
    Z = Zmin
    x.append(X)
    y.append(Y)
    z.append(Z)
    s.append(size)
if Zmin<Zin: Zin=Zmin
Zmin = (lmin**2-(X-x3)**2-(Y-y3)**2)**0.5
if Zmin>0.0:
  l1 = ((X-x1)**2+(Y-y1)**2+Zmin**2)**0.5
  l2 = ((X-x2)**2+(Y-y2)**2+Zmin**2)**0.5
  l3 = ((X-x3)**2+(Y-y3)**2+Zmin**2)**0.5
  if l1<lmin or l2<lmin or l3<lmin or l1>lmax or l2>lmax or l3>lmax:
    p=0
  else:
    if Y>Yx: Yx=Y
    if Y<Yx: Yn=Y
    if X>Xx: Xx=X
    if X<Xn: Xn=X
    if Zmin>Zx: Zx=Zmin
    if Zmin<Zn: Zn=Zmin
    #print l1,l2,l3
    Z = Zmin
    x.append(X)
    y.append(Y)
    z.append(Z)
    s.append(size)
if Zmin<Zin: Zin=Zmin
Zmax = (lmax**2-(X-x1)**2-(Y-y1)**2)**0.5
if Zmax > 0.0:
```

```
    l1 = ((X-x1)**2+(Y-y1)**2+Zmax**2)**0.5
    l2 = ((X-x2)**2+(Y-y2)**2+Zmax**2)**0.5
    l3 = ((X-x3)**2+(Y-y3)**2+Zmax**2)**0.5
    if l1>lmax or l2>lmax or l3>lmax or l1<lmin or l2<lmin or l3<lmin:
        p=0
    else:
        if Y>Yx: Yx=Y
        if Y<Yx: Yn=Y
        if X>Xx: Xx=X
        if X<Xn: Xn=X
        if Zmax>Zx: Zx=Zmax
        if Zmax<Zn: Zn=Zmax
        Z = Zmax
        x.append(X)
        y.append(Y)
        z.append(Z)
        s.append(size)
if Zmax>Zax: Zax=Zmax
Zmax = (lmax**2-(X-x2)**2-(Y-y2)**2)**0.5
if Zmax > 0.0:
    l1 = ((X-x1)**2+(Y-y1)**2+Zmax**2)**0.5
    l2 = ((X-x2)**2+(Y-y2)**2+Zmax**2)**0.5
    l3 = ((X-x3)**2+(Y-y3)**2+Zmax**2)**0.5
    if l1>lmax or l2>lmax or l3>lmax or l1<lmin or l2<lmin or l3<lmin:
        p=0
    else:
        if Y>Yx: Yx=Y
        if Y<Yx: Yn=Y
        if X>Xx: Xx=X
        if X<Xn: Xn=X
        if Zmax>Zx: Zx=Zmax
        if Zmax<Zn: Zn=Zmax
        Z = Zmax
        x.append(X)
        y.append(Y)
        z.append(Z)
        s.append(size)
if Zmax>Zax: Zax=Zmax
Zmax = (lmax**2-(X-x3)**2-(Y-y3)**2)**0.5
if Zmax > 0.0:
    l1 = ((X-x1)**2+(Y-y1)**2+Zmax**2)**0.5
    l2 = ((X-x2)**2+(Y-y2)**2+Zmax**2)**0.5
    l3 = ((X-x3)**2+(Y-y3)**2+Zmax**2)**0.5
    if l1>lmax or l2>lmax or l3>lmax or l1<lmin or l2<lmin or l3<lmin:
        p=0
    else:
        if Y>Yx: Yx=Y
        if Y<Yx: Yn=Y
        if X>Xx: Xx=X
        if X<Xn: Xn=X
        if Zmax>Zx: Zx=Zmax
        if Zmax<Zn: Zn=Zmax
        Z = Zmax
```

```
        x.append(X)
        y.append(Y)
        z.append(Z)
        s.append(size)
    if Zmax>Zax: Zax=Zmax
  for k in range (0,450,dz):
    l1 = ((X-x1)**2+(Ymax-y1)**2+k**2)**0.5
    l2 = ((X-x2)**2+(Ymax-y2)**2+k**2)**0.5
    l3 = ((X-x3)**2+(Ymax-y3)**2+k**2)**0.5
    if l1>lmax or l2>lmax or l3>lmax or l1<lmin or l2<lmin or l3<lmin:
      p=0
    else:
      if Y>Yx: Yx=Y
      if Y<Yx: Yn=Y
      if X>Xx: Xx=X
      if X<Xn: Xn=X
      if Zmax>Zx: Zx=Zmax
      if Zmax<Zn: Zn=Zmax
      #print l1,l2,l3
      Z = k
      x.append(X)
      y.append(Ymax)
      z.append(Z)
      s.append(size)
    l1 = ((X-x1)**2+(Ymin-y1)**2+k**2)**0.5
    l2 = ((X-x2)**2+(Ymin-y2)**2+k**2)**0.5
    l3 = ((X-x3)**2+(Ymin-y3)**2+k**2)**0.5
    if l1>lmax or l2>lmax or l3>lmax or l1<lmin or l2<lmin or l3<lmin:
      p=0
    else:
      if Y>Yx: Yx=Y
      if Y<Yx: Yn=Y
      if X>Xx: Xx=X
      if X<Xn: Xn=X
      if Zmax>Zx: Zx=Zmax
      if Zmax<Zn: Zn=Zmax
      Z = k
      x.append(X)
      y.append(Ymin)
      z.append(Z)
      s.append(size)
xb=[]
yb=[]
zb=[]
sb=[]
ZU=325
ZL=426
XL=-50
XU=50
YL=-50
YU=50
d=2
for X in range (-50, 51, d):
```

```
    for Y in range (-50, 51, d):
        xb.append(X)
        yb.append(Y)
        zb.append(ZU)
        sb.append(size)
        xb.append(X)
        yb.append(Y)
        zb.append(ZL)
        sb.append(size)
for X in range (-50, XU, d):
    for Z in range (ZU, ZL, d):
        xb.append(X)
        yb.append(YU)
        zb.append(Z)
        sb.append(size)
        xb.append(X)
        yb.append(YL)
        zb.append(Z)
        sb.append(size)
for Z in range (ZU, ZL, d):
    for Y in range (-50, 51, d):
        xb.append(XU)
        yb.append(Y)
        zb.append(Z)
        sb.append(size)
        xb.append(XL)
        yb.append(Y)
        zb.append(Z)
        sb.append(size)
print Xmin, Xmax, Zmin, Zmax
print Zin,Zax
print Xn,Xx,Yx,Zn,Zx
S = mlab.points3d(x,y,z,s, line_width=1.0, colormap='Greys', scale_factor=.25)
S = mlab.points3d(xb,yb,zb,sb, line_width=1.0, colormap='RdBu', scale_factor=.25)

mlab.show()
print 'done'
```

151

Appendix B-4: Code for the analytical error model solver

```
import numpy as np
import scipy as sp
import mpmath
from mpmath import pi, sqrt, sin, cos, tan, acos
import sympy as S
from numpy import array
from sympy import simplify
import sys
from sympy import re, im
from numpy import *

' Analytical Error Model'

cost1,cost2,cost3,X,Y,Z,x1,x2,x3,y1,y2,y3,z1,z2,z3,r1,r2,r3,z1n=
S.symbols("cost1,cost2,cost3,X,Y,Z,x1,x2,x3,y1,y2,y3,z1,z2,z3,r1,r2,r3,z1n")
Pv = [ x1,x2,x3,y1,y2,y3,z1,z2,z3,r1,r2,r3]#,fi1,fi2,fi3 ]
dx1=dx2=dx3=dy1=dy2=dy3=(0.05/3)**2
dz1=(0.25/3.0)**2
dz2=(0.25/3.0)**2
dz3=(0.25/3.0)**2
dr1=(0.2/3.0)**2
dr2=(0.2/3.0)**2
dr3=(0.2/3.0)**2
ab1a=ab1b=ab2a=ab2b=ab3a=ab3b=0.005
offset=0.015
z1=float(sys.argv[1])
z2=float(sys.argv[2])
z3=float(sys.argv[3])
r1=float(sys.argv[4])
r2=float(sys.argv[5])
r3=float(sys.argv[6])
dr1=dr1+tan(ab1b*pi/180)*offset
dr2=dr2+tan(ab2b*pi/180)*offset
dr3=dr3+tan(ab3b*pi/180)*offset
dSD = [ dx1,dx2,dx3,dy1,dy2,dy3,dz1,dz2,dz3,dr1,dr2,dr3 ]
r12=(r1**2+r2**2-2*r1*r2*cost1)
r13=(r1**2+r3**2-2*r1*r3*cost3)
r23=(r2**2+r3**2-2*r2*r3*cost2)
c1= r1**2-x1**2-y1**2-z1**2
c2= r2**2-x2**2-y2**2-z2**2
c3= r3**2-x3**2-y3**2-z3**2
c21=c2-c1
c31=c3-c1
x12=((x1-x2)); y12=((y1-y2))
x23=((x2-x3)); y23=((y2-y3))
x13=((x1-x3)); y13=((y1-y3))
l12=((x12**2+y12**2))#'distance at zero'
l23=((x23**2+y23**2))
l13=((x13**2+y13**2))
```

```
A=((c21/(2*z2))-(c31/(2*z3)))/(x12/z2-x13/z3)
B=(y12/z2-y13/z3)/(x12/z2-x13/z3)
D=(y12/z2)-B*(x12/z2)
F=A*(x12/z2) - c21/(2*z2)

k= 1 + B**2 + D**2
l= 2*D*F + 2* x1 *B - 2*A*B - 2* y1
m= A**2 + F**2 - 2* x1 *A - c1

Y1= (-l +(abs(l**2-4*k*m))**0.5)/(2*k)
Y2= (-l -(abs(l**2-4*k*m))**0.5)/(2*k)

X1= A - B*Y1
X2= A - B*Y2
Z1= (F + D*Y1)#+z1n
Z2= (F + D*Y2)#+z1n

X=X2;Y=Y2;Z=Z2+z1n
cost1= cos(bita1*pi/180)
cost3= cos(bita3*pi/180)
erx1=-0.160; erx2=-0.125; erx3=0.271
ery1=0.0951; ery2=-0.059; ery3=0.0315###
lv12=(abs(r12))**0.5
ga2=-253.750-erx2
gb2=-220.110-ery2
ec12=x1-ga2
ec22=y1-gb2
ea2=0.008**2+0.019**2+1
eb2=-((2*ec12*0.008+2*ec22*0.019+2*z1))
ec2=z1**2+ec12**2+ec22**2-lv12**2
z2a=(-eb2+(abs(eb2**2-4*ea2*ec2))**0.5)/(2*ea2)
z2b=(-eb2-(abs(eb2**2-4*ea2*ec2))**0.5)/(2*ea2)

lv13=(abs(r13))**0.5
ga3=140.740#-erx3
gb3=-454.53#0-ery3
ec13=x1-ga3
ec23=y1-gb3
ea3=0.0069**2+0.0153**2+1
eb3=-(2*ec13*0.007+2*ec23*0.015+2*z1)
ec3=z1**2+ec13**2+ec23**2-lv13**2
z3a=(-eb3+(abs(eb3**2-4*ea3*ec3))**0.5)/(2*ea3)
z3b=(-eb3-(abs(eb3**2-4*ea3*ec3))**0.5)/(2*ea3)
z2=eval(repr(z2b));z3=eval(repr(z3b))
if pz2==-1: z2=eval(repr(z2a))
if pz3==-1: z3=eval(repr(z3a))
x1= ((0.0075      *z1 +     148.59  -erx1))
x2= ((0.0082      *z2 +     -253.75 -erx2))
x3= ((0.0069      *z3 +     140.74  -erx3))
y1= (((0.0201     *z1 +     3.3691) -ery1))
y2= ((0.0192      *z2 +     -220.11 -ery2))
y3= ((0.0153      *z3 +     -454.53 -ery3))
z2=((z2-z1))
```

153

```
z3=((z3-z1))
z1n=z1
z1=0.0
x12=((x1-x2)); y12=((y1-y2))
x23=((x2-x3)); y23=((y2-y3))
x13=((x1-x3)); y13=((y1-y3))
l12=((x12**2+y12**2))
l23=((x23**2+y23**2))
l13=((x13**2+y13**2))
DX=0.0
DY=0.0
DZ=0.0
dYP= []
dXP= []
dZP= []
SDP = np.zeros((12,12))
J = np.zeros((3,12))
for i in range(0,12):
J[1,i]=eval(repr(S.diff(Y,Pv[i])))
J[0,i]=eval(repr(S.diff(X,Pv[i])))
J[2,i]=eval(repr(S.diff(Z,Pv[i])))
SDP[i,i]= dSD[i]#(0.050/3.0)**2
JT=J.T
JT=np.mat(JT)
J=np.mat(J)
SDP=np.mat(SDP)
COV=J*SDP*JT
print 'SD x,y,z', '%.6f'% sqrt(COV[0,0]),'%.6f'% (sqrt(COV[1,1])),'%.6f'% sqrt(COV[2,2])

for i in range(0,12):
    DY= DY + dSD[i]*J[1,i]#((dYP[i]))
    DX= DX + dSD[i]*J[0,i]#((dXP[i])))
    DZ= DZ + dSD[i]*J[2,i]#((dZP[i])))
print 'Y=','%.3f' %eval(repr(Y))#,eval(repr(Y1)),eval(repr(Y2))
print 'X=','%.3f' %eval(repr(X))#,eval(repr(X1)),eval(repr(X2))
print 'Z=','%.3f' %eval(repr(Z))#,eval(repr(Z1)),eval(repr(Z2))
print '%.6f' %DX,'%.6f' %DY,'%.6f' %DZ

print ("done")
```

Appendix B-5: Code for the Monte-Carlo simulation

```
import sympy
import mpmath
import numpy as np
from mpmath import pi, sqrt, sin, cos, tan, acos
from sympy import Matrix, S, Eq, solve
import sys
import scipy
import matplotlib
matplotlib.use('TkAgg') # do this before importing pylab
import matplotlib.mlab as mlab
import matplotlib.pyplot as plt

 'Monte-Carlo simulation'

 bita1=68.737; bita2=68.564; bita3=68.616
 cost1= cos(bita1*pi/180)
 cost2= cos(bita2*pi/180)
 cost3= cos(bita3*pi/180)

 r12=(r1**2+r2**2-2*r1*r2*cost1)
 r13=(r1**2+r3**2-2*r1*r3*cost3)
 r23=(r2**2+r3**2-2*r2*r3*cost2)

 x1= 0.0075     *z1 +     148.59
 x2= 0.0082     *z2 +     -253.75
 x3= 0.0069     *z3 +     140.74
 y1= 0.0201     *z1 +     3.3691
 y2= 0.0192     *z2 +     -220.11
 y3= 0.0153     *z3 +     -454.53

 x12=x1-x2; y12=y1-y2
 x23=x2-x3; y23=y2-y3
 x13=x1-x3; y13=y1-y3

 lv12=(abs(r12))**0.5
 ga2=-253.750-erx2
 gb2=-220.110-ery2
 ec12=x1-ga2
 ec22=y1-gb2
 ea2=0.008**2+0.019**2+1
 eb2=-((2*ec12*0.008+2*ec22*0.019+2*z1))
 ec2=z1**2+ec12**2+ec22**2-lv12**2
 z2a=(-eb2+(abs(eb2**2-4*ea2*ec2))**0.5)/(2*ea2)
 z2b=(-eb2-(abs(eb2**2-4*ea2*ec2))**0.5)/(2*ea2)

 lv13=(abs(r13))**0.5
 ga3=140.740-erx3
 gb3=-454.530-ery3
 ec13=x1-ga3
 ec23=y1-gb3
```

155

```
ea3=0.007**2+0.015**2+1
eb3=-(2*ec13*0.007+2*ec23*0.015+2*z1)
ec3=z1**2+ec13**2+ec23**2-lv13**2
z3a=(-eb3+(abs(eb3**2-4*ea3*ec3))**0.5)/(2*ea3)
z3b=(-eb3-(abs(eb3**2-4*ea3*ec3))**0.5)/(2*ea3)

z2=((z2a));z3=((z3a))
if p>1: z2=((z2b))
if p>3: z3=((z3b))

z1n=z1
z2=z2-z1
z3=z3-z1
z1=0

c1= r1**2-x1**2-y1**2-z1**2
c2= r2**2-x2**2-y2**2-z2**2
c3= r3**2-x3**2-y3**2-z3**2
c21=c2-c1
c31=c3-c1
A=((c21/(2*z2))-(c31/(2*z3)))/(x12/z2-x13/z3)
B=(y12/z2-y13/z3)/(x12/z2-x13/z3)
D=(y12/z2)-B*(x12/z2)
F=A*(x12/z2) - c21/(2*z2)

k= 1 + B**2 + D**2
l= 2*D*F + 2* x1 *B - 2*A*B - 2* y1
m= A**2 + F**2 - 2* x1 *A - c1

Y1= (-l +sqrt(abs(l**2-4*k*m)))/(2*k)
Y2= (-l -sqrt(abs(l**2-4*k*m)))/(2*k)

X1= A - B*Y1
X2= A - B*Y2
Z1= F + D*Y1
Z2= F + D*Y2
X=X2;Y=Y2;Z=Z2+z1n
if p>3: X=X1;Y=Y1;Z=Z1+z1n

print '%.3f'%X,'%.3f'%Y,'%.3f'%(Z)

dx1=dx2=dx3=0.05
dy1=dy2=dy3=0.05
dz1=0.25;   dz2=0.25;   dz3=0.25
dr1=0.15
dr2=0.15
dr3=0.15
ab1a=ab1b=ab2a=ab2b=ab3a=ab3b=0.011
offset=0.005

dr1=dr1+tan(ab1b*pi/180)*offset
dr2=dr2+tan(ab2b*pi/180)*offset
dr3=dr3+tan(ab3b*pi/180)*offset
```

156

```
dr1=dr1+(r1-r1*cos(ab1a*pi/180)*cos(ab1b*pi/180))
dr2=dr2+(r2-r2*cos(ab2a*pi/180)*cos(ab3b*pi/180))
dr3=dr3+(r3-r3*cos(ab3a*pi/180)*cos(ab3b*pi/180))
dfi1=0.0#005/2.0
dfi2=0.0#005/2.0
dfi3=0.0#005/2.0


YP= []
XP= []
ZP= []
Xmin=Xmax=X
Ymin=Ymax=Y
Zmin=Zmax=Z
SmX=0.0
SmY=0.0
SmZ=0.0
N=50000
estimate=Z
count=0
for i in range(0,N):
  ex1=(np.random.random())*(2.0*dx1)+(x1-dx1)
  ex2=(np.random.random())*(2.0*dx2)+(x2-dx2)
  ex3=(np.random.random())*(2.0*dx3)+(x3-dx3)
  ey1=(np.random.random())*(2.0*dy1)+(y1-dy1)
  ey2=(np.random.random())*(2.0*dy2)+(y2-dy2)
  ey3=(np.random.random())*(2.0*dy3)+(y3-dy3)
  er1=(np.random.random())*(2.0*dr1)+(r1-dr1)
  er2=(np.random.random())*(2.0*dr2)+(r2-dr2)
  er3=(np.random.random())*(2.0*dr3)+(r3-dr3)
  ez1=(np.random.random())*(2.0*dz1)+(z1-dz1)
  ez2=(np.random.random())*(2.0*dz2)+(z2-dz2)
  ez3=(np.random.random())*(2.0*dz3)+(z3-dz3)

  ec1= er1**2-ex1**2-ey1**2-ez1**2
  ec2= er2**2-ex2**2-ey2**2-ez2**2
  ec3= er3**2-ex3**2-ey3**2-ez3**2
  ec21=ec2-ec1
  ec31=ec3-ec1

  x12=ex1-ex2
  y12=ey1-ey2
  x13=ex1-ex3
  y13=ey1-ey3

  A= ((ec21/(2*ez2))-(ec31/(2*ez3)))/((x12/ez2-x13/ez3))
  B= (y12/ez2-y13/ez3)/((x12/ez2-x13/ez3))
  D= (y12/ez2)-B*(x12/ez2)
  F= A*(x12/ez2) - ec21/(2*ez2)

  k= 1 + B**2 + D**2
  l= 2*D*F + 2*ex1*B - 2*A*B - 2*ey1
  m= A**2 + F**2 - 2*ex1*A - ec1
```

157

```
   Y1= (-l +sqrt(abs(l**2-4*k*m)))/(2*k)
   Y2= (-l -sqrt(abs(l**2-4*k*m)))/(2*k)

   X1= A - B*Y1
   X2= A - B*Y2
   Z1= F + D*Y1
   Z2= F + D*Y2
   X=X2;Y=Y2;Z=Z2+z1n
   if p>3: X=X1;Y=Y1;Z=Z1+z1n
   if abs(Z)>(abs(estimate) +3) or abs(Z)<(abs(estimate) -3):
      print 'wrong'
   else:
      XP.append(X)
      YP.append(Y)
      ZP.append(Z)
      count=count+1
      if X<Xmin:Xmin=X
      if Y<Ymin:Ymin=Y
      if Z<Zmin:Zmin=Z
      if X>Xmax:Xmax=X
      if Y>Ymax:Ymax=Y
      if Z>Zmax:Zmax=Z
      SmX=SmX+X
      SmY=SmY+Y
      SmZ=SmZ+Z
MX= np.median(XP)
MY= np.median(YP)
MZ= np.median(ZP)

XSD= np.std(XP)
YSD= np.std(YP)
ZSD= np.std(ZP)
Xvr= np.var(XP)
Yvr= np.var(YP)
Zvr= np.var(ZP)

avX=SmX/count
avY=SmY/count
avZ=SmZ/count

sumx=0
sumy=0
sumz=0
for i in range(0,count):
   sumx=sumx+(XP[i]-avX)**2
   sumy=sumy+(YP[i]-avY)**2
   sumz=sumz+(ZP[i]-avZ)**2

sdX=(sumx/(count-1))**0.5
sdY=(sumy/(count-1))**0.5
sdZ=(sumz/(count-1))**0.5
```

158

```
print '%.3f'%X,'%.3f'%Y,'%.3f'%Z
print 'Standard deviations of X=','%.6f' %XSD,'   Y=','%.6f' %YSD,'   Z=','%.6f' %ZSD
#print 'variances X,Y,Z',Xvr,Yvr,Zvr

print 'min X,Y,Z', '%.3f' %Xmin,'%.3f' %Ymin,'%.3f' %Zmin
print 'max X,Y,Z', '%.3f' %Xmax,'%.3f' %Ymax,'%.3f' %Zmax
errorX=Xmax-Xmin
errorY=Ymax-Ymin
errorZ=Zmax-Zmin
print 'error value max-min', '%.3f' %(errorX/2),'%.3f' %(errorY/2),'%.3f' %(errorZ/2)

print MX,'Standard deviations of X=',XSD,'   Y=',YSD,'   Z=',YSD

matplotlib.pyplot.hist(YP, bins=50, facecolor='green')
plt.xlabel('Y-direction (mm)')
plt.ylabel('Probability')
plt.axis([Ymin, Ymax, 0, 0.03])
plt.show()

print ("done")
```

159

Appendix C: Measurements data and calculations

Table C-1: Dead distance calculation

	Point no.									
	1	2	3	4	5	6	7	8	9	10
l_a	329.341	328.815	328.544	329.751	329.636	329.650	329.626	329.504	328.247	328.334
l_b	326.345	321.724	321.926	323.827	323.569	324.003	325.917	327.787	324.870	323.749
l_c	324.235	324.403	324.620	324.093	324.137	324.320	324.374	324.338	326.411	326.021
r_a	35.408	34.853	34.657	35.622	35.552	35.550	35.551	35.553	34.154	34.300
r_b	36.443	31.847	32.014	34.111	33.513	34.217	35.906	37.947	34.908	33.812
r_c	34.801	35.104	35.389	34.758	34.740	34.866	34.903	34.856	36.991	36.600
d_a	293.940	293.962	293.890	294.131	294.081	294.095	294.071	293.949	294.089	294.027
d_b	289.904	289.884	289.916	289.717	290.059	289.793	290.016	289.845	289.965	289.939
d_c	289.430	289.299	289.237	289.339	289.397	289.460	289.471	289.485	289.416	289.421

Measurements in (mm)

Table C-2: Confirmation of micro-CMM measurements

No.	CMM			micro-CMM			ε-CMM
	x	*y*	*z*	*x*	*y*	*z*	
1	14.982	-5.846	79.743	14.192	-5.627	80.298	-0.387
2	29.992	-4.256	73.423	29.769	-4.027	73.719	-0.178
3	48.318	-2.358	67.148	48.309	-2.116	67.36	-0.160
4	27.666	-44.101	40.761	27.608	-44.124	40.824	-0.029
5	31.588	-41.857	39.366	31.543	-41.88	39.422	-0.026
6	-13.537	-7.822	93.342	-11.668	-7.631	92.564	1.034
7	-48.378	-69.651	87.032	-47.323	-69.815	86.391	0.781
8	-29.866	-13.266	41.018	-29.172	-13.314	40.667	0.655
9	-40.152	-14.874	47.561	-39.606	-14.925	47.277	0.541
10	-50.786	-17.03	55.258	-50.331	-17.085	55.013	0.463
11	-56.509	6.368	45.642	-56.09	6.406	45.476	0.425
12	-3.557	20.509	68.49	-2.658	19.972	67.655	0.991
13	-20.272	20.899	77.416	-19.931	20.349	76.835	0.765
14	-26.03	20.951	80.788	-25.769	20.401	80.247	0.708
15	-4.325	10.592	76.864	-2.279	11.115	76.301	0.570
16	-16.812	10.256	83.423	-15.62	10.745	83.223	0.360
17	-23.242	10.039	87.187	-22.21	10.515	87.047	0.339
18	-31.225	68.995	54.807	-30.918	68.88	54.563	0.330
19	-40.019	72.76	61.691	-39.743	72.643	61.454	0.330
20	-48.061	74.359	67.496	-47.806	74.239	67.263	0.331
21	-49.055	74.486	68.211	-48.802	74.366	67.979	0.330
22	-47.942	7.343	39.329	-47.469	7.426	39.173	0.451
23	8.043	21.7	63.267	8.389	21.135	62.715	0.656
24	17.328	21.606	59.264	14.687	20.93	59.976	0.217
25	12.461	11.092	69.158	10.496	11.546	70.468	-1.032
26	-4.768	63.059	38.875	-4.309	62.959	38.589	0.262
27	-16.908	65.49	45.617	-16.536	65.382	45.356	0.308
28	23.859	11.474	64.405	23.335	11.957	65.046	-0.497
29	16.458	-23.57	55.239	17.099	-24.808	55.152	-0.264
30	64.864	18.69	89.578	64.355	18.669	89.725	0.155

Measurements in (mm)

Table C-3: Error estimation and comparison

No.	ε-CMM	ε-MC 3.σ	ε-AM 3.σ
1	0.387	0.718	0.729
2	0.178	0.717	0.725
3	0.160	0.719	0.719
4	0.029	0.703	0.702
5	0.026	0.703	0.702
6	1.034	0.726	0.735
7	0.781	0.709	0.713
8	0.655	0.74	0.738
9	0.541	0.727	0.739
10	0.463	0.737	0.74
11	0.425	0.753	0.749
12	0.991	0.736	0.743
13	0.765	0.745	0.747
14	0.708	0.738	0.748
15	0.570	0.745	0.741
16	0.360	0.738	0.743
17	0.339	0.744	0.745
18	0.330	0.757	0.762
19	0.330	0.756	0.763
20	0.331	0.767	0.764
21	0.330	0.761	0.764
22	0.451	0.743	0.748
23	0.656	0.742	0.74
24	0.217	0.741	0.739
25	1.032	0.728	0.738
26	0.262	0.758	0.757
27	0.308	0.76	0.76
28	0.497	0.733	0.734
29	0.264	0.737	0.740
30	0.155	0.740	0.748

Measurements in (mm)

Appendix D: Instruments specifications and data sheets

Includes the specifications and drawings of:

D-1: TP8 manual indexable probe

D-2: T-LSR300A Linear motor

D-3: OptoNCDT 1302 Laser distance sensor

D-4: FNS Runner block

D-5: SNS Ball guide rail

D-6: SRJ Spherical joints

D-1: TP8 manual indexable probe
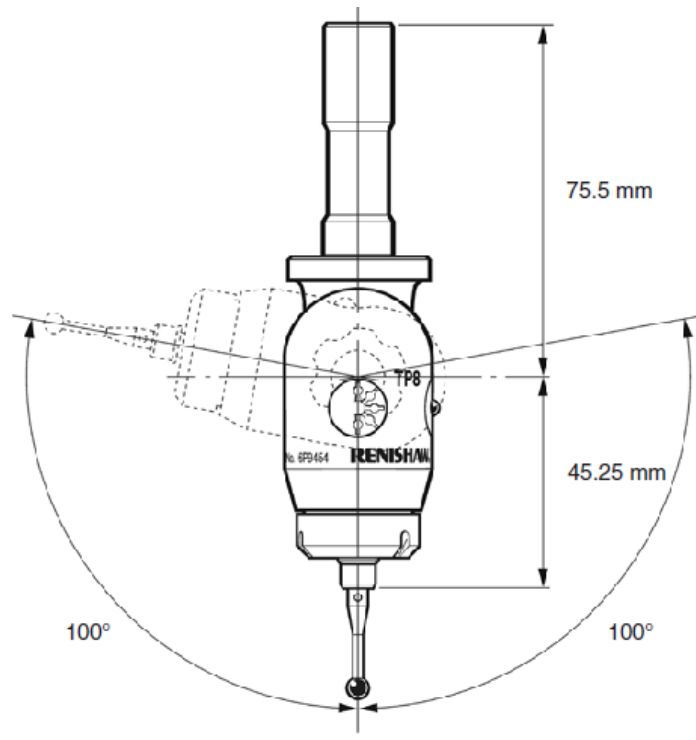
Specification summary	TP8
Principal application	Robust universal DCC and manual CMMs.
Sense directions	5-axis: ±X, ±Y, +Z
Unidirectional repeatability maximum (2s μm) (at stylus tip)	0.5 μm (0.00002 in)
Pre-travel variation 360° (xy plane)	±1 μm (±0.00004 in)
Weight (without shank)	95 g (3.36 oz)
Stylus range	M3
Stylus force range (adjustable)	0.11 N - 0.3 N
Stylus force (set by renishaw)	0.11 N - 0.13 N
Stylus overtravel xy plane (typical) +z axis	±22° 5.5 mm (0.22 in) @ 0.11 N 2 mm (0.08 in) @ 0.3 N
Mounting method	Shank
Suitable interface	PI 4-2, PI 7-2, PI 200, UCC

Above data applies to test conditions as follows: Stylus length 21 mm (0.83 in).

Stylus velocity 480 mm/min (1.57 ft/min). Stylus force 0.11-0.13 N. Ø4 ball.

D-2: T-LSR300A Motorized Linear Slide, 300 mm travel, RS-232 plus manual control

Specification	Value	Alternate Unit
Microstep Size (Default Resolution)	0.09921875 µm	
Integrated Controller	Yes	
Travel Range	300 mm	11.811 "
Accuracy (unidirectional)	90 µm	0.003543 "
Repeatability	< 2.5 µm	< 0.000098 "
Backlash	< 5 µm	< 0.000197 "
Maximum Speed	4 mm/s	0.157 "/s
Minimum Speed	0.00093 mm/s	0.00004 "/s
Speed Resolution	0.00093 mm/s	0.00004 "/s
Encoder Type	None	
Peak Thrust	300 N	67.3 lb
Maximum Continuous Thrust	100 N	22.4 lb
Communication Interface	RS-232	
Communication Protocol	Zaber Binary	
Maximum Centered Load	200 N	44.9 lb
Maximum Cantilever Load	800 N-cm	1,132.9 oz-in
Guide Type	Roller bearing	
Vertical Runout	< 13 µm	< 0.000512 "
Horizontal Runout	< 13 µm	< 0.000512 "
Pitch	0.05 degrees	0.873 mrad
Roll	0.01 degrees	0.175 mrad
Yaw	0.02 degrees	0.349 mrad
Power Supply	12-16 VDC	
Power Plug	2.1 mm center positive	
Linear Motion Per Motor Rev	1.27 mm	0.050 "
Motor Steps Per Rev	200	
Motor Type	Stepper (2 phase)	
Inductance	28 mH	
Default Resolution	1/64 of a step	
Data Cable Connection	Minidin 6 M/F	
Mechanical Drive System	Precision leadscrew	
Limit or Home Sensing	Magnetic home sensor	
Manual Control	Knob with center detent	
Axes of Motion	1	
Mounting Interface	M6 threaded holes and 8-32 threaded holes	
Vacuum Compatible	No	
Compatible Products	T-LS Motorized Stages, TSB Manual Translation Stages	
Operating Temperature Range	0 to 50 degrees C	
Stage Parallelism	< 100 µm	< 0.003937 "
RoHS Compliant	Yes	
CE Compliant	Yes	
Weight	1.80 kg	

165

Specification Charts and Notes

Thrust is a function of speed. The values given are maximums. These values cannot both be achieved simultaneously (i.e. at maximum speed, the unit will not produce maximum thrust). See chart below.

166

16X #8-32 UNC ⌄7
1/2" Spacing

16X M6X1.0 ⌄7
12.5 Spacing

Mounting Slots for M6 or 1/4"-20 Screws

41.8

25

2.5 at Home

13.5

20

65

50

6

31.5 on T-LSR075
44 on All Other Models

Mounting Holes for M6 or 1/4"-20 Screws
Access from Inside for Vertical Mounting

LEDs

Power In
12-16 Vdc
2.1 mm Centre Positive

7.3

64

35.8 to Top
of Carriage

45.3

15.6

14

Data Cables

6

25

65

99

12

Travel + 201
276 This Model
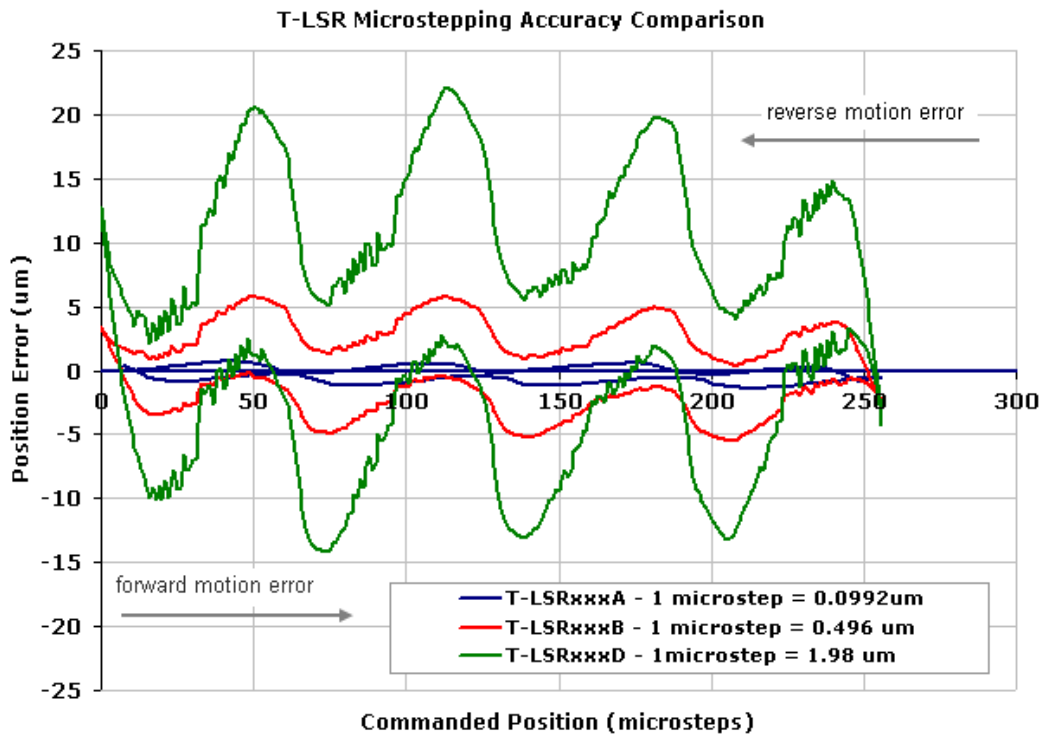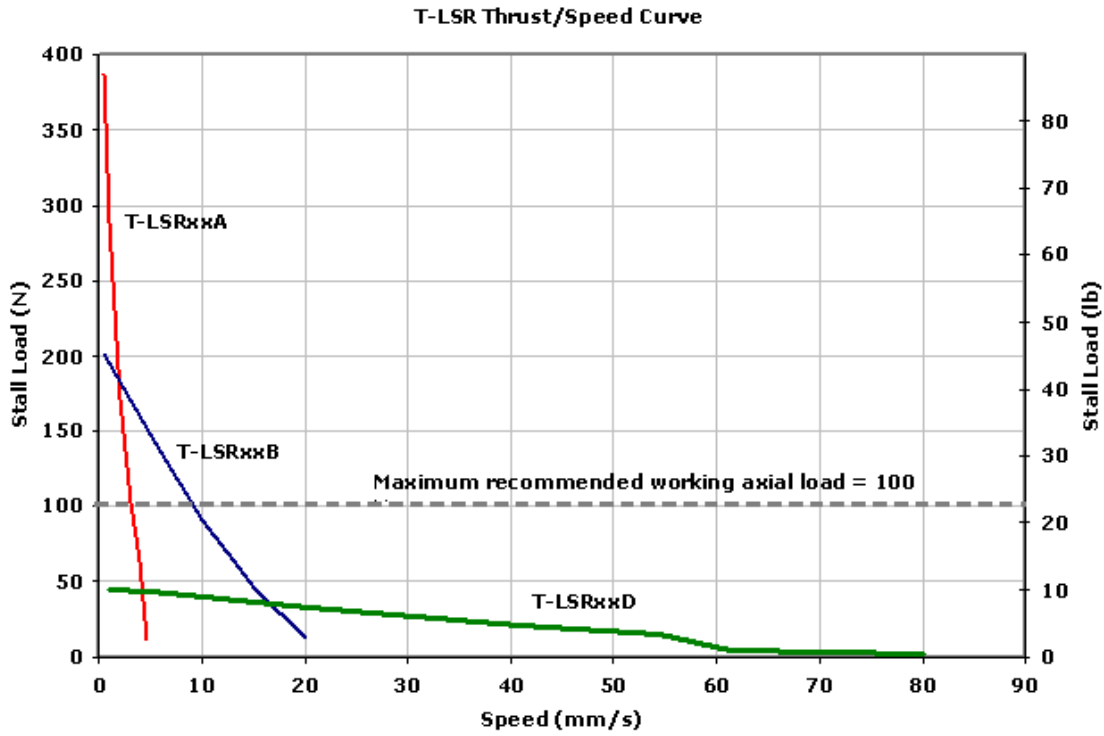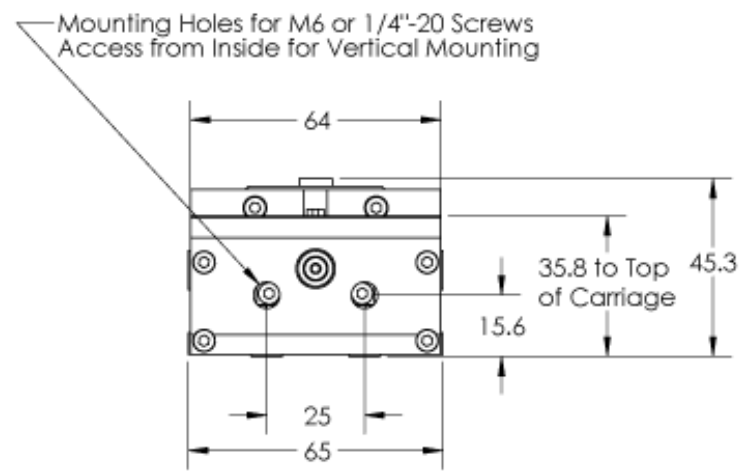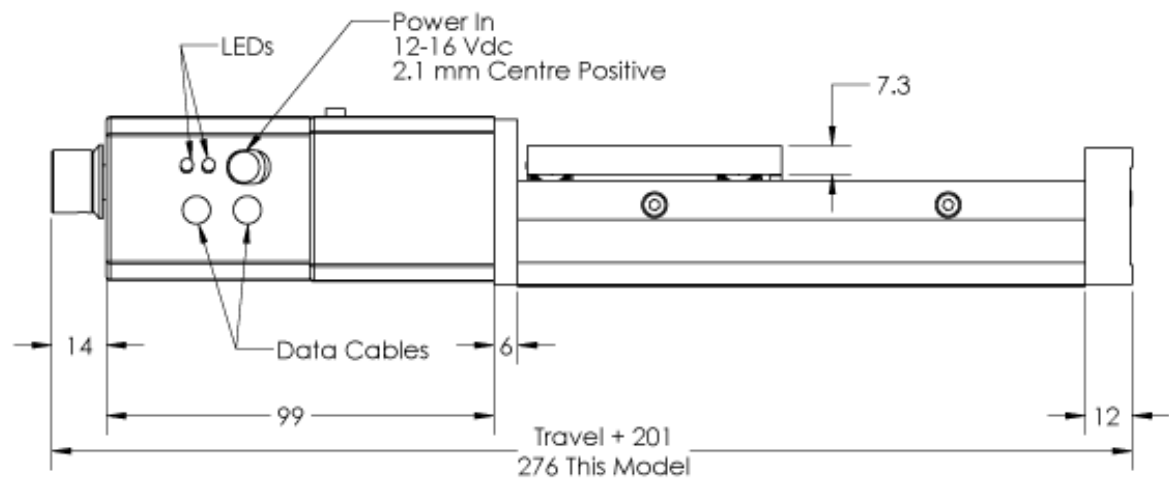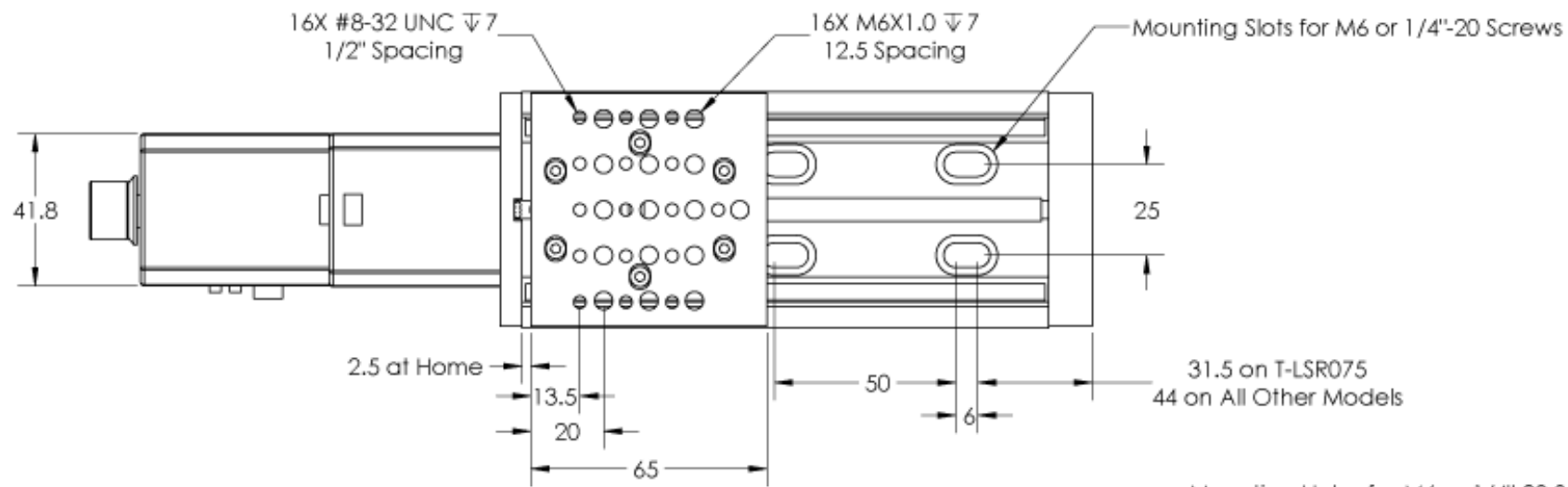
Zaber T-LSR Motorized Linear Stage
dimensions in mm

167

D-3: OptoNCDT 1302 Laser distance sensor

The miniaturised optoNCDT 1302 is a low-cost laser sensor for common measuring tasks. The extremely small design facilitates its integration even in areas with limited space. Despite the small dimensions, the 1302 series provides precise measurement results and is suitable for machine integration and automation technology.
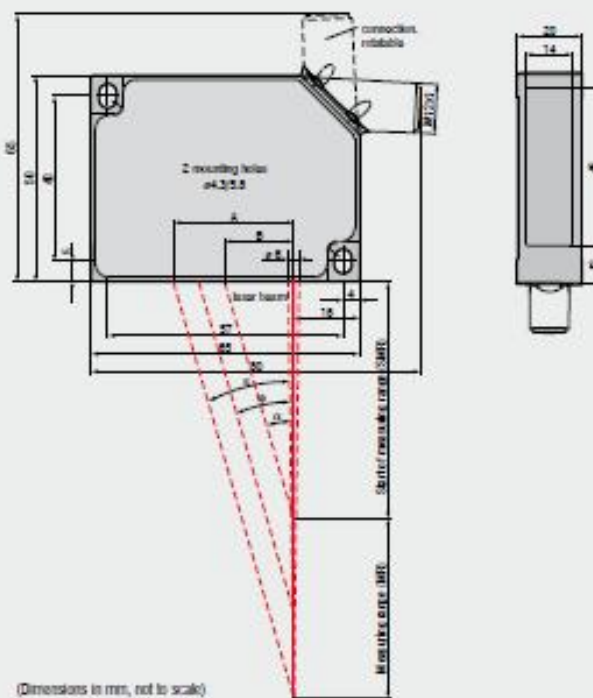
(Dimensions in mm, not to scale)

Model		ILD 1302-20	ILD 1302-50	ILD 1302-100	ILD 1302-200
Measuring range		20mm	50mm	100mm	200mm
Start of measuring range	SMR	30mm	45mm	50mm	60mm
Midrange	MR	40mm	70mm	100mm	160mm
End of measuring range	EMR	50mm	95mm	150mm	260mm
Linearity		40µm	100µm	200µm	400µm
		±0.2 % FSO			
Resolution	averaged with averaging factor 64	4µm	10µm	20µm	40µm
		0.02 % FSO			
	dynamic 750Hz	10µm	25µm	50µm	100µm
		0.05 % FSO			
Measuring rate		750Hz			
Light source		semiconductor laser <1mW, 670nm (red)			
Laser safety class		class 2 IEC 60825-1 : 2008-05			
Spot diameter	SMR	210µm	1100µm	1400µm	2300µm
	MR	530µm	110µm	130µm	2200µm
	EMR	830µm	1100µm	1400µm	2100µm
Protection class		IP 67			
Vibration		15g / 10Hz…1kHz			
Shock		15g / 6ms (IEC 68-2-29)			
Weight (without cable)		approx. 83g			
Temperature stability		0.03 % FSO/°C		0.08 % FSO/°C	
Operating temperature		0…+50°C			
Storage temperature		-20…+70°C			
Output	analogue	4…20mA (1…5V with cable PC 1402-3/U)			
	digital	RS422			
Control I/O		1x open collector output (switching output, switch. error); 1x input (teach in. trigger); 1x laser on/off			
Power supply		11…30VDC, 24VDC / 50mA			
Controller		integrated signal processor			
Electromagnetic compatibility (EMC)		EN 61326-1:2006 / EN 55011 Class B (interface emission) EN 61326-1:2006 / EN 61000-4-2:1995 + A1:1998 + A2:2001 (interference resistance)			

FSO = Full scale output. All specifications apply for a diffusely reflecting matt white ceramic target
SMR = Start of measuring range; MR = Midrange; EMR = End of measuring range

Connector axial

45.4
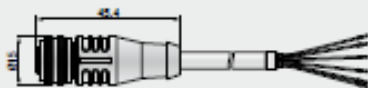
12-pin-connector
(view on solder termination side of male inserts)

Pin	Description		colour PC1402-x/I
3	RS422 Rx+	serial input	green
4	RS422 Rx-	serial input	yellow
5	RS422 Tx+	serial output	grey
6	RS422 Tx-	serial output	pink
7	+U$_B$	11-30VDC typ. 24V	red
8	Laser off	switch input	black
9	Teach in	switch input	violet
10	Error	switch output	brown
11	I$_{out}$	4…20mA	white
12	GND	supply and signal ground	blue
1/2	n.c.		

The cable screen is connected with the sensor housing. The interface and power supply cable are robot rated and UL certified. At one end there is a 12pin M12 connector, the other end is open.

169

D-4: FNS Runner block

Ball Runner Blocks made of aluminum

FNS – Flanged, normal, standard height

R1631 ... 2.

Dynamic characteristics
Travel speed: $v_{max} = 5$ m/s
Acceleration: $a_{max} = 500$ m/s²
(If $F_{comb} > 2.8 \cdot F_{pr}$: $a_{max} = 50$ m/s²)

Note on lubrication
– Pre-lubricated

Note
Can be used on all Ball Guide Rails
SNS.
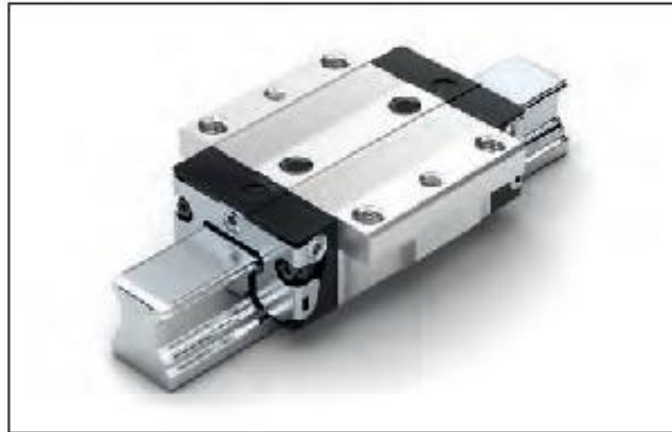
Ordering example
Options:
– Ball Runner Block FNS
– Size 30
– Preload class C1
– Accuracy class H
– With standard seal,
  without ball chain
Part number: R1631 713 20

Options and part numbers

Size	Ball runner block with size	Preload class		Accuracy class		Seal for ball runner block			
						without ball chain		with ball chain	
		C0	C1	N	H	SS	LS	SS	LS
15	R1631 1	9	1	4	3	20	21	22	23
20	R1631 8	9	1	4	3	20	21	22	23
25	R1631 2	9	1	4	3	20	21	22	23
30	R1631 7	9	1	4	3	20	21	22	23
35	R1631 3	9	1	4	3	20	21	22	23
e.g.	R1631 7		1		3	20			

Size	Load capacities[1] (N)	Permissible load (N)	Load moments[1] (Nm)			
	C	F_{max}	M_l	$M_{t\,max}$	M_L	$M_{L\,max}$
15	7 800	3 000	74	29	40	16
20	18 800	7 200	240	92	130	50
25	22 800	8 800	320	125	180	70
30	31 700	12 200	540	210	290	110
35	41 900	16 200	890	345	440	170

1) Load capacities and moments for Ball Runner Block **without** ball chain.
   Load capacities and moments for Ball Runner Block **with** ball chain ☞ B.
   Determination of the dynamic load capacities and moments is based on a travel life of
   100,000 m per ISO 14728-1. Often only 50,000 m are actually stipulated. For comparison:
   Multiply values C, M_t and M_L from the table by 1.26.

Preload classes
C0 = without preload
C1 = preload 2% C

Seals
SS = standard seal
LS = low-friction seal

Key to table
Gray numbers
= version/combination not preferred
(longer delivery times in some cases)

170

Ball Runner Blocks FNS

a) For O-ring
   Size 15: Ø 4 - 1.0 (mm)
   Size 20 - 35: Ø 5 - 1.0 (mm)
   Open lube bore as required (☞ 258).
b) Pin holes are already predrilled as illustrated (dimensions E₄, ☞ 235).
c) Lube nipple, size 15 - 20:
   Funnel-type lube nipple DIN 3405-A M3x5, B₃ = 1.6 mm
   If another lube nipple is used: observe the screw-in depth of 5 mm!
   Lube nipple, size 25 - 35:
   Hydraulic-type lube nipple DIN 71412-B M6x8, B₃ = 9.5 mm
   If another lube nipple is used: observe the screw-in depth of 8 mm!
   Lube nipples are provided (unmounted).
   Connection possible at all sides.
d) For manufacturing reasons, there may be plugs at these positions.
   These must be removed before mounting.

Size	Dimensions (mm)																	
	A	A₁	A₂	A₃	B	B₁	E₁	E₂	E₃	E₄	E₅	H	H₁	H₂[1]	H₂[2]	K₁	K₂	K₃	K₄
15	47	23.5	15	16.0	58.2	39.2	38	30	26	24.55	6.70	24	19.90	16.30	16.20	8.00	9.6	3.20	3.20
20	63	31.5	20	21.5	75.0	49.6	53	40	35	32.50	7.30	30	25.35	20.75	20.55	11.80	11.8	3.35	3.35
25	70	35.0	23	23.5	86.2	57.8	57	45	40	38.30	11.50	36	29.90	24.45	24.25	12.45	13.6	5.50	5.50
30	90	45.0	28	31.0	97.7	67.4	72	52	44	48.40	14.60	42	35.35	28.55	28.35	14.00	15.7	6.05	6.05
35	100	50.0	34	33.0	110.5	77.0	82	62	52	58.00	17.35	48	40.40	32.15	31.85	14.50	16.0	6.90	6.90

Size	Dimensions (mm)											Weight
	N₁	N₂	N₄	N₆ ±0.5	S₁	S₂	S₅	S₉	S₁₁	T	V₁	(kg)
15	5.2	4.40	10.3	10.3	4.3	M5	4.4	M2.5x3.5	3.7	60	5.0	0.10
20	7.7	5.20	13.5	13.2	5.3	M6	6.0	M3x5	4.7	60	6.0	0.24
25	9.3	7.00	17.8	15.2	6.7	M8	7.0	M3x5	5.7	60	7.5	0.30
30	11.0	7.90	20.5	17.0	8.5	M10	9.0	M3x5	7.7	80	7.0	0.55
35	12.0	10.15	24.0	20.5	8.5	M10	9.0	M3x5	7.7	80	8.0	0.75

1) Dimension H₂ with cover strip
2) Dimension H₂ without cover strip

171

D-5: SNS Ball guide rail

Standard Ball Guide Rails made of steel

# SNS with Steel Mounting Hole Plugs

R1606 .5. ..

**For mounting from above,
for steel mounting hole plugs**

Note on installation
- Steel mounting hole plugs not
  included in scope of supply.
- Follow the mounting instructions!
- Send for the publication "Mounting
  Instructions for Ball Rail Systems."
- Composite guide rails also available.

**Further Ball Guide Rails SNS and
accessories**
- Steel mounting hole plugs ☞ 179
- Mounting tool for
  steel mounting hole plugs ☞ 179
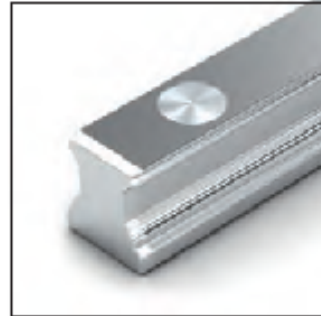
Options and part numbers

Size	Ball guide rail with size	Accuracy class					Number of sections, Rail length L (mm), ...		Hole spacing T (mm)	Recommended rail length according to formula $L = n_g \cdot T - 4$ mm
		N	H	P	SP	UP	One-piece	Composite		Maximum number of holes n_g
25	R1606 25	4	3	2	1	9	31, ...	3, ...	60	64
30	R1606 75	4	3	2	1	9	31, ...	3, ...	80	48
35	R1606 35	4	3	2	1	9	31, ...	3, ...	80	48
45	R1606 45	4	3	2	1	9	31, ...	3, ...	105	36
55	R1606 55	4	3	2	1	9	31, ...	3, ...	120	32
65	R1606 65	4	3	2	1	9	31, ...	3, ...	150	25
e.g.	R1606 75	3					31, 1676			

Ordering example 1:
(up to L_{max})
Options:
- Ball Guide Rail SNS
- Size 30
- Accuracy class H
- One-piece
- Rail length L = 1676 mm
Part number:
R1606 753 31, 1676 mm

Ordering example 2:
(over L_{max})
Options:
- Ball Guide Rail SNS
- Size 30
- Accuracy class H
- 2 sections
- Rail length L = 5116 mm
Part number:
R1606 753 32, 5116 mm

172

D-6: SRJ Spherical joints

CENTER OF BALL

17

3.6

$\emptyset$ 4.3

$\emptyset$ 11 g6 $^{-0.006}_{-0.017}$

$\emptyset$ 34 (PCD)

$\emptyset$ 16

M10

$\emptyset$ 9

$(\emptyset 14)$

$\emptyset$ 42 $^{0}_{-0.02}$

(2)

15

20

11

(31)

8

14

A-A

	NAME	DATE	DO NOT SCALE DRAWING	DIMENSIONS ARE METRIC
DRAWN	M.Dank	July 25, 2012	TITLE:	
CHECKED				
ENG APPR.			SPHERICAL ROLLING JOINT SRJ SERIES	

Unless otherwise specified, tolerance to be:CNS 4018 IT 14 Linear measures
0.5~3 ±0.1
3~6 ±0.1
6~30 ±0.2
30~120 ±0.3
120~315 ±0.5

PROPRIETARY AND CONFIDENTIAL
THE INFORMATION CONTAINED IN THIS DRAWING IS THE SOLE PROPERTY OF MYOSTAT MOTION CONTROL INC. ANY REPRODUCTION IN PART OR AS A WHOLE WITHOUT WRITTEN PERMISSION IS PROHIBITED.

Myostat Motion Control Inc.
www.myostat.ca
+1 905-836-4441

SIZE	PRT. NO.		REV
B	SRJ012C		1.0
SCALE: 2:1	WEIGHT: -		SHEET 1 OF 1

173